Università degli Studi di Torino
Scuola di Dottorato in Scienza ed Alta Tecnologia

Development of a Novel Compact Neutron Collimator for Neutron Imaging Applications within the ANET Project

Oriol Sans Planell

Università degli Studi di Torino
Scuola di Dottorato in Scienza ed Alta Tecnologia

Dottorato in Fisica e Astrofisica

Development of a Novel Compact Neutron Collimator for Neutron Imaging Applications within the ANET Project

Oriol Sans Planell

Tutor: Prof. Marco Costa
Co-Tutor: Dr. Francesco Grazzi

"The frog at the bottom of the well."

UNIVERSITÀ DEGLI STUDI DI TORINO

Abstract

Scienze della Natura
Department of Physics and Astrophysics

Doctor of Philosophy

Development of a Novel Compact Neutron Collimator for Neutron Imaging Applications within the ANET Project

by Oriol SANS PLANELL

This thesis presents the development of a new concept of compact neutron collimator, developed within the framework of the ANET project. The novel multi-channel geometry is proven to deliver highly collimated neutron beams within very limited distances, outperforming other types of neutron collimators. The technology is designed, prototyped and tested in two different facilities, a reactor source and an accelerator-based source. The optimisation work on the ANET collimator has been successful enough to demonstrate its applicability in tomography. The transport code associated to this new technology is part of the original work developed in this thesis. Through extensive resolution campaigns, this work faces also with the problem of the combination of two collimating systems in a single beamline, showing an improvement in the divergence beyond the expectations. A new theoretical approach to this problem is described and discussed.

Acknowledgements

The first acknowledgement is due for my two supervisors, Marco and Francesco. They both have done an excellent work at guiding, counselling and paving the way for me to successfully complete this work. I've learned much from both of them and I could not have wished for better tutors.
A work like this is not a single-person job. It would not have been possible without the support from the rest of the research group, from Valeria, Luca, Ettore, Betta and Francesco. All of them have put their honest contribution so this project could come to term. Same goes for those who walked the same path alongside me: Andrea, Federico and Marta.
The road up to this point has been long and tricky, there have been figures always present, pushing up and encouraging along the way. Those are my parents, who have unconditionally given me strength to keep going on.
A PhD by itself is not an easy feat, and adding a pandemic on top of it doesn't make it any simpler. Having Gaia by my side since day one has surely improved the quality of my research, as well as my personal growth.
Remembering where we come from makes it easier confront the next steps. That's why I'd like to acknowledge the work done by Carles, whose council I still go back for whenever I have a chance.
Of course, despite the fancy research performed in Turin, the measurements had to be done somewhere else. Rome handled the construction of the collimator, at the hands of Roberto. ISIS saw the first steps of the small prototype, with Antonella. Pavia hosted a myriad of tests, with the optimism and dedication of Michele, Barbara, Daniele and Saverio. The PSI is the place where the work was perfected, hosted by Anders, Uwe, Pierre and the always patient Manuel.
A particularly big thanks goes to Masako, without whom this thesis would be way shorter. Her interest and curiosity led to the final campaign of this work.
Living abroad is always complicated, but I found a net of people who made it feel like home. The cultural beer group kept the nights interesting and intellectually stimulating, with Diego, Barbara, Riccardo, Massi and Giusi.
Coming back home I've always counted on those same friends whom I've known since childhood. To those who are always there to listen when there's a problem and laugh and make fun of everything in the world. To Pau, Olga, Marti, Laia, Arnau, Ester, Axel, Mercè and Rosalba.
The world is a small place, and proof of that is the fact that some of my dearest friends are scattered across the seven seas. Anna, Deanna, Marina, Berta, Cris, Elena, Lorenzo... Having met them way before this adventure started, I could not imagine a future without them at the distance of a call.
Most probably I forgot a long list of people who have encouraged, patiently listened and even given pointers this last 3 years. To those, I offer a sincere apology, as well as a thank you. Despite not being listed here, without all those who gave some, not matter how small, portion of time for me, this thesis wouldn't be the same.
I'd like to close this acknowledgement with a preemptive thanks to anyone with the patience to read through this thesis. I hope you enjoy it!

Contents

Abstract **v**

Acknowledgements **vii**

List of Figures **xi**

List of Abbreviations **xvii**

1 Imaging technique and methodology **1**
1.1 The radiography set-up 2
1.2 Imaging figures of merit 7
1.3 The imaging system 9
1.4 The radiography technique 10
1.5 The tomography technique 11

2 Theoretical methods to evaluate the image resolution **15**
2.1 The Discrete Fourier Transform 16
2.2 The Fourier Ring Correlation 20
2.3 The Modulation Transfer Function 26

3 Design of the ANET compact neutron collimator **31**
3.1 Current state-of-the-art 32
3.2 The ANET Compact Neutron Collimator 33
3.3 The absorbing material performance study 36
3.4 The Compact Neutron Collimator method of operation 36

4 The ANET CNC proof of concept **39**
4.1 The experimental set-up 39
4.2 Results of the measuring campaign 43

5 Simulation work **47**
5.1 The Neutron Divergence Model (NeDiMo) 47
5.2 The McStas simulation tool 55

6 Performance Measurement of the ANET CNC **61**
6.1 The L/D factor extraction 61
6.2 The set-up description 62
6.3 The gadolinium knife edge technique 63
6.4 The Siemens Star method 68
6.5 Results 70

7 The Acceptance Curve parametrisation and the beam divergence calculation **73**
7.1 Mathematical description 73
7.2 Testing the Acceptance Curve parametrisation 75
7.3 Physical implications 77
7.4 Calculating the divergence angle from the simulation 77
7.5 Comparing the ANET CNC to a pin-hole collimator 79

8 Application to tomography **85**
8.1 The experiment description 85
8.2 Tomography reconstruction 86
8.3 Results 88

9 Conclusions **91**

A The Artificial Bee Colony **93**
A.1 Origin 93
A.2 The original algorithm 94
A.3 State of the art improvements 95
A.4 Benchmarking 96

Bibliography **99**

List of Figures

1.1 Table showing the mass attenuation coefficient with respect to the atomic number of most elements. Comparison between different energies of X-Rays and neutrons [1] 2
1.2 Greyscale attenuation maps the interaction behaviour of different neutron energies and X-Rays with $1cm$ thickness of given materials. The darker the color, the stronger the interaction, as would the result be for a radiography. For X-rays, the heavier the element or compound, the bigger the attenuation. For fast neutrons, the value decreases with the atomic number, while for thermal neutrons the attenuation varies greatly depending on the isotope [1] 2
1.3 Comparison between a light photography, X-ray radiography and neutron radiography of the motor of a toy airplane. 3
1.4 **Left**: Design of a conical beam. **Right**: Design of a parallel beam. 4
1.5 Graphical description of the intensity reduction of a wave travelling through a potential. As the figure suggests, the intensity of the beam decreases exponentially with the depth of the material. 5
1.6 Representation of the standard neutron imaging setup using a CCD camera. The neutrons are absorbed on the scintillator screen which, through fluorescence, emits light which is deviated by a mirror and collected on a detection system. The goal of the mirror is to protect the detector from the direct beam. . 7
1.7 Design of the imaging setup with the variables employed. . . 8
1.8 Analogy to the inner workings of a CCD camera. The water buckets get all filled, and then the right-most line discharges first onto a separated bucket array, which in its turn get emptied, one by one, on a calibrated sensor. This process allows for the identification of the charge -water quantity- on each pixel -water bucket- sequentially. 10
1.9 Inner workings of a CMOS sensor. Further details are explained in the text. 11
1.10 Example of the histogram of a grayscale image. 11
1.11 **Left**: Low brightness (blue) and high brightness (red). The dynamic range is compressed between the two limits, highlighting a narrow range of grayscale intensities. **Right**: Narrow contrast (red) and wide contrast (blue). A wider contrast smooths the dynamic range of the image over a larger set of values, delivering an more blurry image as a result. 12
1.12 P stands for the radiographic projection, while S_n is the n^{th} tomographic slice. 13

1.13 Step-by-step creation of a sinogram 13
1.14 Representation of the Filtered Back-Projection algorithm. . . . 14

2.1 Design of the imaging setup with the variables employed. . . 15
2.2 Crop from a black-and-white image taken at the gulf of Roses, in the northern Catalonia. 17
2.3 Magnitude of the Fourier Transform without the logarithmic operator (left) and with it (right). 18
2.4 Comparison between the original image (top-left) and the noisy version (top-right), and a plot showing the relative intensity at Y = 200 in both images (bottom). 19
2.5 Discrete Fourier Transform applied to the original example image (top-left) and the DFT applied to the noisy image (top-right). Plot showing the greyscale intensity (on a 0-255 scale) at Y = 150 for both images (bottom). 20
2.6 FRC calculated on the example image with the $T_{\frac{1}{2}bit}$ threshold curve. 25
2.7 Four cases of FRC curves measured on the same image under different noise conditions. 26
2.8 Image chosen as an example for the MTF demonstration. The clear contrast generates a good edge to calculate the MTF. . . . 28
2.9 LSF curve together with the gaussian fit. 28
2.10 MTF curve with the polynomial fit of grade 6. 29

3.1 First image of the article from K. Ogawa and N. Wakabayashi [29] showing the design of a thermal neutron collimator for research purposes. 32
3.2 Design of the cross-sectional view of the 7R beam tube for the JRR-3M research reactor built near Tokai, in the Ibaraki Prefecture, north of Tokyo. The image is extracted from [35]. 33
3.3 3D rendering of the ANET compact neutron collimator. 34
3.4 Design of the collimator structure. D is the dimension of a single channel and L the length of the collimator structure. . . 35
3.5 Total, scatter and absorption cross-section of the material used to build the collimator absorbing rods as a function of the neutron energy. 35
3.6 Distribution of the ratio T_{ideal}/T_{real} as a function of the collimator depth. The curves correspond to different choices of the beam divergence as quoted in the legend. 37
3.7 Schematic design of the resulting image combining two collimator positions on a fixed object. Images A and B emulate a neutron radiography with the CNC in two complementary positions, and C the result of combining the two former images. 37

4.1 Design of the basic set-up used in ANET experiments. 40
4.2 The image shows a radiography of the collimator before the alignment (left) and after (right). In both cases, the chessboard structure is clearly visible. After the alignment the illumination of the alternated channels is well uniform, suggesting the definition of an internal fiducial area. 41

4.3 Schematics of the triangular pattern of the dynamic approach of the collimator method of operation. 42
4.4 Comparison of radiographies done statically (left) and dynamically (right). For details see text. 42
4.5 Table showing the normalised measurements of the Siemens star with and without the collimator at $40mm$ and $20mm$ from the scintillator respectively. 43
4.6 Comparison between the resolution obtained with and without the ANET collimator under the LENA Channel B beam. . 44
4.7 Comparison between the resolution obtained with the ANET collimator and that expected from the theoretical model. . . . 45

5.1 Geometry of the 2D model also including most of its variables. 47
5.2 Coordinate system used for NeDiMo. The collimator's lower-left vertex is placed at the origin (0,0). The two coordinate systems used for transport are (x, y, z, θ, ϕ) and $(x, y, z, \alpha_{zx}, \alpha_{zy})$. Neutrons are generated uniformly with respect to $cos(\theta)$, then transported using the "cartesian" angles $(\alpha_{zx}, \alpha_{zy})$, and eventually registered on the initial coordinate system. 49
5.3 "Heat map" of the exit window of a single CNC channel showing the maximum possible L/D factor at each point in the plane. 52
5.4 Distribution of θ (right) and ϕ (left). 52
5.5 Distribution in ϕ of all the neutrons arriving at the detector after the collimator. 53
5.6 Polar plots of simulated angular distributions. The difference between the four plots is related with the position of the monitor w.r.t the square collimator channel: (a) top-left vertex, (b) centre-top, (c) centre and (d) centre-left. 54
5.7 Two examples of Siemens star simulated under the measuring conditions of the LENA facility. The distance between the Siemens star and the detector is 10 mm (left) and 30 mm (right). 55
5.8 Rendering of the McStas model of BOA, including the custom ANET CNC section and monitors. The light blue element at the lower right belongs to the ANET CNC; while the objects on the left represent the guides and bender, as well as the source of BOA. 55
5.9 McStas simulation of the BOA facility. Heat maps of the divergence at the exit window of BOA. Left: Vertical divergence map, Right: Horizontal divergence map. 57
5.10 Left: Heat map of the total divergence at the exit window of BOA. Right: 2D histogram of the axial-wise divergence at the exit window of BOA. 57
5.11 Heat map of the divergence at $5.23m$ from the exit window of BOA. Left: Vertical divergence map, Right: Horizontal divergence map. 58
5.12 Heat map of the divergence at $5.23m$ from the exit window of BOA and right after the ANET CNC. Left: Vertical divergence map, Right: Horizontal divergence map. 58

5.13 Plot highlighting the variation in angular distribution when varying the tilt angle of the collimator (left), and rocking curve (right). 59

6.1 Two radiographies taken at macro-position 1 with the ANET collimator in, at 70mm (top) and 10mm (bottom) from the detector. 64
6.2 Image chosen as an example for the MTF demonstration. Image taken at the macro-position 1, with the ANET CNC in the beamline, with the sample at 50mm from the detector. 64
6.3 The LSF curve together with the gaussian fit. 65
6.4 The MTF curve with the polynomial fit of grade 6. 65
6.5 Detector contribution to the spatial resolution measurement as a function of the MTF threshold. 66
6.6 Sample of the L/D calculation from the measurements with collimator in position 3. 66
6.7 Resolution fit on macro-position 3, in both the BOA and BOA+ANET configurations, for the horizontal and vertical axis. 67
6.8 Calculated divergence angle on every configuration using the gadolinium knife-edge method. B+A stands for "BOA + ANET", while P1-4 correspond to the macro-positions 1 to 4 as detailed in the previous section in table 6.1. The errors have been evaluated using a Monte Carlo procedure and the ABC algorithm. 67
6.9 Two examples of measurements taken with the Siemens star in macro-position 1, at 10mm and 60mm from the detector respectively. 68
6.10 Representation of the process of "unfolding" the Siemens star using Fiji (ImageJ). The reslicing operation is done clockwise from the 45° line. 69
6.11 Visualisation of the unfolded and segmented Siemens star. The greyscale image is displayed using the "jet" LUT in order to highlight the difference between the noise region and the actual spikes of the Siemens star. 69
6.12 Left: Sample of the standard deviation of a measure in position 1, at 10mm from the detector. The red dotted line separates the noise region and the signal. Using a 2σ threshold, the value for the resolution is 79μm. Right: Histogram of the noise created by the standard deviation in the noise region. The noise is fitted with a Gaussian curve in order to obtain the 2σ threshold. 70
6.13 Calculated divergence angle on every configuration using the Siemens star. The label "B+A" stands for "BOA + ANET", while P1-4 correspond to the macro-positions 1 to 4 as detailed in the previous section in table 6.1. The errors have been evaluated using a Monte Carlo procedure and the ABC algorithm. 71
6.14 Comparison between two Siemens star measurements, without and with the ANET CNC, in macro-position 2, at 20mm from the detector. 71
6.15 Graph showing the divergence angle calculated on each macro-position with both the Siemens star and the gadolinium knife-edge. 72

7.1 2D acceptance curves calculated at different values of L/D. . . 74
7.2 Different acceptance curves calculated in 3D. 75
7.3 Vertical and horizontal angular divergence distribution plots before and after the ANET CNC along with the predicted distribution. Simulation done with the CNC at 20 *cm* from the exit window of BOA. 76
7.4 Vertical and horizontal angular divergence distribution plots before and after the ANET CNC along with the predicted distribution. Simulation done with the CNC at 5.23 *m* from the exit window of BOA. 76
7.5 Results of the simulations of the 3D neutron angular distribution before and after the ANET CNC, along with the analytical calculation of the resulting angular distribution. 77
7.6 Result of the calculation of the χ^2 with all the measures from the gadolinium knife-edge and the Siemens star. 78
7.7 Graphical summary of all the measurements with the gadolinium knife-edge, the Siemens star and the calculated values. . . 79
7.8 Comparison between the 3D acceptance curves of the ANET CNC and an equivalent pin-hole system. 80
7.9 Comparison between the 2D angular distributions of the pin-hole and the ANET CNC on the detector. The neutron survival probability is plotted against the divergence angle. 80
7.10 Comparison between the 2D maximum divergence distributions of the pin-hole and the ANET CNC on the detector. The two colour map scales show the divergence angle and the equivalent geometrical resolution measured when a sample is placed at 30 *mm* from the detector (calculated using equation 1.7). . . 81
7.11 Histograms comparing the number of neutrons on each angle, calculated on two simulations with the same number of particles. 81
7.12 Histograms comparing the number of neutrons measured on a 10 x 10 cm^2 ANET CNC and a pin-hole system, with a L/D factor of 160 and a detector of 10 x 10 cm^2. 82
7.13 Simulations of the angular neutron distribution in all macro-positions with and without the ANET CNC. 83

8.1 The measurement set-up (left) with a detail on the rotary stage (right). (1) The ANET CNC, (2) The Stewart platform, (3) The T5 stage, (4) The T6 stage, (5) The ZnS-Lif(Ag) scintillator, (6) The Andor cooled camera, (7) The rotary stage, (8) Samples for the neutron tomography inside the aluminium tube. 85
8.2 Average Z-profile on a small squared area devoid of sample, extracted from the tomography dataset. 86
8.3 Comparison between the raw image and the pre-processed result after the normalisation and de-noise. 87
8.4 False colour 3D models of the reconstructed fibula. 1- "pristine metal" volume fraction unaffected by the corrosion, 2- Transparent isosurface which represents the effective mineralised layer. 88
8.5 Rotation of the False colour 3D map representation of the iron fibula with a highlight on the largely attenuating corrosion. . . 88

8.6 Slice of the reconstructed tomography from the lapis lazuli. The pyrite can be individualised with ease, as the contrast is very different from the other two phases. The calcite and lazurite are very similar in attenuation, and thus remain harder to distinguish. 89
8.7 False colour 3D model of the lapis lazuli, with three different cuts to highlight, with the appropriate colour map, the different material distributions within the mineral. 90

A.1 Number of articles published related to the *Artificial Bee Colony* algorithm and *Swarm Intelligence* each year. 93
A.2 Comparative plot of the performance between the classical ABC algorithm and the modified version, ABC-ESDL, applied to the Rastrigin function. 96
A.3 Comparative plot of the performance between the classical ABC algorithm and the modified version, ABC-ESDL, applied to the Eggholder function. 97

List of Abbreviations

ABC	**A**rtificial **B**ee **C**olony
ANET	**A**dvanced **NE**utron **T**echniques
BOA	**B**eamline for neutron **O**ptics and other **A**pproaches
CCD	**C**harged **C**oupled **D**evice
CMOS	**C**omplementary **M**etal-**O**xide-**S**emiconductor
CNC	**C**ompact **N**eutron **C**ollimator
CT	**C**omputed **T**omography
DFT	**D**iscrete **F**ourier **T**ransform
ESDL	**E**lite **S**trategy and **D**imension **L**earning
ESF	**E**dge **S**pread **F**unction
FBP	**F**iltered **B**ack-**P**rojection
FFT	**F**ast **F**ourier **T**ransform
FOM	**F**igure **O**f **M**erit
FRC	**F**ourier **R**ing **C**orrelation
FSC	**F**ourier **S**hell **C**orrelation
HPC	**H**igh **P**erformance **C**omputing
LAN	**L**ocal **A**rea **N**etwork
LENA	**L**aboratorio **E**nergia **N**ucleare **A**pplicata
LSF	**L**ine **S**pread **F**unction
LUT	**L**ook **U**p **T**able
MTF	**M**odulation **T**ransfer **F**unction
NeDiMo	**Ne**utron **Di**vergence **Mo**del
OTF	**O**ptical **T**ransfer **F**unction
PLA	**Poly**l**actide** **A**cid
PSF	**P**oint **S**pread **F**unction
PSI	**P**aul **S**cherrer **I**nstitut
PTF	**P**hase **T**ransfer **F**unction
SNR	**S**ignal-to-**N**oise **R**atio

Introduction

The objective of this thesis is the design, construction and test of a novel compact multi-channel neutron collimator and demonstrate its application in neutron radiography. The work has been done within the framework of the ANET (Advanced NEutron Techniques) INFN project.

Chapter 1 contains the theoretical introduction. There is a brief explanation of imaging techniques, the experimental set-up composition and the definition of the figures of merit that will be used in the thesis. There is also an overview of the general data analysis method used in radiological imaging, followed by a summary on the history of neutron collimators and ending with a brief state-of-the-art on the subject.

Chapter 2 describes the methodology and techniques used to evaluate the image resolution: starting from the mathematical explanation up to two hands-on examples of the Fourier Ring Correlation and the Modulation Transfer Function techniques.

Chapter 3 explains the design of the ANET compact neutron collimator in detail, including the studies related to the material choice and expected method of operation.

Chapter 4 contains the description of the first commissioning of the ANET CNC. For this purpose the prototype was brought to the LENA facility in Pavia (Italy) and tested to determine its performances on a thermal neutron beam. In this chapter there is also an explanation on the way to operate the CNC and the alignment procedure.

Chapter 5 describes the simulation work done to characterise the collimator and its combination with the beamlines. It is divided in two wide sections: the python custom model NeDiMo (Neutron Divergence Model) and the widely used McStas.

Chapter 6 explains in detail the experimental campaign at the BOA facility at the Paul Scherrer Institut. The measurements used standard reference samples: a Siemens star and a Gadolinium knife-edge. A description of the analysis methodology and a discussion of the results are reported.

Chapter 7 describes the parametrisation of the acceptance curve and the theoretical calculation of the spatial resolution. The comparison between the ANET CNC and the traditional pin-hole collimating system is discussed.

Chapter 8 demonstrates the applicability of the ANET technology in a tomographic reconstruction using two samples with different geometries and compositions. The procedure, as well as the data elaboration and issues encountered are explained in this chapter.

Chapter 1

Imaging technique and methodology

The main field of this thesis is neutron imaging. The core concept is the capability of acquiring images not from visible photons, as common photography, or even X-rays, as the medical radiography, but with neutrons. The process to achieve a result encompasses a myriad of elements, combining different fields, such as nuclear physics or optics, dabbling in chemistry and making use of astronomical tools. To understand the work performed in this research work, this chapter will be dedicated to an overview of all the theoretical ingredients required to go from the design idea of the collimator to the final result. Once the data have been acquired, they must be properly analysed. This process varies not depending on the radiation source (it's very similar for both photons and neutrons), but depending on the setup and detector. Before entering on the specifics, it is important to have a basic understanding on how the camera obtains the image, and how the information is digitised. The two following subsections will detail how the data elaboration proceeds in case of a radiography and a tomography both taken with a CCD or CMOS camera.
As already mentioned, different radiation sources may be used to radiograph a sample. The two main options studied are X-Rays and neutrons. The two radiation approaches are somehow complementary to each other, as they bring different information from one same sample. The mass attenuation coefficient for X-rays increases with the atomic number of the elements, while the average tendency of interaction of neutrons it varies without a regular behaviour. The difference in tendency, shown in Figure 1.1, is due to the different interaction between those two types of radiation. X-Rays essentially interact with matter through photoelectric effect, Compton effect and pair production, all processes which increase with the atomic number, while neutrons interact through nuclear reactions, elastic and inelastic scattering, which depend on the internal structure of the nucleus.
Figure 1.2[1] highlights how, for the same 1 cm thick material, different neutron energies widely vary their behaviour, and how X-Rays increase linearly their interaction with the atomic number, as seen previously on Figure 1.1.
It is important to remark the fact that neutrons do not bring more information than X-Rays, but a complementary amount. This fact can be appreciated in Figure 1.3 where a toy replica of a combustion engine with a plastic propeller is studied with both X-rays and neutrons.

[1] Brought by Prof. Burkhard Schillinger, from the Technische Universität München.

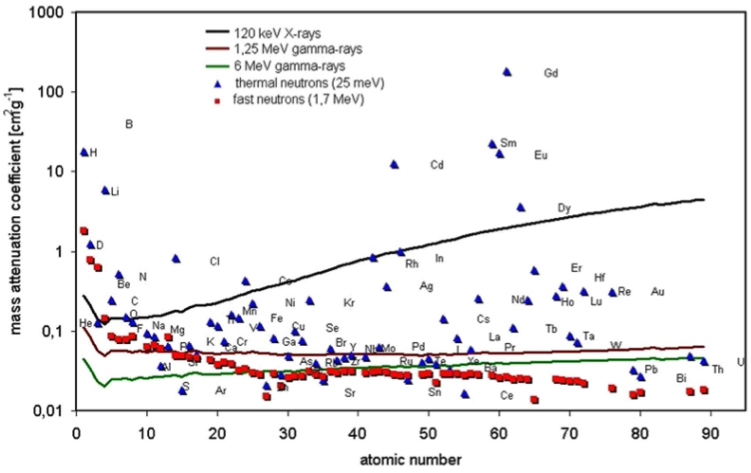

FIGURE 1.1: Table showing the mass attenuation coefficient with respect to the atomic number of most elements. Comparison between different energies of X-Rays and neutrons [1]

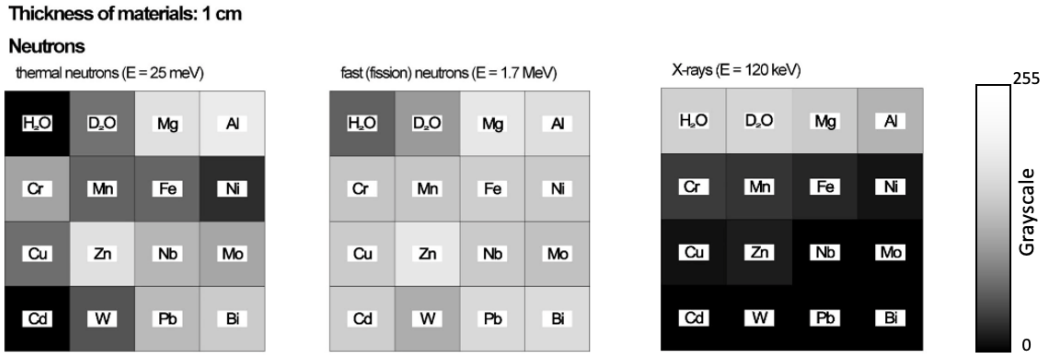

FIGURE 1.2: Greyscale attenuation maps the interaction behaviour of different neutron energies and X-Rays with $1cm$ thickness of given materials. The darker the color, the stronger the interaction, as would the result be for a radiography. For X-rays, the heavier the element or compound, the bigger the attenuation. For fast neutrons, the value decreases with the atomic number, while for thermal neutrons the attenuation varies greatly depending on the isotope [1]

The X-Rays can easily penetrate the plastic propeller and the aluminium given their light density, but are very attenuated on the steel components. With neutrons, aluminium is still very transparent, not because of its density but because of the small cross section, while steel is more easily penetrated and plastic is instead quite opaque due to the hydrogen within it that triggers the scattering of thermal neutrons.

1.1 The radiography set-up

By definition, a radiography is the construction of an image using ionising or non-ionising radiation. The most commonly used are the X-ray-based radiography techniques, which include medical radiography, airport security body scanners or industrial non-destructive testing, among many others. In

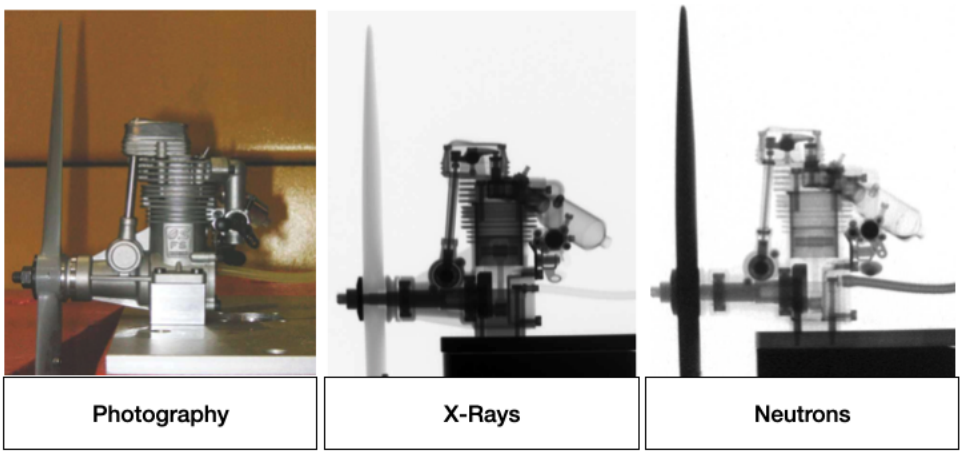

FIGURE 1.3: Comparison between a light photography, X-ray radiography and neutron radiography of the motor of a toy airplane.

our case, the research is focused on the usage of neutrons as the image inducer particle. With any kind of radiography, the output image represents the shadow created when the various materials that compose the object absorb differently the passing radiation on a projected screen. Since at the moment it doesn't exist any optical system or computer method capable of properly eliminating the aberrations created by the optical system, the radiation beam must be appropriately collimated. Through radiography, it is possible to extract morphological, structural and composition information on a sample. Under optimal conditions, a radiography setup is composed by:

1. Source: Typically a point source placed far from the object for a parallel beam, or close when targeting a conical beam for magnification.
2. Collimator: Usually a cone or cylinder that ensures that the radiation passing through is parallel or uniformly divergent to the source-object axis to a high degree.
3. Sample: The object to be measured or studied illuminated by the incoming beam. To optimise the image quality the sample shall be as thin as possible.
4. Detector: Placed close to the sample for the parallel beam, or far when using a conical beam, with a high spatial resolution.

Depending on the individual characteristics of these elements, there might appear alternative geometries or usages.

1.1.1 The beam shape

The radiation beam may take different shapes. Here are two examples:

1. Conical beam: To conform such a shape, it is required a point source and a big detector, as the image will be enlarged due to the optical geometry, as seen in Figure 1.4 on the left.

2. Parallel beam: As depicted on the right side of Figure 1.4, a parallel beam shape is composed by a very large (less collimated) - or very distant (weak intensity) - source, which will generate an image with similar dimensions to those of the object being studied. This kind of setup is both compatible with neutrons and X-rays. In order to reduce the inner divergence of the system, it is imperative for the object to be as close as possible to the detector.

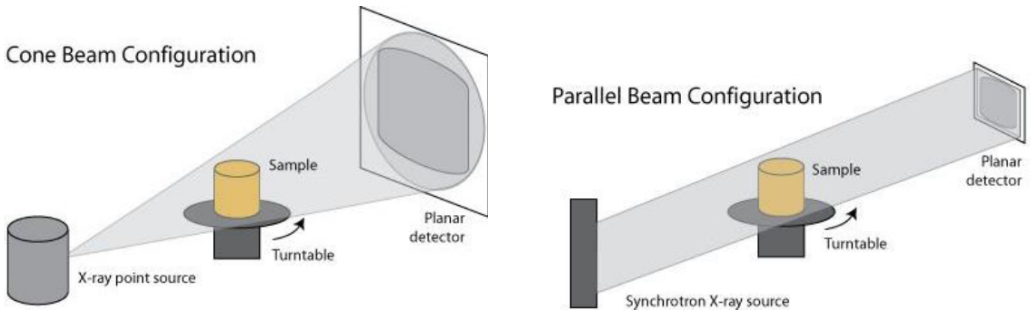

FIGURE 1.4: **Left**: Design of a conical beam. **Right**: Design of a parallel beam.

1.1.2 The collimator

Most definitely one of the core concepts of this doctoral thesis. The collimator theory and its applications hold a main role on the development of this work. From the Oxford Dictionary [2] "collimation" is defined as "make (rays of light or particles) accurately parallel".
The collimators for X-rays are fairly simple, as they are composed by heavy-Z materials which essentially leave only a limited aperture, constraining the beam to pass through it and adapt to the geometry. Neutrons, on the other hand, are trickier than X-rays, and thus this subsection will be focused on them. To create a neutron imaging infrastructure, one of the key components is a mono-directional neutron beam with as little angular dispersion as possible. Since neutrons don't have an electrical charge, there are a few ways to ensure the proper direction of a beam. In this section some of them will be described, along with the physical quantities related to the collimation of a beam. The vast majority of the neutron collimation systems follow the same principle of operation, with long thin tubes, in most cases under vacuum, surrounded by absorbing and attenuating materials. Those neutrons capable of surviving the path are those with the smallest divergence angle. A cheaper alternative is that of leaving a small aperture and placing the detector at a great distance. This forces the neutrons arriving at the detector to have a very small angle of divergence. This is called a pin-hole collimator. In order to reduce the length of the overall set-up, some alternative designs to the long tubes or the pin-holes have been developed. One approach is that of limiting one of the dimensions of beam propagation, placing many parallel sheets of absorbing material, limiting the neutron divergence on the perpendicular direction of the plaques, while leaving it free on the other. This approach is called the Soller collimator. In order to limit simultaneously both axis and at the same time constrain the length of the setup, two examples of

alternatives that have been developed so far are the honeycomb collimators, which have a hexagonal structure, similar to those present in nature, and have formerly been used in X-ray applications, made of heavy materials. For neutrons, the examples found in literature are covered in highly absorbent material. The second approach is that of the micropore collimator, in which a block of material is laser carved with microscopic tunnels to create a myriad of small cylindrical channels for neutrons to pass through, while the rest are absorbed.

1.1.3 The sample

The sample will alter the beam itself, not only by absorbing the radiation but also creating distortions. The absorption on the material - for both neutrons or photons - will follow the law of Lambert Beer. The equation can be derived from the following assumption: Considering the transmission defined as:

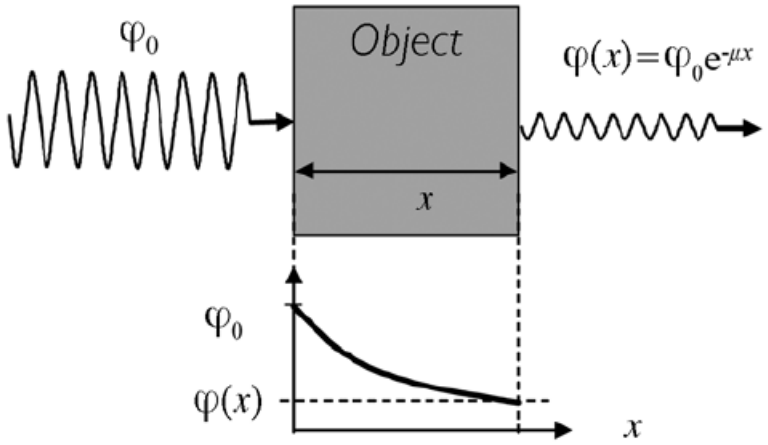

FIGURE 1.5: Graphical description of the intensity reduction of a wave travelling through a potential. As the figure suggests, the intensity of the beam decreases exponentially with the depth of the material.

$$T = \frac{I}{I_0} = e^{-\Sigma x} \tag{1.1}$$

Being Σ the material's macroscopic cross section, which is equivalent to the materials microscopic cross section (σ) multiplied by the atom density by volume unit (n), x is the depth, and I_0 and I the initial and final beam intensity, respectively. Given a certain width Δx, we can define the intensity variation due to the beam going through the material as:

$$\Delta I = -In\sigma\Delta x \tag{1.2}$$

Or as it would be in its continuous form:

$$dI = -Indx \tag{1.3}$$

Solving the differential equation leads to the Lambert Beer law:

$$I = I_0 e^{-n\sigma x} \tag{1.4}$$

Overall, the defining factor that alters the intensity is defined by the density of the material, the amount of material that the beam shall go through, and the material itself. The interaction probability will vary depending on the type of radiation and material itself, as follows:

1. For electrons: $\sigma(e)_{tot} = \sigma(e)_{sct}$
2. For photons: $\sigma(\gamma)_{tot} = \sigma(\gamma)_{abs}$
3. For neutrons: $\sigma(n)_{tot} = \sigma(n)_{sct} + \sigma(n)_{abs}$

A gross approximation can be considered, depending on the particle composing the beam. In case of the beam being electron-based, the major effect will be from scattering. Contrary to that, the biggest effect in case of the beam being made of photons would be the absorption, while with neutrons both scattering and absorption have a big role, depending on the material. A movement system, composed by a rotary stage is usually found on the sample, allowing different angle studies, fine position tuning and tomography.

1.1.4 The detector

Following the design in Figure 1.6, the neutrons are initially absorbed on the scintillating layer, following a nuclear capture reaction. The energy release by the process emits light through the scintillating material. The light emitted bounces at the 45º angled mirror up to the camera, which integrates the readings over a period of time, generating the image.
The scintillation in the screen is a two-step process: first a reaction with very high absorption cross section isotopes (^{155}Gd,^{157}Gd,^{6}Li or ^{10}B) which create secondary radiation that forces an excitation of a luminous material that shows a fluorescence emission in the optimal range for the detection system. It can either be built in two phases (first absorbent and then the fluorescent) or as a single component, in which the material both absorbs the neutrons and emits light in response. There is always an equilibrium to be found when building the scintillating screens, as the thickness determines both the light output and resolution. A thick screen will increase the light output, while a thin one will operate in the opposite way, with less light output the measuring time will increase.
The combination of ZnS/^{6}LiF is one of the most widely used, as it yields one of the highest light outputs on the market. When the scintillator is Cu doped, it has a light peak emission at a wavelength of 530 nm, which corresponds to a green light photon. In order for the detection to be optimal, the camera must be properly chosen to have a maximum sensitivity to the wavelength emitted by the scintillator (or vice-versa, the scintillator shall be chosen in accordance to the camera). The most common cameras used are either CMOS or CCD. The election of either one or the other greatly depends on the experiment[2].

[2] An extensive overview on the specific operational differences between CMOS and CCD cameras is found in section 1.3

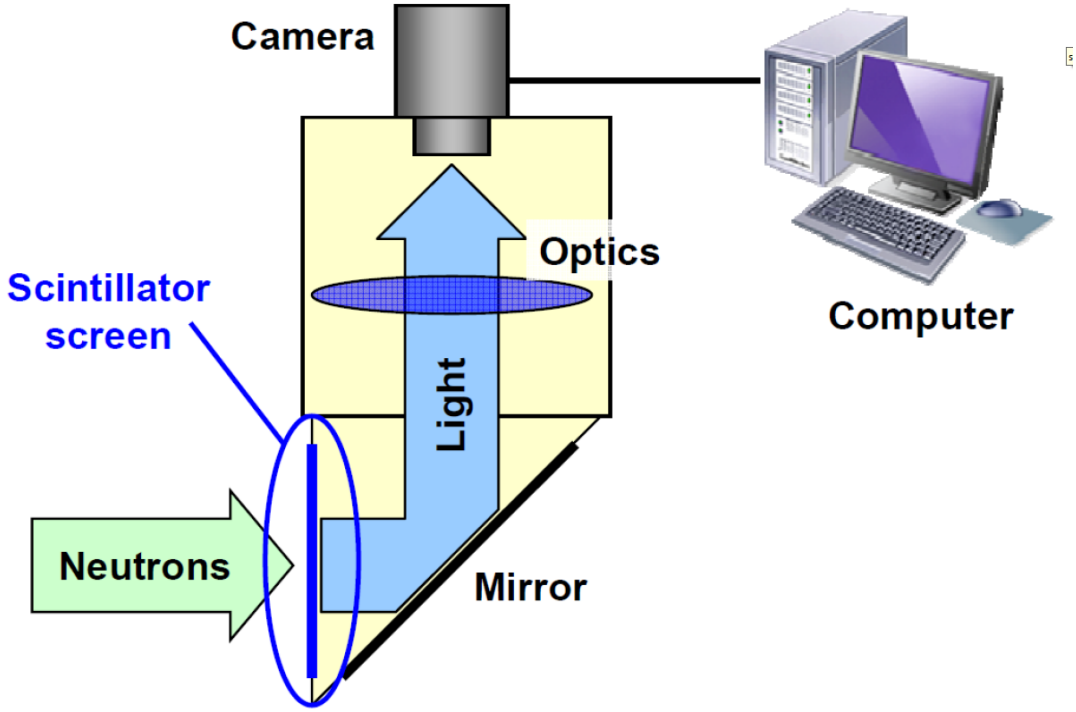

FIGURE 1.6: Representation of the standard neutron imaging setup using a CCD camera. The neutrons are absorbed on the scintillator screen which, through fluorescence, emits light which is deviated by a mirror and collected on a detection system. The goal of the mirror is to protect the detector from the direct beam.

To obtain the resolution of an image, one of the most widely used techniques, not only in radiography, but in photography in general (applied in both physical images and digital ones) is the Siemens Star. The Siemens Star, also known as spoke target, is essentially a pattern of bright spikes all pointed towards a single point at the centre. When the Siemens Star is photographed on a limited resolution device, the spikes will contact at a certain distance of the centre. This phenomenon permits the measurement of the resolution of the imaging instrument. In the recent years, the PSI has developed a Siemens Star for neutron imaging [3] built in gadolinium, with a layer thickness of 0.5μm. This object will be further studied later on in this thesis.

1.2 Imaging figures of merit

The simplest model to describe the effect of the collimation of a radioimaging set-up with a collimator is that of figure 1.7. There are a few figures of merit (FOM) which need to be defined for its relevance in imaging. The most relevant one -for this thesis- is the concept of *collimation power*, or L/D factor. As the name defines, it is the relationship between the diameter of the beam aperture and the distance between the aperture and the sample:

$$\frac{L}{D} = \frac{length}{diameter} \tag{1.5}$$

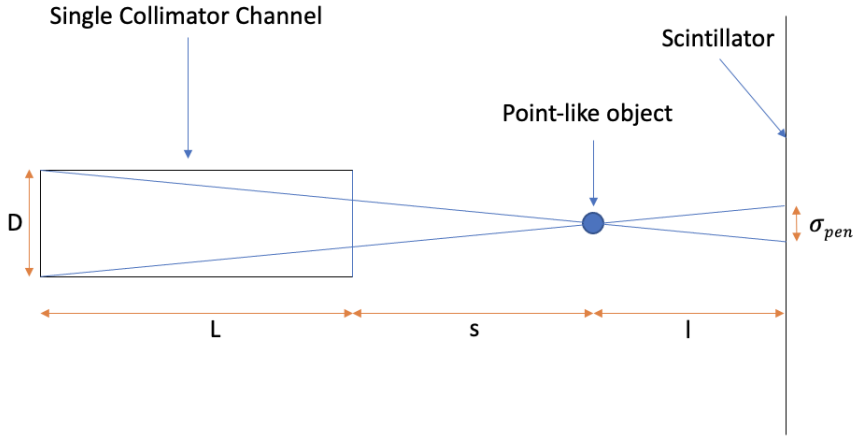

FIGURE 1.7: Design of the imaging setup with the variables employed.

The definition, as stated, is applied to a pinhole collimator. In case of a long-tube, the L/D of the collimator is the length of the tube divided by its diameter. In the particular case of multi-channel collimators, the L/D is defined for each individual channel, treating the device as an array of long-tube collimators. The L/D is directly related with the divergence of the beam through the trigonometric formula:

$$\sigma_{div} = arctan\left(\frac{1}{L/D}\right) \tag{1.6}$$

Namely, the arctangent of the inverse of the L/D is equivalent to the angle of acceptance of the neutrons passing through the collimator -i.e not absorbed-. Since the collimation power is present on the mathematical definition of the blurring, the higher the L/D, the smaller the penumbra and the better the resulting image quality will be. The *optical penumbra*, also called *blurring*, which is defined as the shadow created by a light source when impacting an opaque object. When using an imaging technique with radiation, the penumbra becomes a distortion or spread of every point of the object when projected on the detector screen. The penumbra can be easily calculated through:

$$\sigma_{pen} = \frac{lD}{L+s} \tag{1.7}$$

In equation 1.7 the collimation power is present with a slight variation: the L/D is transformed into a (L+s)/D, in which the true divergence is improved due to the distance -s- and it is smaller than the geometrical L/D of the collimator. When the distance between the collimator and the sample is very small, though, the geometrical calculation for the collimator is a good approximation of the true L/D.
All those parameters described so far behave independently from one spatial dimension to another. A beam can be extremely well collimated in the vertical axis and more divergent on the horizontal one. The image taken under

such conditions would have an elevated image resolution along the horizontal axis and very low one on the vertical[3].
Another important parameter which has an effect on the image quality is the detector resolution, labeled as σ_{det}. Since the camera has a discrete structure to collect light (pixels), there is a limit on how much resolution it can have. A good approximation to σ_{det} is twice the size of a pixel projected to the scintillator screen. This approximation is also called *Nyquist number*. The final resolution of the image can be calculated by combining the penumbra blurring and the contribution of the detector via the following equation:

$$\sigma_{total} = \sqrt{\sigma_{pen}^2 + \sigma_{det}^2} \tag{1.8}$$

This equation implies that, by measuring the spatial resolution of an image and knowing the limit resolution of the detector, it is possible to calculate the penumbra of the image, and extract from there the divergence of the incident beam.

1.3 The imaging system

The two most commonly used systems, CCD (Charge-Coupled Device)[4] and CMOS (Complementary Metal Oxide Semiconductor)[5]. Each cell of a CCD image is an analog device. When light gets to the photo sensor it produces a small electrical charge. The charges in the line of pixels placed nearest to the output amplifiers pass through them, and then each line of pixels shifts its charges one line closer to the amplifiers, as represented in Figure 1.8. This process is iterative until all the lines of pixels have read their charge.
Contrary to the CCD, the CMOS image sensor has an amplifier for each individual pixel. The result of that is less effective area for the capture of light - compared to the CCD -, although this difference can be compensated with the use of microlenses in front of the photodiodes. A depiction of the CMOS architecture appears in Figure 1.9.
Both systems can accumulate signal up to a certain maximum value which is measured in an exponential scale of base 2. For example, having an endpoint $2^N - 1$ implies that the device has N bits. This value N typically takes values 8, 12, 14 or 16. The data acquired can be either 2D or 3D. 2D images are typically pictures, radiographs or CT slices, while 3D images would be volumes (x,y,z) or movies (x,y,t). The building blocks of an image are either a square (2D), called pixel, or a cube (3D), named voxel, which are defined by intensity, colour and coordinates. To conform the image, every element will be associated with a value as a function of the intensity of the signal under which it has been irradiated. As seen in Figure 1.10 a statistical analysis on the frequency of the number of pixels as a function of the individual's intensity leads to a histogram which can be used as a guide to visualise certain properties of the image. It is the basis for the segmentation method. The segmentation method in image processing or computer vision is the process of

[3]Very small penumbra on an axis is shown on the perpendicular one. For example: A vertical straight line will highlight the horizontal spatial resolution, but not the vertical.
[4]Invented by Williad S. Boyle and George E. Smith in 1969.
[5]Merit of Nobukazu Teranishi, Hiromitzu Shiraki and Yasuo Ishihara in 1980.

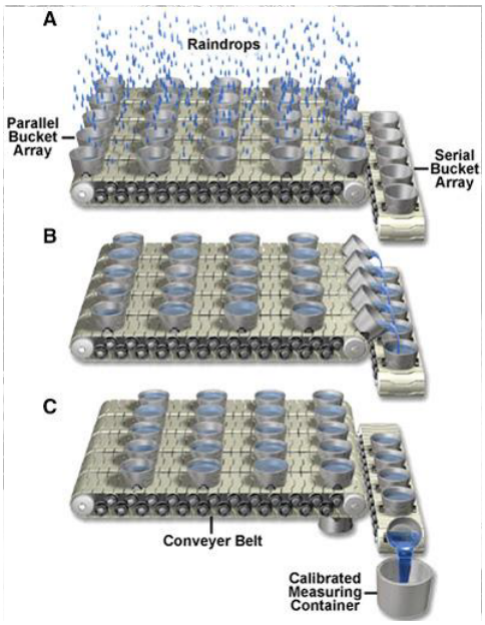

FIGURE 1.8: Analogy to the inner workings of a CCD camera. The water buckets get all filled, and then the right-most line discharges first onto a separated bucket array, which in its turn get emptied, one by one, on a calibrated sensor. This process allows for the identification of the charge -water quantity- on each pixel -water bucket- sequentially.

partitioning a digital image into multiple segments. The goal of such process is to simplify and/or change the representation of an image into something that is more meaningful and easier to analyse. Through segmentation it is possible to alter brightness and contrast in an image. A practical example on how those two variables can be altered is shown in Figure 1.11. The brightness of an image depends on the position in the histogram section selected, while the contrast depends on the width of the selection. Varying those two parameters implies essentially a re-scale of the minimum and maximum values of the grey scale.

1.4 The radiography technique

When performing a radiography on an object, the base result must be properly elaborated before extracting any relevant data from it.

1. Dark field: namely the background noise of the detector and/or camera. This is eliminated by subtracting an image made in absence of radiation field to both the background and the object radiographies.

2. Open beam: Since the radiation field is not necessarily homogeneous, an image in absence of the object allows the normalisation to the background, eliminating any disturbance or dis-homogeneity, as well as differences in efficiency between the camera and scintillator.

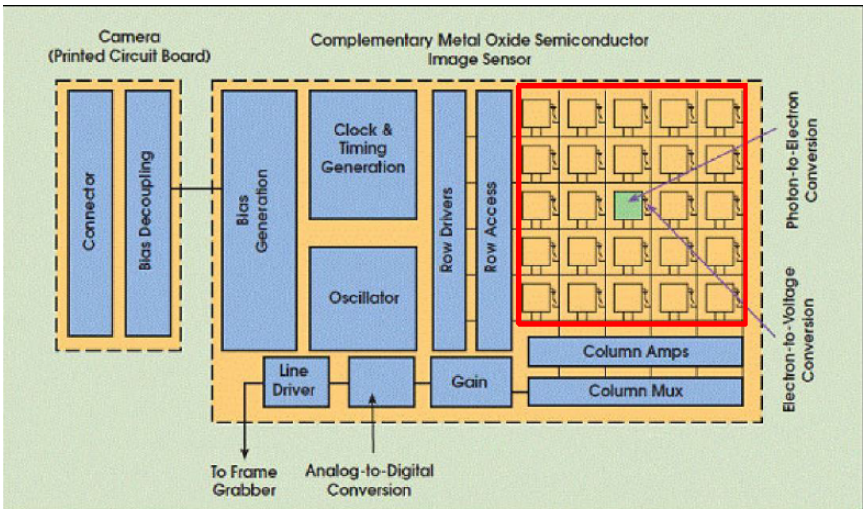

FIGURE 1.9: Inner workings of a CMOS sensor. Further details are explained in the text.

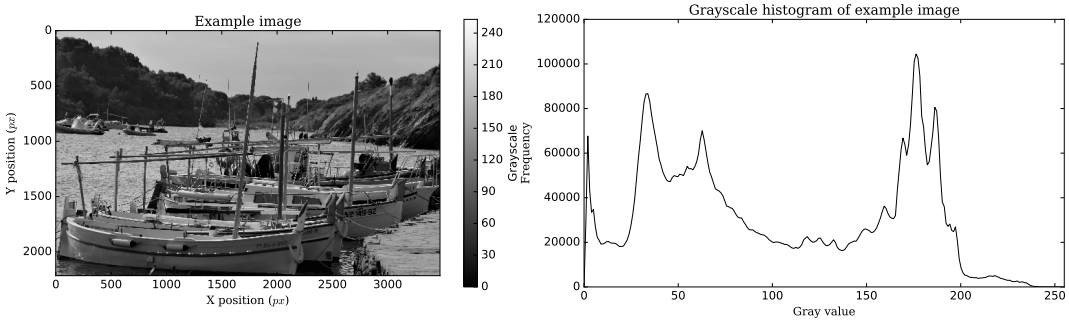

FIGURE 1.10: Example of the histogram of a grayscale image.

Overall, the elaboration of an image goes as follows:

$$I_{norm} = \frac{I - I_{DF}}{I_0 - I_{DF}} \tag{1.9}$$

Where I_{norm} stands for the normalised radiography, I and I_0 for image and open beam image respectively, and I_{DF} the dark field image[6].

1.5 The tomography technique

A tomography is a three dimensional system composed by an array of two dimensional images separated by a distance of one pixel along a normal axis, as depicted in Figure 1.12. A tomography requires the combination of n radiographic images of a sample taken at different angles (projections) with respect to a fixed axis which is itself perpendicular to the incoming radiation beam axis. The information within a single projection is relative to the direction (angle) that relates the source and detector. The usual method to create the tomography implies a rotary stage of the sample, thus generating

[6]In photography and specially in astronomical photography there are also other calibration images required, such as the flat field or the bias images, but in radiological images those elements are not necessary due to the imaging conditions.

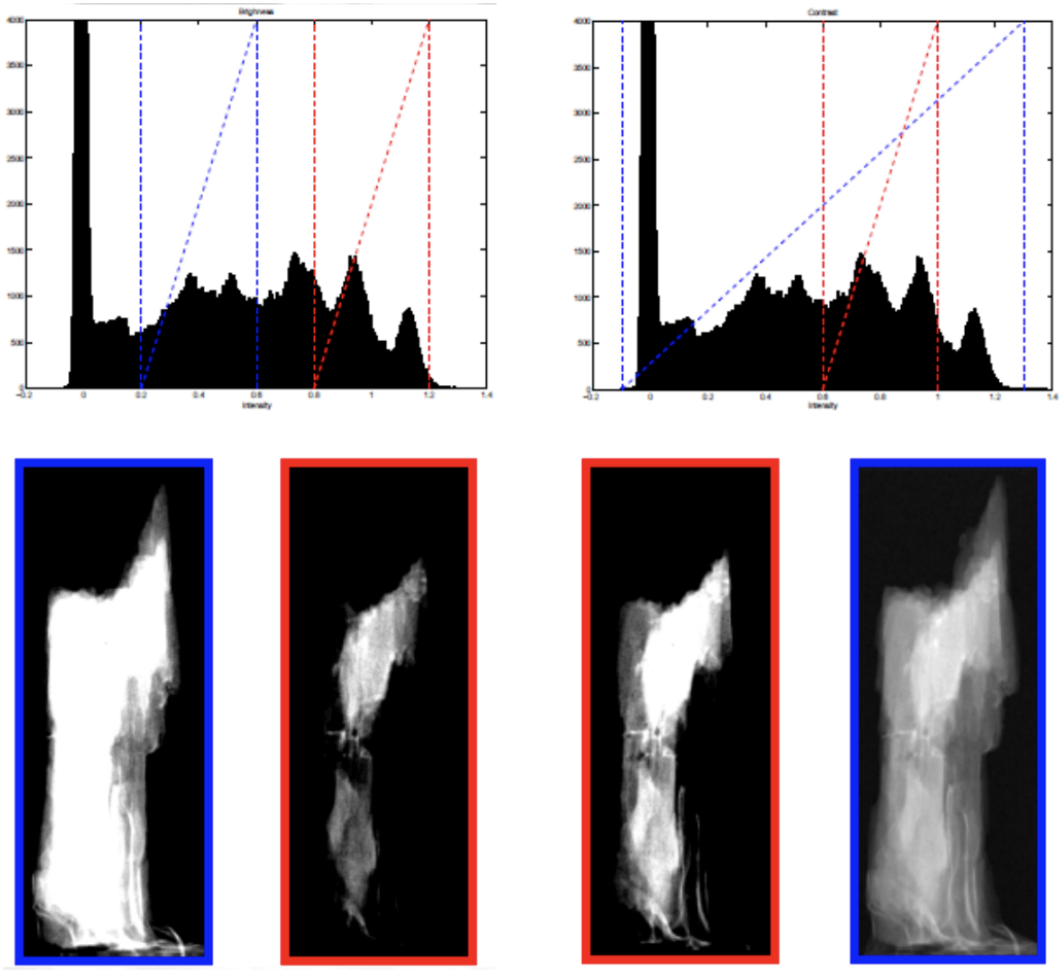

FIGURE 1.11: **Left**: Low brightness (blue) and high brightness (red). The dynamic range is compressed between the two limits, highlighting a narrow range of grayscale intensities. **Right**: Narrow contrast (red) and wide contrast (blue). A wider contrast smooths the dynamic range of the image over a larger set of values, delivering an more blurry image as a result.

the projections by rotating the sample instead of the detector or beam. Each image taken at a certain angular position comes organised in a sinogram[7]. Figure 1.13 shows how the sinogram is created.
The mathematical tool that allows the tomographic reconstruction from a sinogram is called the projection-slice theorem [4], which states that the Fourier transform of a projection of a two-dimensional function into a one-dimensional line is identical to the slice through the origin of a two-dimensional Fourier transform, parallel to the projection line. In mathematical terms:

$$F_1 P_1 = S_1 F_2 \tag{1.10}$$

Where F_1 and F_2 are the one and two-dimensional Fourier transforms, P_1 is the projection operator and S_1 is the slice operator. This same concept can

[7]The name is due to the fact that the Radon transform of an off-centre point source is a sinusoid. As a result of that, the Radon transform of a number of small objects appears on a graph as diffused sine waves with a variety of amplitudes and phases.

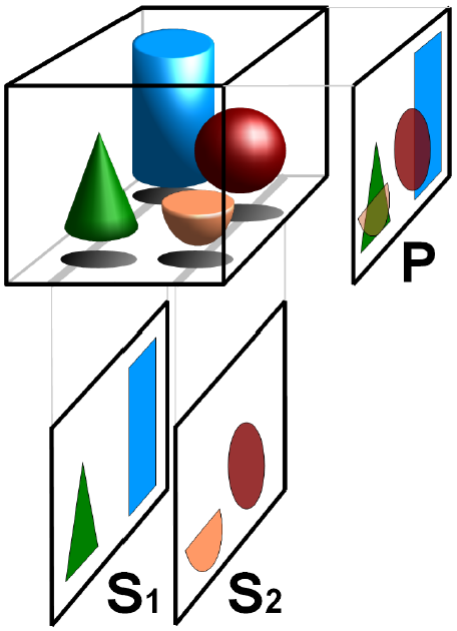

FIGURE 1.12: P stands for the radiographic projection, while S_n is the n^{th} tomographic slice.

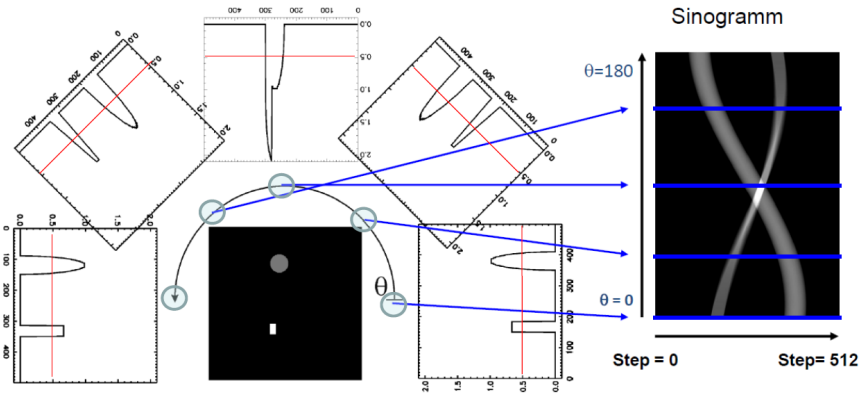

FIGURE 1.13: Step-by-step creation of a sinogram

be applied to higher dimensions ($F_m P_m = S_m F_N$). The projection is typically obtained with the Radon transform [5], which gives as result a series of bi-dimensional images perpendicularly distributed with respect to the rotation axis of the sample (slices).
The reconstruction of the image itself is an *inverse problem* [6], similar to the calculation of the density of the Earth from measurements of its gravity field or the neutron spectrum deconvolution from a Bonner sphere set of measurements [7]. To solve it, one of the most used (by a wide margin) techniques is the Filtered Back-Projection (FBP), represented in Figure 1.14.
The algorithm itself works as follows[8]:

1. It sums each of the n images (one per each angle θ).
2. It measures the projection $P_\theta(t)$.

[8] A full explanation of the algorithm is found in [8]

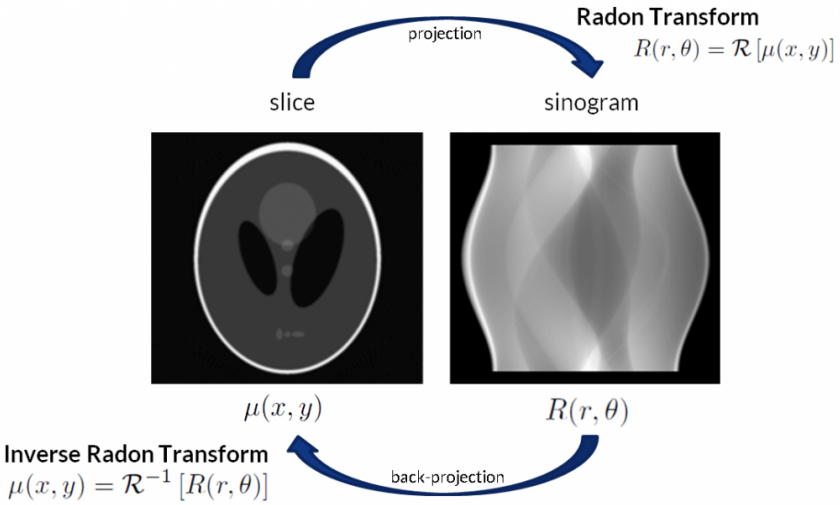

FIGURE 1.14: Representation of the Filtered Back-Projection algorithm.

3. It applies the Fourier transform to obtain $S_\theta(w)$.
4. It multiplies the items by the weighting function $\frac{2\pi|w|}{n}$
5. It sums over the image plane the inverse Fourier transforms of the filtered projections.

In this chapter the elements conforming a radiography set-up have been defined, along with the figures of merit which physically describe the system. After the overview of the hardware used for data acquisition and the definitions of radiography and tomography, the following chapter will be dedicated to the numerical techniques used to determine the spatial resolution from an image.

Chapter 2

Theoretical methods to evaluate the image resolution

One of the key characteristics of any imaging system is the image resolution that it can provide. The image resolution is grossly defined as the amount of detail a single image holds. This definition, though, fails to specify which aspect of the image is being studied. A common misconception is to use the term "resolution" while implying "pixel count", since the number of pixels is only a component of the spatial resolution, not the overall factor. Throughout this thesis, the term "resolution" will be used to refer to the spatial resolution of the image, found as the combination of the penumbra and the pixel size projected to the scintillator screen, following the equation 1.7.
Figure 2.1 depicts the optical setup from the imaging system, where D is the width of a single collimator channel, L is the length of any channel, s the distance between the exit window of the collimator and the object, l the distance between the object and the scintillator and σ_{pen} the penumbra generated by the geometry of the system at the detector.

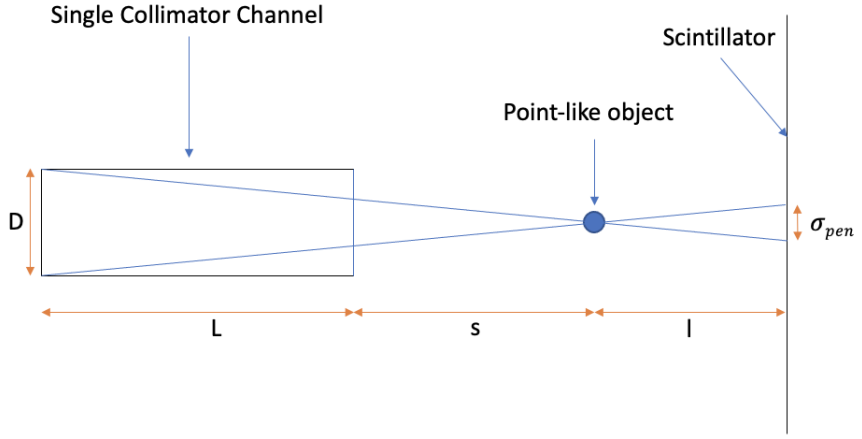

FIGURE 2.1: Design of the imaging setup with the variables employed.

The penumbra can be easily calculated through:

$$\sigma_{pen} = \frac{lD}{L+s} \tag{2.1}$$

The pixel size projected on the scintillator screen can be experimentally determined by placing a millimetric sheet in place of the scintillator and taking

a fast photography. In the ANET imaging instrument[1], a single pixel has a squared size of $47.9\mu m$. Through equation 2.1 it is possible to determine the theoretical value of the spatial resolution given a certain setup configuration. To experimentally measure the parameter, there are two widespread strategies: by optical means or numerical analysis.
To optically determine the spatial resolution of an image, three common instruments are:

1. Bar pattern: sequence of precise lines with a known width and separation through which the value of the spatial resolution can be directly deduced.

2. Siemens star: radial spoke structure, with concentrical circles at precise distances. The measurement of the resolution comes by the point in which the eye cannot distinguish the separation between consecutive spokes.

3. Knife edge: A high contrast sample which creates a good edge to evaluate the Edge Spread Function.

Nevertheless, more accurate measurements of spatial resolution can be obtained through numerical methods. When a good signal-to-noise-ratio and large statistics are available, two methods can be used: the Modulation Transfer Function (MTF) and the Fourier Ring Correlation (FRC). Both methods rely on the Fourier Transform methodology. That is the object of the following section.

2.1 The Discrete Fourier Transform

The Fourier transform is a mathematical operation which decomposes functions depending on space or time into spatial frequency or time frequency. It can be applied to any kind of function or signal, and in this case will be applied to determine the resolution of an image.
The Fourier transform is an essential instrument for digital image processing and it allows the decomposition of an image into its sine and cosine components, resulting in a representation of the image in the frequency domain.
Considering only digital images, the mathematical function employed is the Discrete Fourier Transform (or DFT):

$$F(k,l) = \sum_{i=0}^{N-1} \sum_{j=0}^{N-1} f(i,j) e^{i2\pi \left(\frac{ki}{N} + \frac{lj}{N}\right)} \tag{2.2}$$

Where $f(a,b)$ is the value of the image in the spatial domain and the exponential term is the basis function for the frequency domain. $F(k,l)$ is composed by a variety of sine and cosine waves with increasing frequency. $F(0,0)$ corresponds to the average frequency, while $F(N-1,N-1)$ is the highest frequency.

[1] A commercial 16-bit cooled camera, with a resolution of 2759 x 2200 pixels, and a pixel size of 4.54 x 4.54 μm^2.

The DFT is a double sum, implying a N^2 computational complexity. By disassembling the equation into single-dimensional DFTs and applying the various FFT (Fast Fourier Transform) algorithms present in literature, the complexity can be reduced down to $Nlog_2N$.
The DFT result is a complex value image in which each pixel has information regarding magnitude and phase of the Fourier Transform, corresponding to the real and imaginary values respectively. Most of the information of the image is within the magnitude value, which implies that the imaginary component is often discarded in the image processing. This value is, though, important to apply the proper inverse Fourier Transform to bring the information back from the frequency domain to the spatial domain.

2.1.1 Extracting information from a DFT

Through the Fourier Transform it is possible to access the geometrical characteristics of the spatial domain of an image. Many DFT algorithms shift the frequency domain image in such a way that the $F(0,0)$ is found at the centre of the image[2]. This eases the interpretation of the image, as the average frequency is placed at the centre of the image, and the farther away from it, the higher its corresponding frequency.
As an example of the DFT, figure 2.2 shows an image taken at a bay, with some boats, passed through a black-and-white filter.
The Fourier transform of that figure delivers a complex image in which the

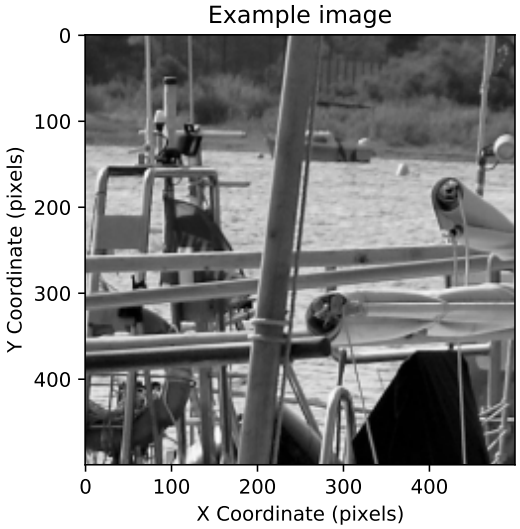

FIGURE 2.2: Crop from a black-and-white image taken at the gulf of Roses, in the northern Catalonia.

pixels are composed by magnitude and phase components. Figure 2.3, on the left, shows the resulting magnitude from the Fourier Transform of figure 2.2. It is completely dark, as the range of values is far too great to appreciate the data. To compress the dynamic range of the image, a logarithmic operator is applied to all the pixels. This enhances the low intensity pixels compared

[2]Labview IMAQ FFT function automatically shifts the image, while Python, for example, requires a specific shift function.

to the high-intensity ones. As the target is an 8-bit output, the logarithmic operator applied will be:

$$Q(i,j) = \frac{255}{log(1+|R|)} log(1+|P(i,j)|) \tag{2.3}$$

Where R is the greatest magnitude value found in the DFT and $P(i,j)$ and $Q(i,j)$ are the former and final pixel values respectively. The transformation,

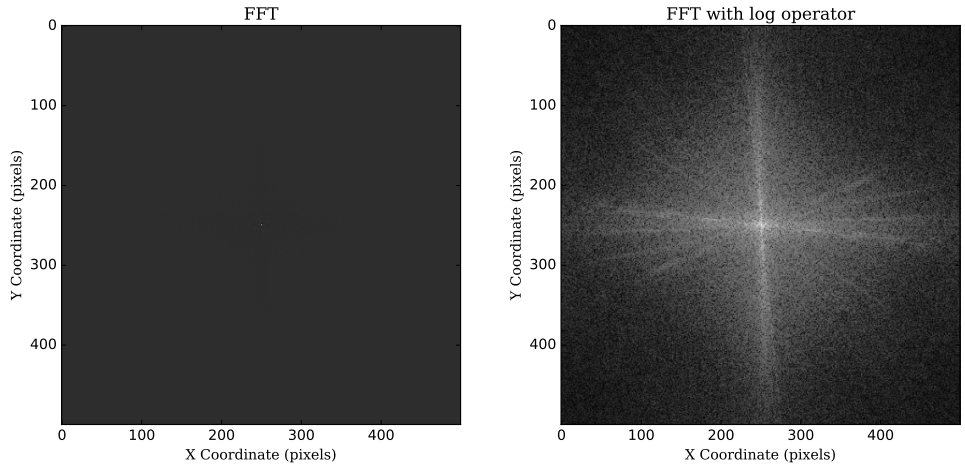

FIGURE 2.3: Magnitude of the Fourier Transform without the logarithmic operator (left) and with it (right).

resulting in the right component of figure 2.3, shows that mostly all the frequencies are present, and their magnitudes decrease at higher frequencies. This implies that higher frequencies contain more image information. The result also highlights some predominant directions in form of straight lines in different angles on the Fourier space. This is due to regular patterns on the spatial domain image.

2.1.2 Noise effect on the DFT

The technique of relevance on this section heavily relies on the difference made by the noise upon the signal in an image. For this reason, it is important to understand the impact of the noise when studied on the Fourier space.
In order to analyse the impact of the noise on the Fourier transform, some Gaussian noise has been added to the original example image. With a variance of 10^{-3} and an average of 0, the comparison result is shown on figure 2.4.

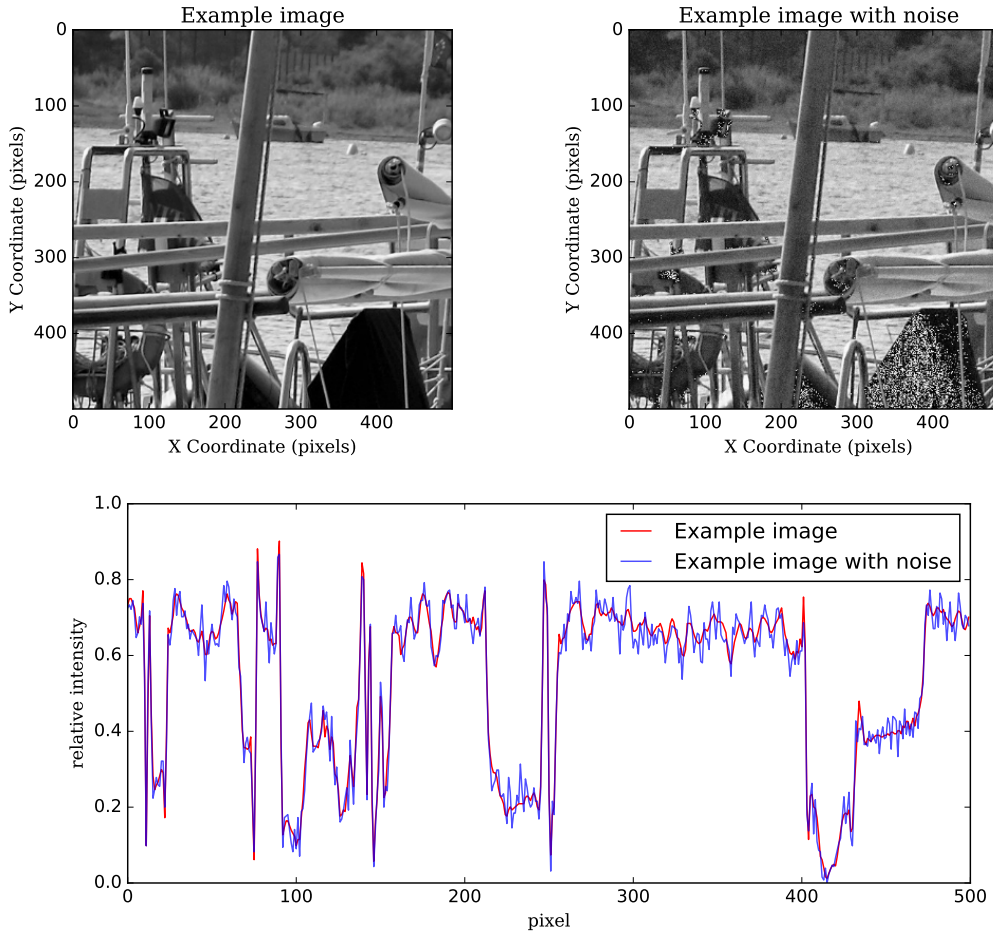

FIGURE 2.4: Comparison between the original image (top-left) and the noisy version (top-right), and a plot showing the relative intensity at Y = 200 in both images (bottom).

The Gaussian noise applied on the image is barely perceptible by the naked eye, or even by the linear plot on the same segment of both images. This is partially due to the fact that the variance was very small. The area in which the applied noise has the biggest effect is in the lower-right, where there is a black cloth. As the value of the pixels in the region is very small, the addition of the Gaussian noise on top creates a more distinguishable difference, although the greyscale values are still similar.

Even though the visual effect on the image is dim, this is not the case on the frequency domain. The noise addition, even though it has an average of 0, applied to the whole image alters the frequencies, pushing them towards a greater uniformity. This is shown in figure 2.5.

Figure 2.5 is the comparison between the Discrete Fourier Transform of the original image and that of the noisy image. The biggest difference between both images is the smoothing of the different frequencies. From the Fourier space point of view, some of the secondary predominant directions present at the original image no longer have enough contrast to be discernible. This smoothing is further noticed when compared on the plot profile, which show a clear difference between both images. On the example image, there is a clear gap between the central region and the border, and it coincides with

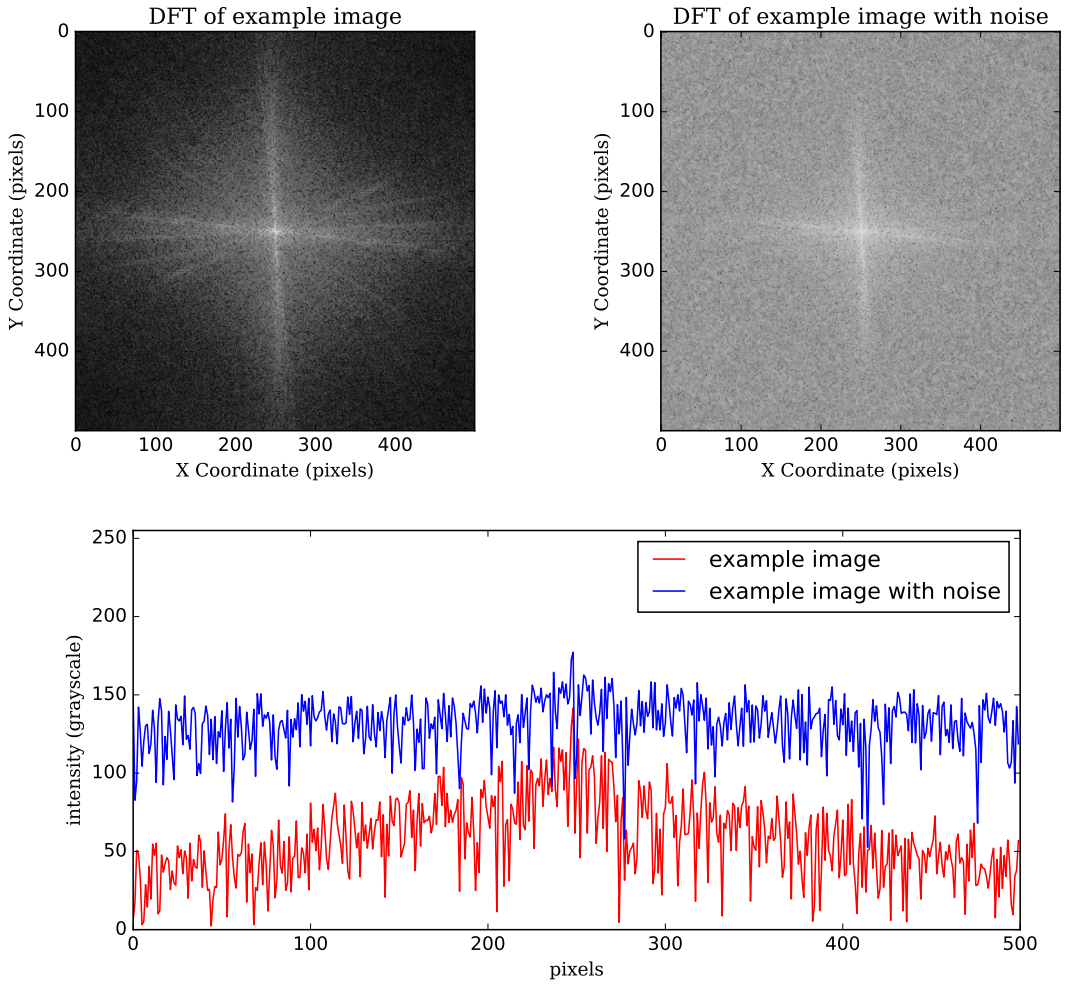

FIGURE 2.5: Discrete Fourier Transform applied to the original example image (top-left) and the DFT applied to the noisy image (top-right). Plot showing the greyscale intensity (on a 0-255 scale) at Y = 150 for both images (bottom).

clear higher bands of frequency on the DFT image. On the example image with noise added, the profile is more uniform. This effect is due to the noise populating all the frequency spectrum, creating a uniform sheet which hides the structures before visible.
As the impact of the noise on the image is this great on the Fourier space, analysing the resolution on the image by comparing two identical images, different only due to the noise component, is more reasonable on the frequency domain. This is the base of the Fourier Ring Correlation technique.

2.2 The Fourier Ring Correlation

The Fourier Ring Correlation (FRC) - or Fourier Shell Correlation (FSC), for the 3-D case - is a metric used for computing the normalised cross-correlation coefficient between two areas - or volumes - as a function of the spatial frequency. It does not depend any *a priori* assumption regarding the nature of the signal or noise. Following the definition from the former author, Marin

van Heel, it follows: "The FRC is a one-dimensional curve showing a high correlation level at the low resolution end, gradually dropping towards zero at higher spatial frequencies, and finally oscillating around the zero mark close to the Nyquist frequency[3] where only random correlations should be present." [9–11].
This metric is calculated through the equation:

$$FRC_{12}(r_i) = \frac{\sum_{r \epsilon r_i} F_1(r) \cdot F_2(r)^*}{\sqrt{\sum_{r \epsilon r_i} |F_1(r)|^2 \cdot \sum_{r \epsilon r_i} |F_2(r)|^2}} \tag{2.4}$$

In which the $FRC_{12}(r_i)$ is the value for the FRC between image (or signal) 1 and 2 on the i^{th} ring r_i. $F(r)$ is the complex structure factor at position r in the Fourier space. The sum is done over all the pixels (or voxels in case of 3-D) contained in the ring r_i.
This technique is based on the assumption that any pixel, on the Fourier domain, is composed by a signal component S and a noise component N. Assuming a common signal value between both images, the only difference will be the noise.
The Fourier Ring Correlation, as the name states, is essentially a correlation function between identical rings in the frequency domain of two images. Each ring, gets equation 2.4 applied, and it leads to a binned histogram in which the X axis represents the inverse of the resolution, while the Y axis delivers information regarding the correlation between both images.
In order to determine the point in which the spatial resolution is found using the FRC technique, it is necessary to establish a threshold criterion based on the distinction between the signal and the noise.

2.2.1 Threshold criteria

There are, in literature, many different criteria to determine the appropriate resolution threshold on the FRC or FSC curves. Two main categories are:

1. Fixed point curves: setting a single value on the FRC function to determine the threshold. It is easy to apply but fails to account for the variability induced by the number of pixels/voxels. Two common cases of fixed value threshold are 0.5 [12, 13] and 0.143 [14].

2. Function threshold: A non-constant curve based on the distinction between signal and noise, the two most common ones are the σ curves and the $T_{1/2}$, also known as "half-bit information" curves.

σ curves were initially introduced as an improved representation of the quality of the data with respect to the fixed value curves [15]. The currently most widely used threshold curve linked to 3D FSC data is the σ-factor curve:

$$\sigma(r_i) = \frac{\sigma_{factor}}{\sqrt{n(r_i)/2}} \cdot \sqrt{n_{asym}} \tag{2.5}$$

[3] Half of the sampling rate. In an image it would be $1/2\ px^{-1}$.

Where $\sigma(r_i)$ is the value of the threshold curve at a certain ring or shell r_i, σ_{factor} is the number of standard deviations above the expected random noise fluctuations - usually 2 or 3 -, $n(r_i)$ is the number of voxels in the shell and n_{asym} the number of asymmetric units within the given pointgroup symmetry (1 for an asymmetrical object, up to 60 for icosahedral symmetry) [10, 16].
The most accurate threshold curve, though, is mathematically extracted from the behaviour of the system-to-noise ratio (SNR) within the Fourier space. The mathematical demonstration is based on the work by Van Heel and Shatz [10]:
Considering any pixel within the Fourier space to be composed by a complex signal component S and an uncorrelated noise component N, the value S on both images considered will be identical, while N will vary:

$$\begin{aligned} F_1(r) &\approx S(r) + N_1(r) \\ F_2(r) &\approx S(r) + N_2(r) \end{aligned} \tag{2.6}$$

Applying the FSC formula, based on this equations leads to:

$$\begin{aligned} FSC_u(r_i) &\approx \sum_{r \epsilon r_i} F_1(r) \cdot F_2(r) \\ &\approx \sum_{r \epsilon r_i} S^2(r) + \sum_{r \epsilon r_i} S(r) \cdot N_1(r) + \sum_{r \epsilon r_i} S(r) \cdot N_2(r) + \sum_{r \epsilon r_i} N_1 \cdot N_2(r) \end{aligned} \tag{2.7}$$

Where $FSC_u(r_i)$ reffers to the uncollimated FSC at the shell r_i. In order to properly understand the functioning of the FRC and FSC, the four terms that compose the equation must be taken into consideration. The average of the squares for the signal component is:

$$\overline{S^2}(r_i) = \frac{1}{n(r_i)} \cdot \sum_{r \epsilon r_i} S^2(r) \tag{2.8}$$

And the same can be applied for the noise term:

$$\overline{N^2}(r_i) = \frac{1}{n(r_i)} \cdot \sum_{r \epsilon r_i} N^2(r) \tag{2.9}$$

To understand this equation it is important to note that the cross-term between the two noise components is:

$$\overline{N_1 N_2}(r_i) = \frac{1}{n(r_i)} \cdot \sum_{r \epsilon r_i} N_1(r) \cdot N_2(r) \approx \frac{1}{\sqrt{n(r_i)}} \cdot \overline{N^2}(r_i) \tag{2.10}$$

The cross-term between signal and noise is:

$$\overline{SN_a}(r_i) = \frac{1}{n(r_i)} \cdot \sum_{r \epsilon r_i} S(r) \cdot N_a(r) \approx \frac{1}{\sqrt{n(r_i)}} \cdot \overline{S^2}(r_i) \cdot \overline{N^2}(r_i) \tag{2.11}$$

where $\overline{S}(r) = \sqrt{\overline{S^2}(r)}$ and $\overline{N}(r) = \sqrt{\overline{N^2}(r)}$. Instinctively, it is possible to fall on the assumption that the signal and noise not being correlated implies

that the cross-terms $\overline{SN_1}$ and $\overline{SN_2}$ are equal to 0. The signal and the noise not being correlated leads to random correlations within the cross-terms, which do not have a zero expectancy value but rather exhibit a similar statistical behaviour to that of the cross-term between the random noise between two volumes ($N_1 N_2$). This means that, from the point of view of the noise, the signal itself is noise. The assumption that the cross-term $\overline{SN_1}$ and $\overline{SN_2}$ have an expectation value of 0 can only happen if the two components are orthogonal, which is not the same as uncorrelated.
By substituting the expectation values calculated to the main equation 2.7 the result is:

$$FSC_u(r_i) \approx n(r_i) \cdot \overline{S^2}(r_i) + 2\sqrt{n(r_i)} \cdot \overline{N}(r_i) \cdot \overline{S}(r_i) + \sqrt{n(r_i)} \cdot \overline{N^2}(r_i) \tag{2.12}$$

The expected behaviour of the normalising factor is:

$$\begin{aligned} FSC_n(r_i) = &\sqrt{\Big(\sum_{r \epsilon r_i} S^2(r) + \sum_{r \epsilon r_i} 2 \cdot S(r) \cdot N_1(r) + \sum_{r \epsilon r_i} N_1^2(r)\Big)} \\ &\cdot \sqrt{\Big(\sum_{r \epsilon r_i} S^2(r) + \sum_{r \epsilon r_i} 2 \cdot S(r) \cdot N_2(r) + \sum_{r \epsilon r_i} N_2^2(r)\Big)} \end{aligned} \tag{2.13}$$

Which result in:

$$FSC_n(r_i) \approx \sum_{r \epsilon r_i} S^2(r) + \sum_{r \epsilon r_i} 2 \cdot S(r) \cdot N(r) + \sum_{r \epsilon r_i} N^2(r) \tag{2.14}$$

Applying the expectation values previously calculated:

$$FSC_n(r_i) \approx n(r_i) \cdot \overline{S^2}(r_i) + 2\sqrt{n(r_i)} \cdot \overline{N}(r_i) \cdot \overline{S}(r_i) + n(r_i) \cdot \overline{N^2}(r_i) \tag{2.15}$$

From this result we can combine equation 2.12 and 2.15 to obtain:

$$\begin{aligned} FSC(r_i) &= \frac{FSC_u(r_i)}{FSC_n(r_i)} \\ &\approx \frac{n(r_i) \cdot \overline{S^2}(r_i) + 2\sqrt{n(r_i)} \cdot \overline{N}(r_i) \cdot \overline{S}(r_i) + \sqrt{n(r_i)} \cdot \overline{N^2}(r_i)}{n(r_i) \cdot \overline{S^2}(r_i) + 2\sqrt{n(r_i)} \cdot \overline{N}(r_i) \cdot \overline{S}(r_i) + n(r_i) \cdot \overline{N^2}(r_i)} \end{aligned} \tag{2.16}$$

From this equation the behaviour of the FSC can be studied. The no-signal limit found at $S \to 0$ brings:

$$FSC_{S \to 0}(r_i) = \frac{0 + 0 + \sqrt{n(r_i)} \cdot \overline{N^2}(r_i)}{0 + 0 + n(r_i) \cdot \overline{N^2}(r_i)} \approx \frac{1}{\sqrt{n(r_i)}} \tag{2.17}$$

This behaviour is expected on the no-signal regime, in which the noise evolves as the inverse of $\sqrt{n(r_i)}$. In the same fashion, the no-noise limit can be calculated:

$$FSC_{N \to 0}(r_i) = \frac{n(r_i) \cdot \overline{S^2}(r_i) + 0 + 0}{n(r_i) \cdot \overline{S^2}(r_i) + 0 + 0} \approx 1 \tag{2.18}$$

The FSC tends to unity when the noise is null, which implies that the two volumes are identical, as they should, given that the only difference between the two was the noise component.
To derive the formula for the threshold from 2.16, there are two actions to be taken:

1. Divide both numerator and denominator by $n(r_i) \cdot \overline{N^2}(r_i)$
2. Apply the definition of signal-to-noise ratio $SNR(r_i) \equiv \frac{\overline{S^2}(r_i)}{\overline{N^2}(r_i)}$.

Leading to:

$$FSC(r_i) = \frac{SNR(r_i) + 2/\sqrt{n(r_i)} \cdot \sqrt{SNR(r_i)} + 1/\sqrt{n(r_i)}}{SNR(r_i) + 2/\sqrt{n(r_i)} \cdot \sqrt{SNR(r_i)} + 1} \tag{2.19}$$

Through this function it is possible to determine the resolution r_i at which the Fourier space achieves a certain signal-to-noise ratio SNR_T.
To place a simple example, following [10], if the target was $SNR(r_i) = 1$, the SNR value on each dataset shall be 0.5, as the total reconstruction, being the sum of the two datasets has twice the SNR of a single dataset. Placing those values inside 2.19 results in:

$$T(r_i) = \frac{0.5 + 2.4142 \cdot 1/\sqrt{n(r_i)}}{1.5 + 1.4142 \cdot 1/\sqrt{n(r_i)}} \tag{2.20}$$

The two limits of this function are 1 when r_i approaches 0, case in which there is only one pixel/voxel in the function, and $1/3$ when the number of pixels tend to infinity.
The point in which the threshold curve and the FSC curve intersect in this example has a SNR of unity, thus the average information content, as defined by Claude Shannon in 1984 [17], will be:

$$log_2(1 + SNR) = log_2(2) = 1bit \tag{2.21}$$

And through that calculation, the curve in 2.20 receives the name of T_{1-bit} resolution curve. The more commonly used criterion, though, is the $T_{\frac{1}{2}bit}$ curve, which is extracted from:

$$\frac{1}{2}bit = log_2(1.4142) = log_2(1 + SNR) \tag{2.22}$$

Which leads to:

$$T_{\frac{1}{2}bit} = \frac{0.2071 + 1.9102 \cdot 1/\sqrt{n(r_i)}}{1.2071 + 0.9102 \cdot 1/\sqrt{n(r_i)}} \tag{2.23}$$

Same as with 2.20, when the number of pixels approaches 0, the curve tends to unity, and when the function is evaluated far from the origin, the threshold tends asymptotically to $\frac{0.2071}{1.2071} = 0.1716$.
This threshold criteria takes into consideration the cross terms between signal and noise, and takes into consideration the number of pixels present on

the rings/shells. It also ties the resolution criteria with the basis of information theory proposed by Shannon, constituting a strong argument in favour of this technique in front of alternatives such as the fixed-value curves.

2.2.2 Example of an FRC calculation

Applying noise to the example image to generate two different results will allow for the application of the FRC technique to obtain an estimate for the resolution within a controlled example.
The noise applied, in both cases, is a Gaussian noise with a $\sigma^2 = 10^{-3}$. Following the process previously described in 2.2 and 2.2.1. First both images are transformed using the Fast Fourier Transform. Secondly, a number of rings are defined, starting from the centre of the image up to the border (radius equal to half of the image size). From there, applying equation 2.4 on each ring will create a histogram, in which the rings will compose the bins. Knowing the number of pixels in each ring, the half-bit threshold curve is build, delivering the result in figure 2.6.

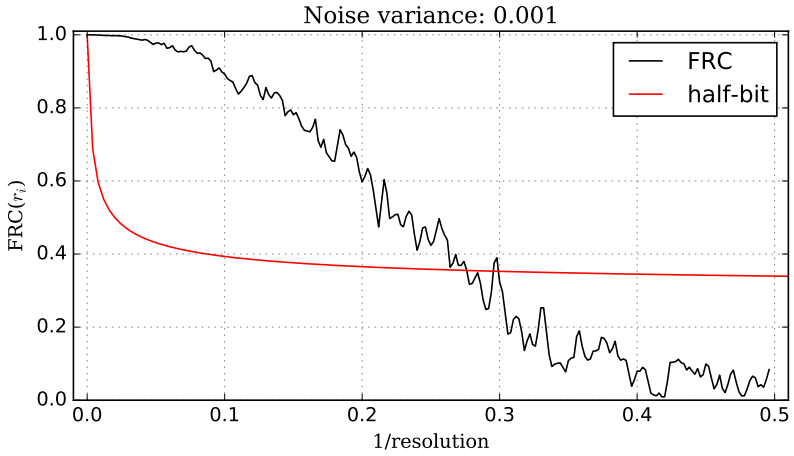

FIGURE 2.6: FRC calculated on the example image with the $T_{\frac{1}{2}bit}$ threshold curve.

Figure 2.6 shows a horizontal axis spanning from 0 to 0.5, corresponding to the extension of the Fourier space, which would be from 0 to N, but shifted to centre the most probable frequency to $\frac{N}{2}, \frac{N}{2}$ instead of $0, 0$. Due to this shift, the space radially spans from 0 to $\frac{N}{2}$. The FRC and threshold curves meet at an inverse resolution of 0.275. The inverse resolution has units of px^{-1}, and assuming (for example purposes) a camera pixel size of $50\frac{\mu m}{px}$, we obtain:

$$(0.275px^{-1})^{-1} \cdot 50\frac{\mu m}{px} = 182\mu m \tag{2.24}$$

Thus the resolution of the image would be $182\mu m$.
It is possible to evaluate the effect of the noise on the FRC calculation by modifying the variance of the Gaussian noise included on the image. In the following example, taking the same starting picture, the FRC calculation has been performed on 4 different noise scenarios: with variances of 10^{-3}, $5 \cdot 10^{-3}$, 10^{-2} and 10^{-1}. Figure 2.7 highlights the same measurement under the

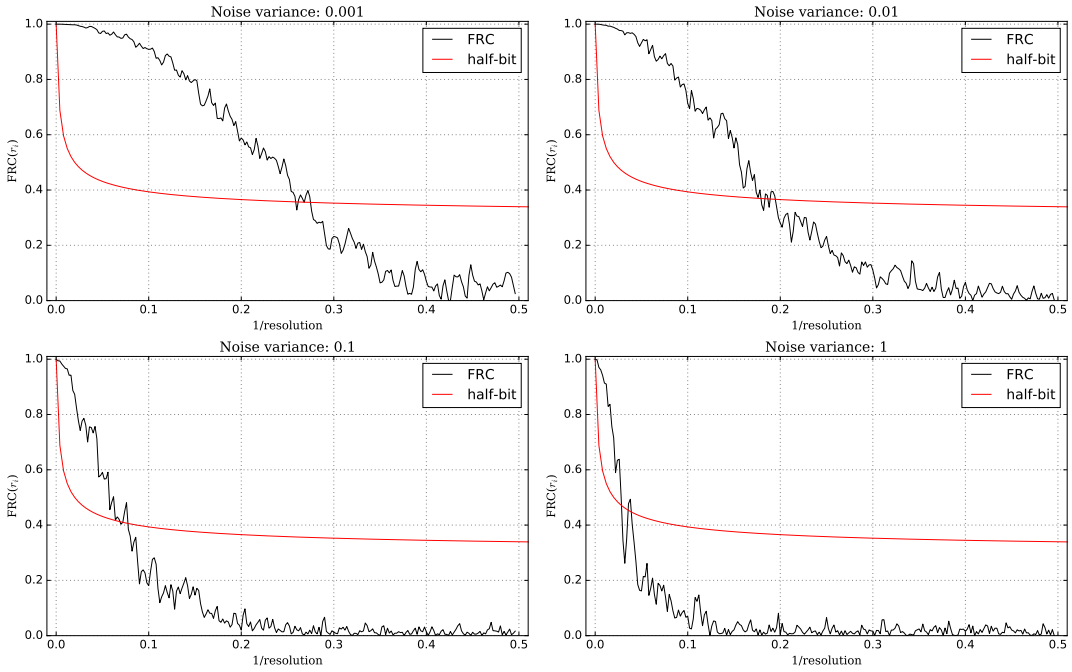

FIGURE 2.7: Four cases of FRC curves measured on the same image under different noise conditions.

4 different noise conditions. From the graphic it can be appreciated the decay on the quality of the signal when increasing the signal-to-noise ratio.

2.3 The Modulation Transfer Function

An alternative method to the Fourier Ring Correlation to evaluate the spatial resolution is the Modulation Transfer Function, or MTF. This method is more widespread than the FRC, in particular in optical and X-Ray imaging fields. The MTF is defined as "the magnitude of the optical transfer function". To understand this definition, some elements need to be disclosed first.

2.3.1 Point Spread Function

The point spread function (PSF) is the response of the imaging system to a point source. The blurring on the image is directly related to the degree of spreading of a point object. Considering the PSF homogeneous over the whole detector, the resulting image can be calculated by the convolution of the true object and the detector's response.
To calculate the PSF on a simple case, two assumptions will be taken: the PSF is independent of the position of the image plane - also known as shift invariant -, and there is no added distortion on the image. Mathematically, the image plane coordinates are directly related to the image plane coordinates through the magnification M:

$$(x_i, y_i) = (Mx_0, My_0) \tag{2.25}$$

From this equation, in which (x_i, y_i) are the image plane coordinates and (x_0, y_0), the object plane field is defined as:

$$O(x_0, y_0) = \iint O(u, v)\delta(x_0 - u, y_0 - v)dudv \tag{2.26}$$

This equation essentially describes the image as a sum of individual point images. The resulting image is formed as the convolution of the object plane with the PSF:

$$I(x_i, y_i) = \iint O(u, v)PSF\Big(\frac{x_i}{M-u}, \frac{y_i}{M-v}\Big)dudv \tag{2.27}$$

Where the $PSF\Big(\frac{x_i}{M-u}, \frac{y_i}{M-v}\Big)$ is equivalent to the image of the impulse function $\delta(x_0 - u, y_0 - v)$.
The Fourier transform of the PSF results in the Optical Transfer Function.

2.3.2 Optical Transfer Function

The Optical Transfer Function (OTF) is the response to a sinusoidal wave passing through a lens system. As mentioned in the previous section, is defined as a Fourier transform of the PSF. The two components of the OTF are the Modulation Transfer Function (real component) and the Phase Transfer Function (complex component). Considering aberrations on the image as spatially invariant, the OTF can be determined from a line or edge. These alternative patterns give rise to the Line Spread Function (LSF) and the Edge Spread Function (ESF) respectively.
In case of a single line passing through the origin, the 2D Fourier transform of it is an orthogonal line passing through the centre. The OTF then can only be calculated by means of a LSF.
The Edge Spread Function is defined as the 2D Fourier transform of an edge, which is 0 on all points except for a single line, orthogonal to that edge. For the knife-edge technique, a completely opaque object is placed in front of the light source, defining a high-contrast edge. A square section encompassing this edge is selected, and the data within transformed into a 2D array, with each element representing the value of a single pixel. The amplitude of each pixel line parallel to the edge is then averaged and the result normalised, leading to the Edge Spread Function. The mathematical description of the process is:

$$ESF = \frac{X - \mu}{\sigma} \tag{2.28}$$

Where X is the input array, μ the average of each pixel line, and σ the standard deviation of the same pixel line. The first derivative of the ESF is the Line Spread Function:

$$LSF = \frac{d}{dx}ESF(x) \tag{2.29}$$

The OTF is derived from the LSF by applying the 2D Discrete Fourier Transform, as explained at the beginning of the section, and the magnitude of the result is the MTF.

2.3.3 Calculating the MTF on an example

In order to understand the Modulation Transfer Function, an example will be shown of a calculation through the ESF on a knife-edge analysis.

FIGURE 2.8: Image chosen as an example for the MTF demonstration. The clear contrast generates a good edge to calculate the MTF.

The sample figure 2.8 is a good example of a knife-edge analysis, since it has a very well-defined contrast area by means of a gadolinium sheet which completely eliminates the neutrons coming to the scintillator onto a certain area, creating a high-contrast edge from which to analyse the MTF.

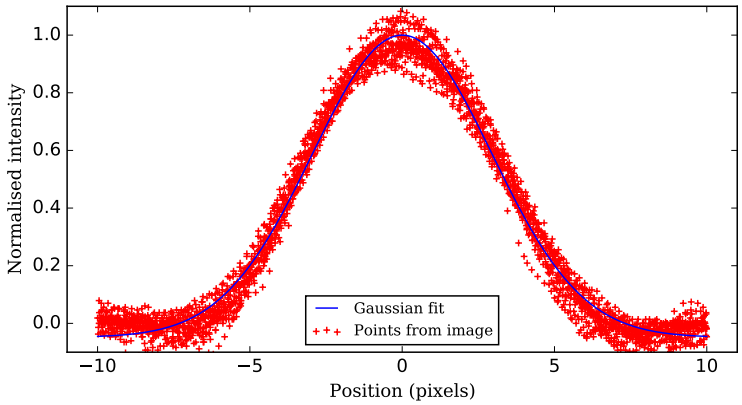

FIGURE 2.9: LSF curve together with the gaussian fit.

The data obtained from a central region in the image is normalised through equation 2.28, obtaining the normalised ESF. The first derivative (equation 2.29) of the ESF is the LSF curve. The Fourier transform of the LSF curve is the OTF, as described previously, the magnitude of which is the MTF, which should be fit with a polynomial of grade 6 [18] (figure 2.9).
From the MTF curve, there is no agreement regarding the proper threshold, as it changes depending on the lens system and requirements of the measurement [19–22]. In this thesis, the threshold has been chosen as 0.155, as a result of an iterative evaluation of the detector contribution to the spatial resolution measurements -explained further on in chapter 6-. Using the same criteria on the example in figure 2.10, applying the threshold of 0.155 on the MTF returns a value of spatial frequency of 0.32. Considering a projected pixel size of 50 μm, this number translates to a spatial resolution of 156.25 μm, calculated using the same procedure as in 2.24.
In this chapter two widely used techniques to evaluate the spatial resolution

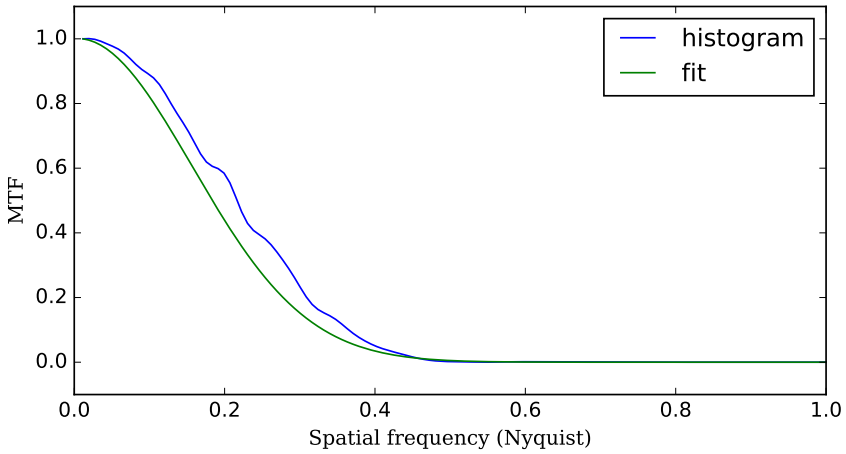

FIGURE 2.10: MTF curve with the polynomial fit of grade 6.

of images have been defined. Both based on the Fourier space, the Fourier Ring Correlation compares the underlying noise between two images while the Modulation Transfer Function analyses the contrast of the image. The next chapter will begin with a historic overview on neutron collimators, and will proceed with the design of the ANET compact neutron collimator.

Chapter 3

Design of the ANET compact neutron collimator

Neutron collimators were invented almost as soon as the neutrons themselves were discovered. The discovery of the neutron was published by James Chadwick in Nature on February, 1932 [23], and the first mention of the concept of "collimating" neutrons appears in the paper, by J.R. Dunning et al., "Interaction of Neutrons with Matter", published in August, 1935 [24], in which it states that "The combination of a paraffin sphere with a canal and defining diaphragms of Cd serves fairly well to collimate a beam of slow neutrons (...)". There appears another mention of a "construction of a source arrangement concentrating the slow neutrons coming from it into a roughly collimated beam" in the article by George A. Fink, published in October, 1936, "The Production and Absorption of Thermal Energy Neutrons". As the concept of a neutron collimator evolves, the first "modern design" appears in 1938, in the paper from L.W. Alvarez: "The production of collimated beams of monochromatic neutrons in the temperature range 300-10 K" [25]. In the article appeared the design for a neutron collimator to couple with a cyclotron in Berkeley. Despite Alvarez having the first collimator built, two years prior the team lead by George A. Fink already studied, through attenuation and collimation, the production of thermal neutron beams [26]. From that point on, the technology branched into a variety of ways: single-piped collimators where developed, creating relatively high-section neutron beams with high L/D factor. In the late 80's, clinical-purposed multi-leaf neutron collimators were created, following the same logic used for their electron or X-ray counterparts [27]. Those multileaf devices are not as much collimators as they are beam shapers, used mainly for radiotherapy purposes [28]. On the front of the single-piped neutron collimators there haven't been any radical advances in either design nor application since their original creation. Figure 3.1 shows one of the first designs of a neutron collimator for research, done in Japan, in the Toshiba Training Reactor by K. Ogawa and N. Wakabayashi back in 1964 [29]. Neutron imaging as a technique got standardised by 1975, when some published articles refer to it as a "norm" and explore alternative ways to approach it and improve the method [30, 31]. The first article which opens the possibility of a portable neutron imaging setup is found in 1987, by the merit of John P. Barton et al. [32], employed to scan small aircrafts. It was further evolved in the DIANA project in 1989 with a joint effort of the LTV Missiles and Electronics Group, in the USA and Airbus from France [33].
On the clinic side, the first patent for a neutron collimator with therapeutic

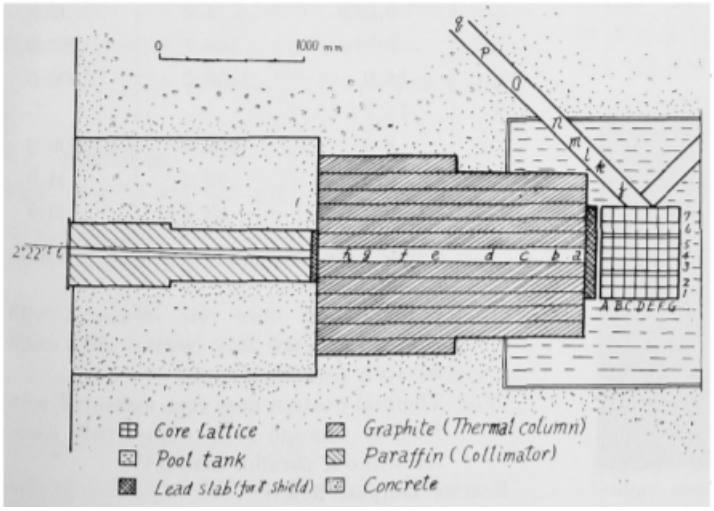

FIGURE 3.1: First image of the article from K. Ogawa and N. Wakabayashi [29] showing the design of a thermal neutron collimator for research purposes.

purposes is found in 1973, held by D. Lundberg [34]. The patent also comprises the variations in material to be used, depending on the desired application - tungsten, hydrogenated silicon, boron...-, to build a single-piped neutron collimator meant for neutron therapy.
The article by Masahito Matsubayashi et al. [35] describes the standard technology on the late 90's for a thermal neutron radiography facility, constructed in the Japan Atomic Energy Research Institute in 1991. The design shown in Figure 3.2 depicts a 3m-long single-piped collimator with a 116 x 266 mm^2 aperture, leading to an L/D factor of 185 and 154 for the horizontal and vertical planes, respectively.
Alternative to the collimation by selection, there exists the treatment of the neutron as a wave, which allows for a different technical approach. By combining the appropriate materials (most usually silicon, nickel or titanium) and creating highly polished layers, the surfaces become neutron reflectors. If the structure is multi-layered, it is named a "supermirror". The concept of a neutron supermirror was first introduced in a paper by F. Mezei in 1976 [36, 37]. On the first 20 years since the discovery, the number of layers on the supermirrors was limited to 20, but the current limit of technology places this number above 16500 [38]. The applications of the supermirrors range from the focusing, collimation or transport to the polarization of neutron waves.

3.1 Current state-of-the-art

At the early 2000's there had been some attempts at creating compact multichannel collimators. The article written by C. Petrillo et al [39] gives a good proof of that fact. Their proposal was the building of a honeycomb-like structure made of a mixture of aluminium and gadolinium. Such work served as basis for a further development of plastic materials rich in Boron-10, which allowed for a more efficient absorption coefficient within similar spatial dimensions, as shown on the work by M. B. Stone et al. [40].

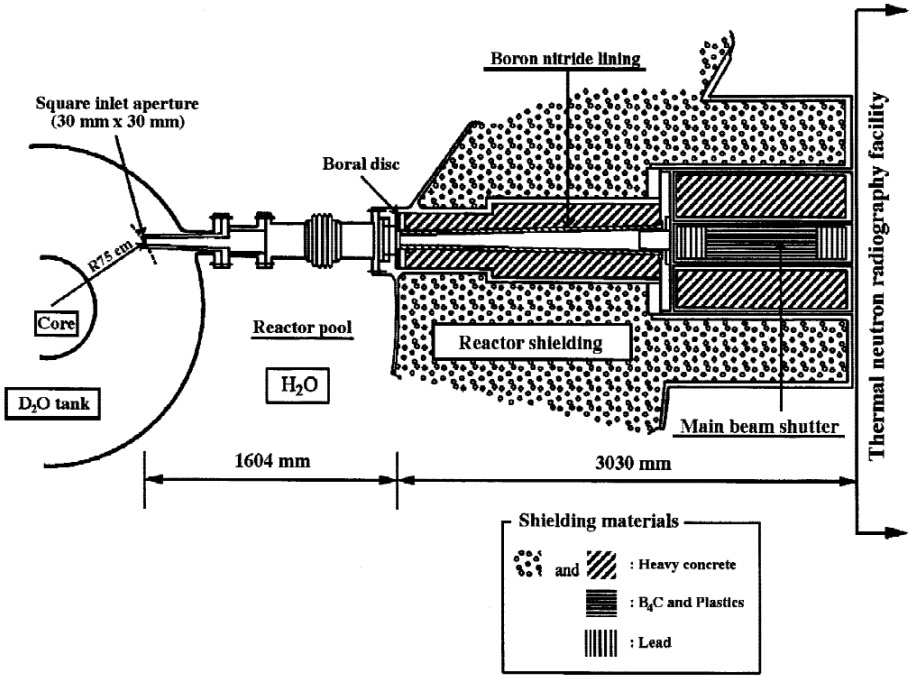

FIGURE 3.2: Design of the cross-sectional view of the 7R beam tube for the JRR-3M research reactor built near Tokai, in the Ibaraki Prefecture, north of Tokyo. The image is extracted from [35].

In the subfield of neutron collimation using multi-channel structures that concerns this project, the current merit for the state-of-the-art appertains to the group of A. Tremsin, in Berkeley. Following the design of the honeycomb collimators existing in nuclear medicine, Tremsin's group hypothesised in the early 2000's an extremely compact neutron collimator which, through selection using a very compact net of micro-channels, could achieve massive L/D factors within a few cm length [41]. The experiments to verify the prototype were published in 2011 [42]. As described on the article, the instrument is a polycapillary collimator with 7mm thickness doped with Boron atoms. It has a channel density of 22000 channels per square millimetre and generates a L/D factor of 1000.

3.2 The ANET Compact Neutron Collimator

Neutron collimators found in imaging or scattering experiments are mostly classical long-tube, pin-hole, Soller slit, multi-plate, or honeycomb type collimators. In each case, the objective of the collimator is to efficiently reduce the dispersion angle of the neutron beam. The main factor to determine the performance of a collimator is the ratio between the transmission length of the channel (L) and its width (D). Typical L/D values are in the range 100-1000 (e.g. [43]).
The ANET - Advanced NEutron Techniques - project aims at creating a Compact thermal Neutron Collimator (CNC) for imaging applications with a length below 1 m and an L/D factor greater than 100. This would allow small or medium-size facilities, such as small reactors or accelerator based neutron sources, to access neutron imaging applications. The core idea behind this

design is to create a multi-channel, scalable structure capable of delivering a highly collimated thermal neutron beam within a short distance. The design consists of an alternate sequence of air and highly absorbant channels arranged in a chessboard section geometry [44]. The absorbing rods are manufactured using a borated polymer purposely created to achieve satisfactory nuclear and mechanical performances. The use of air as transmission channel medium is not limiting the collimation power and it results in an overall simplification of the collimation structure.
The idea behind the concept is to decouple the field of view and the collimation power of the instrument. To do so the device consists of a sequence of air and highly absorbent material channels organized in a chessboard-like section geometry. In order to uniformly illuminate the object under study the instrument will be mounted on a moving stage system. Figure 3.3 shows a 3-D rendering of the collimator.

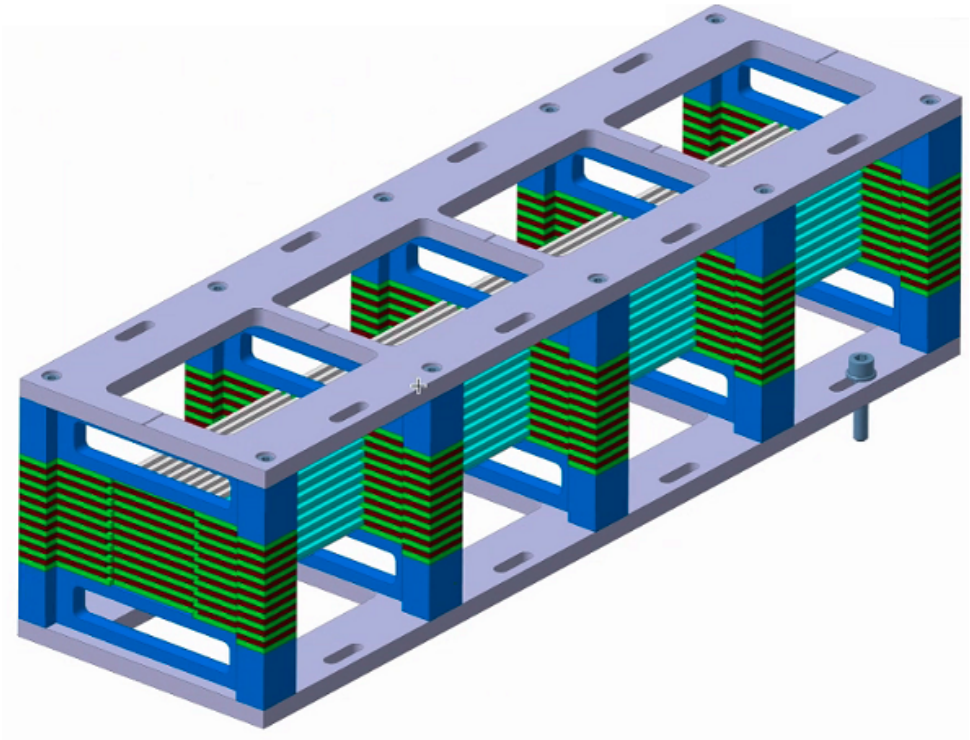

FIGURE 3.3: 3D rendering of the ANET compact neutron collimator.

The collimator consists of four stages arranged inside an aluminium structure to reach the required mechanical rigidity and maintain a low structural activation. Each stage consists of 100 absorbing rods, each one 100 mm in length and with a section of 2.5 x 2.5 mm^2, aligned using laser-cut thin comb-like plates. The expected L/D ratio is 160. The present collimator has been designed to cover an area of 50 x 50 mm^2. Figure 3.4 shows the technical design of the collimator structure. It is possible to increase the total field of view of the collimator or its length just by including more singular elements on a stage or increasing the number of stages itself. The ANET design is scalable both longitudinally and transversely, reaching elevated collimation factors within a limited space. The material of the absorbing rods is a combination of polylactide and boron carbide. Figure 3.5 shows the cross-sections

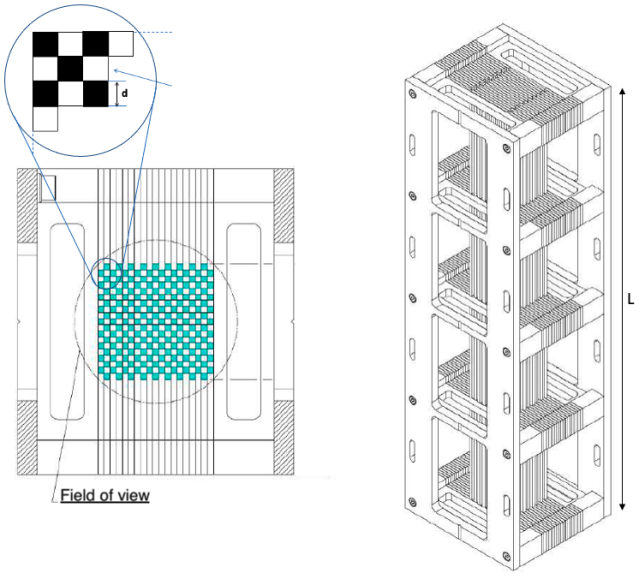

FIGURE 3.4: Design of the collimator structure. D is the dimension of a single channel and L the length of the collimator structure.

(total, absorption and scattering neutron cross-sections respectively) on the material extracted from the simulations performed with MCNP6 transport code [45] using ENDF/B VII.1 cross-section libraries [46]. From the figure, it

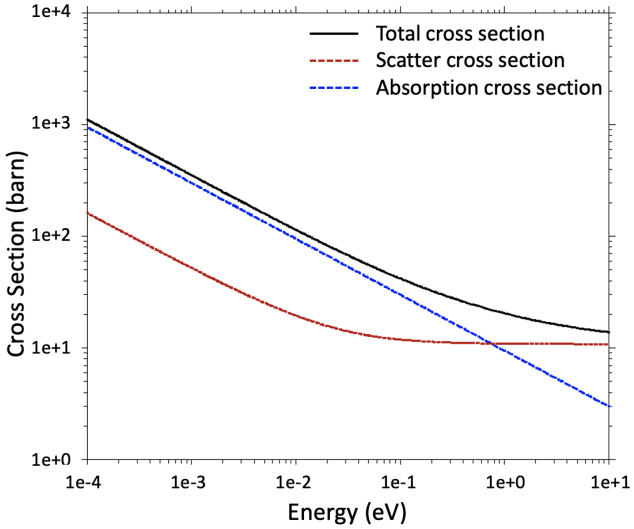

FIGURE 3.5: Total, scatter and absorption cross-section of the material used to build the collimator absorbing rods as a function of the neutron energy.

is clear that the total cross-section in the thermal energy range (at 0.025 eV) is of the order of 10^2 *barn* and mostly due to absorption. This high absorption cross-section makes the material an ideal candidate for building the absorbing elements of the compact neutron collimator.

3.3 The absorbing material performance study

The evaluation of the attenuation and scattering effects induced by the collimator rods, taking into account their composition with respect to an ideal attenuator has been evaluated using MCNP6. The material of the ANET CNC is a composition of PLA[1] and boron carbide, at a mass ratio between 10 and 15%.
To calculate the mean free path of a neutron through the material the following equation 3.1 is used:

$$\Sigma_T = \sigma_T N \tag{3.1}$$

where Σ_T is the total macroscopic cross-section of the material, σ_T the total microscopic cross-section, N atomic number density, expressed in nuclei over cm^3. Assuming a microscopic total cross section at thermal energies of 100 *barn* (see figure 3.5), the macroscopic cross-section is 1.19 cm^{-1}. Since the mean free path λ of a particle is the inverse of the macroscopic cross-section, this results in a value $\lambda = 8.4mm$. Each rod of the ANET collimator introduces on its longitudinal axis an absorbing factor of $2 \cdot 10^4$. The prototype is expected to have 4 sectors, with a total length of 400 mm, thus providing a very high selection of neutrons with the desired direction. The material with the appropriate multi-channel geometry has been simulated using MCNP6 assuming a 400mm long collimator. In the simulation a monoenergetic thermal source has been assumed with selectable divergences. In order to quantify the material performance the comparison between the normalised number of transmitted neutrons at a certain depth passing through a 50 x 50 mm^2 surface in the case of a multi-channel collimator composed by an ideal absorber (T_{ideal}) and by the real material (T_{real}) has been evaluated. The study has been done specifically at 8cm, 16cm, 24cm, 32cm and 40cm depths and under 5 different source divergences, from 0 degrees up to 2 degrees. The distributions of the ratio T_{ideal}/T_{real} are shown in figure 3.6. The ratio T_{ideal}/T_{real} shall always be smaller than 1, as the ideal collimator will always absorb more neutrons than the real one. An asymptotic behaviour of T_{ideal}/T_{real} towards 1 with increasing depth is expected. At the nominal depth of 40 cm the ratio is above 0.95 for all the initial beam divergence scenarios. Figure 3.6 also shows that the effect of neutrons laterally exiting their initial channel tends to be minimised with the increase of the collimator's length.

3.4 The Compact Neutron Collimator method of operation

One feature of the chessboard-like design of the compact neutron collimator is the alternate structure of light and dark areas due to the geometry. In order to have each part of a sample uniformly illuminated, the instrument needs to be moved with respect to the sample. At least two images taken with a translation equivalent to a channel width from one another are needed. Figure 3.7 highlights this concept, in which the combination of two images with the collimator placed in compatible positions eliminates the chessboard pattern as a result. More sophisticated techniques will be studied in order to optimise the quality and resolution of the neutron radiographies, minimising

[1] Polilactide Acid, a rigid thermoplastic very easy to manipulate, widely used for 3D printing.

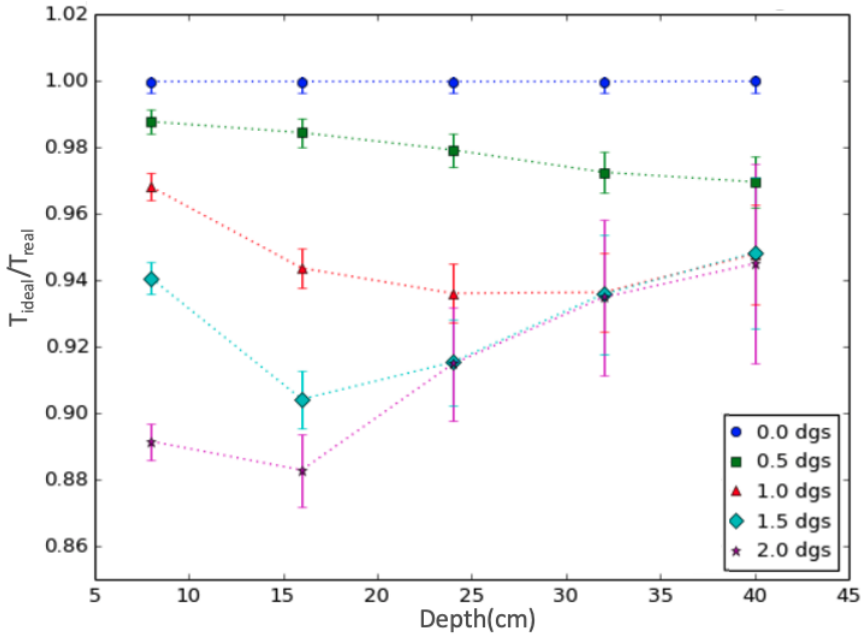

FIGURE 3.6: Distribution of the ratio T_{ideal}/T_{real} as a function of the collimator depth. The curves correspond to different choices of the beam divergence as quoted in the legend.

the systematic artefacts caused by the structure.

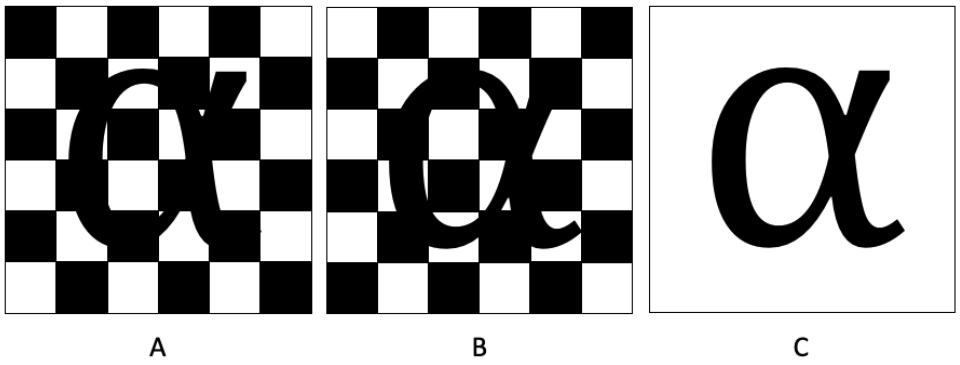

FIGURE 3.7: Schematic design of the resulting image combining two collimator positions on a fixed object. Images A and B emulate a neutron radiography with the CNC in two complementary positions, and C the result of combining the two former images.

Having the concept laid out in this chapter, the following will be dedicated to the first test application of the prototype of the ANET CNC. The test has been performed in Pavia, at the LENA facility, and will present the alignment procedure for the device, the movement strategy to eliminate the chessboard structure, and the beam divergence improvement with the CNC.

Chapter 4

The ANET CNC proof of concept

This chapter contains the results of a measurement campaign at the LENA reactor in Pavia (Italy) aimed at the first characterisation of the ANET compact neutron collimator [47]. The test was performed at the Pavia LENA reactor, a 250kW Mark-II TRIGA reactor where there is a thermal channel not optimised for neutron imaging. The poorly collimated flux served as a perfect test to prove whether the CNC could effectively deliver a highly collimated beam within a very confined space. To that end, the image resolution of the radiography generated by the collimated beam resulting from the ANET CNC will be compared to that of the primary uncollimated flux. To measure the image resolution, two standard objects have been used, a Siemens star and a bar pattern.

4.1 The experimental set-up

The experimental set-up used to perform the measurements is composed of 4 stages:

1. The source: The neutron energy spectrum created at the core of the MARK-II TRIGA reactor follows a Watt distribution[1], which is then thermalised via two filters, a sapphire and a bismuth one, surrounded by a high density polyethylene cylinder. The beam at the exit window is predominantly thermal in energy, with an angular dispersion of 2 degrees.

2. The collimator: The prototype of the ANET CNC used for the experiments has a channel section of 2.5 x 2.5mm^2, with a length of 400mm.

3. The sample: Different reference test objects.

4. The detector: A commercial LiF-ZnS(Cu) based neutron imaging instrument.

A schematic of the instrumental setup is depicted in figure 4.1. The prototype used is composed of a compound material with a 10-15% in mass of B_4C. Every channel is 2.5x2.5x400 mm, with a total field of view of 50x50mm^2. The geometrical characteristics of the collimator imply a nominal L/D=113 along the diagonal, with an axial L/D=160. This L/D factor translates into an acceptance angle, through equation 1.6, equivalent of 0.36 degrees for vertical and horizontal directions, and 0.41 for the combination of both.

[1] A typical fission spectrum.

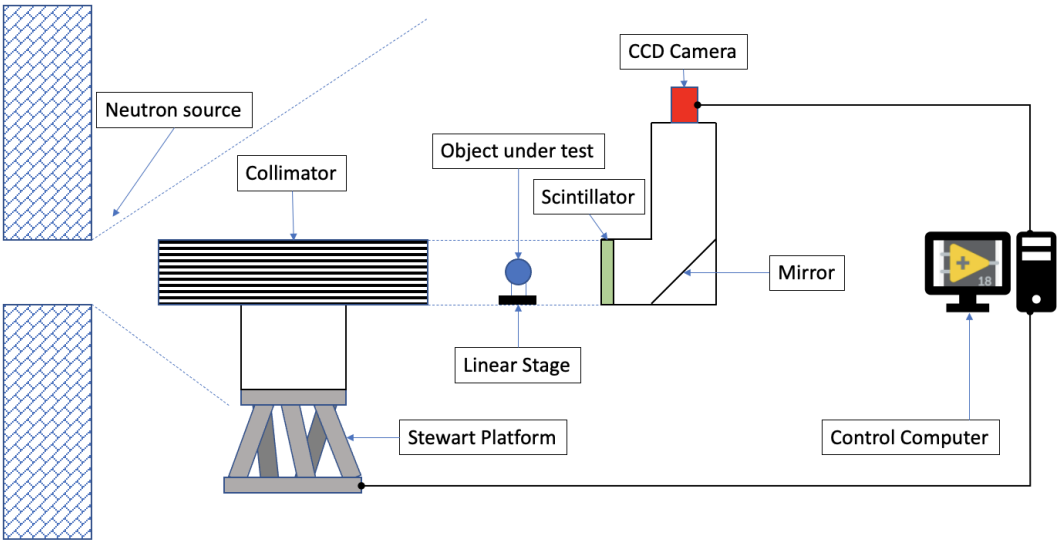

FIGURE 4.1: Design of the basic set-up used in ANET experiments.

The collimator, as explained in the previous chapter 3, requires a moving stage to deliver a valid image. To this end, it was mounted on a highly precise Stewart platform, capable of moving the instrument with 6 degrees of freedom with a precision better than $10\mu m$. In order to optimise the image quality whilst minimising the data processing required, a dynamic approach has been adopted. During the radiography, the collimator is moved continuously, along a scan-like pattern with a very fine separation between lines to minimise dishomogeneities and disturbances. Further details will be disclosed in following sections.
The imaging system is a commercial setup, composed by a 14-bit Sony CCD coupled to a $400\mu m$ scintillator screen made of ZnS(Cu) and ^{6}LiF at a mass rate 2:1. Any radiography has to be normalised to the open beam and combined with the subtraction of the dark field, as described in chapter 2 With the collimator, the open beam image is done by moving it through the same pattern without the object in front of it. While the dark field image is obtained by taking a radiography while turning off the source, or as in this case, closing off the beam shutter.

4.1.1 The CNC alignment procedure

With a collimation factor of 160 in such a short space, the alignment is crucial, as the divergence of the neutrons is below 0.36 degrees (or $6 \cdot 10^{-3} rad$). After a first coarse manual alignment with a laser, the Stewart Platform allows to perform the fine tuning of the angular tilt of the collimator, as seen in figure 4.2. This last active step in the procedure is done directly under the beam. The expected angular alignment precision is of the order of a few $mdeg$ and the translational positioning precision of the order of 100 μm. As the initial beam is conical, there was no possible way of uniformly illuminating all the channels of the collimator. Due to that, the best compromise was a centred and symmetrical distribution of the neutrons through all the channels.
The fine alignment procedure, as explained, can be performed within 10 minutes after finishing the manual set-up.

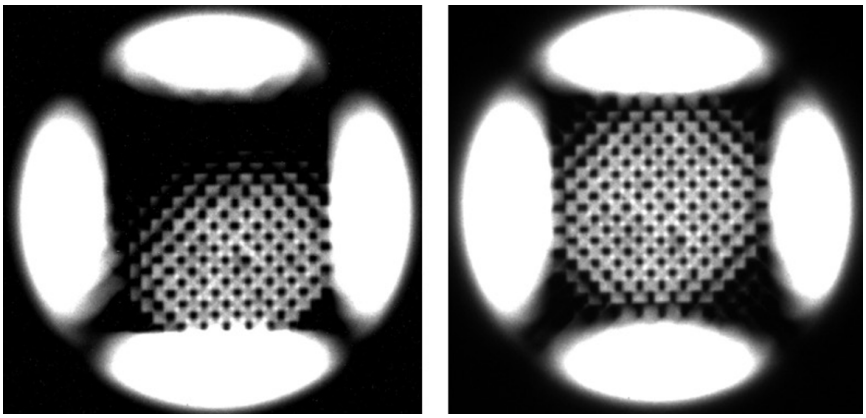

FIGURE 4.2: The image shows a radiography of the collimator before the alignment (left) and after (right). In both cases, the chessboard structure is clearly visible. After the alignment the illumination of the alternated channels is well uniform, suggesting the definition of an internal fiducial area.

Figure 4.2 represents a static radiography using the collimator. In the final radiographies, the chessboard structure characteristic of the ANET CNC should not be present. In order to achieve this result, a dynamic moving pattern strategy has been optimised and will be explained in the following section.

4.1.2 The dynamic acquisition procedure

One of the greatest challenges of this thesis work has been to figure out a way to eliminate the chessboard structure from the radiographies without requiring an immense amount of time and resources. The original idea of two spatially complementary images averaged could only be applied under ideal conditions. If the intensity profile after a channel was uniform and flat, the principle of the two images could have worked, but the actual intensity profile is closer to a 2D gaussian shape, implying that, to apply this method, the measure would require a very elevated number of images, each of which with the CNC at different spatial coordinates in order to uniformise as much as possible the averaged field. Based on this fact, the idea of a long exposure with a dynamic pattern was built.
During the radiography exposure time - in the experiments' case, $900s$ - the Stewart Platform moves the collimator along a 5 x 5 mm^2 square, equivalent to two air channels and two collimating rods. After an extensive study, the triangular alternated pattern has proven to be the most effective and performing (see figure 4.3). This takes into consideration some intrinsic features of the Stewart platform and minimises systematic effects. The pattern is defined by 2 parameters: the extension and ω. The extension is fixed to the double of the channel size, while ω is equivalent to the extension ($5mm$) divided by half of the number of divisions. In the measurements performed in Pavia, ω had a value of $4.76 \cdot 10^{-2} mm$, or $47.6\mu m$. This number has been set to be slightly smaller than the size of the projected CCD pixel on the scintillator, which is $47.9\mu m$. This way, any small disturbance or alteration induced to the image by the pattern remains unresolved and the overall result is a

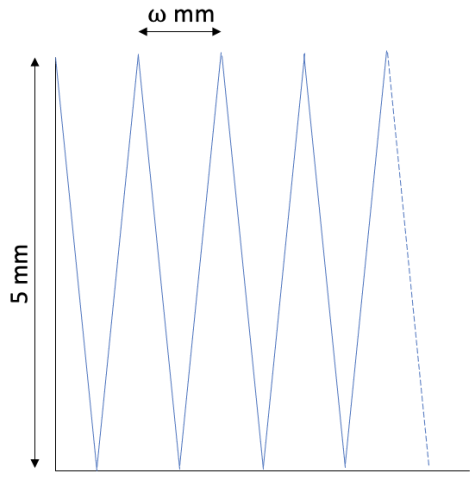

FIGURE 4.3: Schematics of the triangular pattern of the dynamic approach of the collimator method of operation.

smooth, pattern-less image. Figure 4.4 shows a proof of this concept: on the left the static image of the collimator is shown, while on the right a dynamic image of the collimator is displayed using the aforementioned pattern. As it can be appreciated, the chessboard pattern is not present anymore. What survives are some mild dark spots which were already present in the static images and correspond to anisotropies on the filters that compose the original beamline. Those were not possible to see without the collimator, as the bare beam has a strong scatter component which would hide those irregularities. The collimator selects only the neutrons with appropriate directions while absorbing the rest, rendering those effects visible. It can be understood as a base neutron radiography of the filters present to configure the beam.

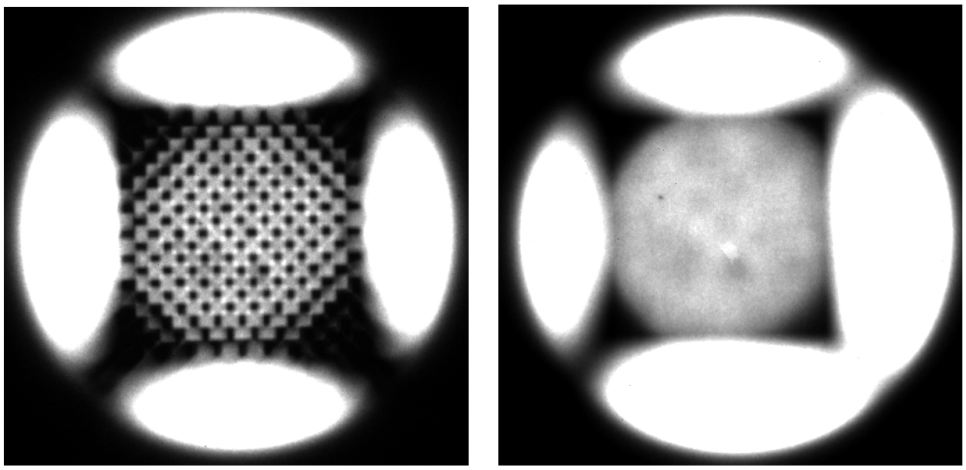

FIGURE 4.4: Comparison of radiographies done statically (left) and dynamically (right). For details see text.

The dynamic acquisition procedure, as specified before minimises some systematic effects: sudden changes of speed in one of the axis corresponding to the turning points introduce an uncertainty on the coordinates of the turning point itself. This is due to the internal clock of the control system. Having a

clock of $1kHz$, and an average velocity of $5\frac{mm}{s}$, at every tick the Stewart platform moves roughly $5\mu m$. This generates an error which may accumulate along the pattern and produce alterations on the image. In order to compensate for this, the control algorithm traces the time at which the collimator passes by each peak and valley, and compares it to the time at which it *should* have passed by. If there is a mismatch, the algorithm will adjust the speed in order to ensure that the platform will reach the following point at the correct timestamp. This adaptive velocity correction has proven to be sizeable improvement on the image quality at short exposure times when the speeds are higher.
The image quality with the ANET compact neutron collimator is clearly improved, in order to quantify by how much, two standard reference samples have been used: the PSI Siemens star and bar pattern. Those two instruments are able to determine the image resolution within ranges of 25-250μm and 50-1000μm respectively. This is described in the following section.

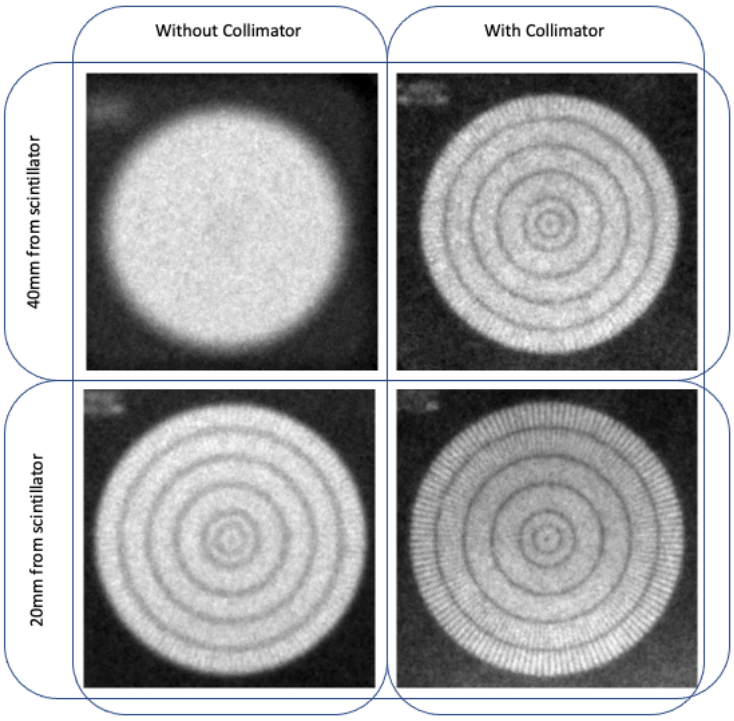

FIGURE 4.5: Table showing the normalised measurements of the Siemens star with and without the collimator at 40mm and 20mm from the scintillator respectively.

4.2 Results of the measuring campaign

To evaluate the system resolution, the experimental procedure consisted in placing the Siemens star at different distances from the detector, whilst keeping the collimator and the scintillator at a fixed 100mm from each other. The measurements have been performed with and without the ANET collimator in the beam, in order to compare the image resolution under both circumstances. One first example of the sheer increase in image resolution is shown in figure 4.5. Where the Siemens star radiography with and without

the ANET CNC is shown. In the left image, no details of the Siemens star are visible. A bar pattern measurement proved the spatial resolution to be around 750μm, far above the upper measuring limit of the Siemens star. In the second image, once the collimator was set, a resolution of roughly 225μm can be appreciated.
The comparison between the resolution measured with and without the ANET collimator present at various distances is shown in figure 4.6. The image

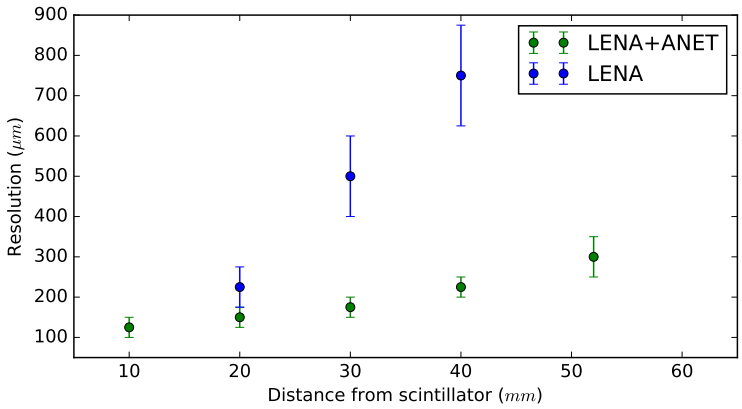

FIGURE 4.6: Comparison between the resolution obtained with and without the ANET collimator under the LENA Channel B beam.

resolution improvement due to the ANET collimator is mighty. It is a first indication that using the ANET technology a poorly collimated source can become suitable for neutron imaging applications.
It is interesting to demonstrate that the measurement trend can be explained from a simple geometrical model. As explained in chapter 1, the resolution is a convolution of the intrinsic limit resolution of the scintillator (σ_{det}) together with the optical penumbra (σ_{pen}), related through the equation:

$$\sigma_{total} = \sqrt{\sigma_{pen}^2 + \sigma_{det}^2} \tag{4.1}$$

The error associated to σ_{tot} is dominated by the physical dimension of the pixel projected on the scintillator screen, as the resolution's true value may vary within this range.
The agreement between the expected theoretical values and the measurement obtained with the ANET CNC are shown in figure 4.7. The agreement is remarkable, thus proving the validity of the measurements as well as the geometrical model employed.
The Pavia measuring campaign is a first demonstration of the ANET CNC capabilities to improve the image quality and resolution generated by an uncollimated beam. The results presented in this chapter have been peer reviewed and published [48].
These encouraging results have been the basis for further research as described in the following chapter 5, in which an in-depth study on the ANET CNC will be performed through two computational models. The results have also stimulated a follow-up measuring campaign at a large-scale facility such as the BOA beamline at the Paul Scherrer Institut. The choice of that facility

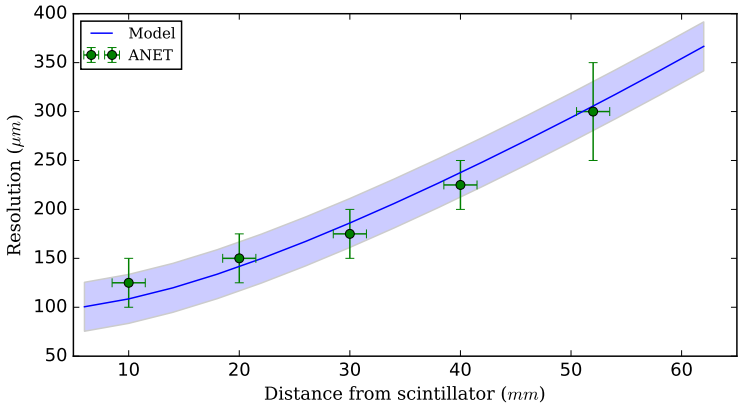

FIGURE 4.7: Comparison between the resolution obtained with the ANET collimator and that expected from the theoretical model.

adresses another goal of the ANET project, i.e. to demonstrate the CNC applicability on both reactor-based sources and accelerator-based sources and in different beam intensities and energies. That will be described in chapter 6.

Chapter 5

Simulation work

This chapter is dedicated to the extensive simulation work performed to assess the performance of the ANET compact neutron collimator. The study is divided in two big blocks: the NeDiMo simulation to achieve an in-depth characterisation of the geometrical behaviour of neutrons inside the collimator, and a McStas simulation, to evaluate the performance of the collimator under different sources.

5.1 The Neutron Divergence Model (NeDiMo)

The Neutron Divergence Model (NeDiMo) has been programmed as part of this thesis work and is now available as open source in GitHub[1] The scope of this software package is to have a way to easily study the geometrical behaviour of the neutrons with the ANET CNC, both in 2D and 3D, under different sources, with different prototype configurations, and under different set-ups.

5.1.1 The model

The algorithm simulates a parallel source of neutrons with arbitrary energy, generated at a given L/D factor. The neutron transport through the 2D collimator[2] and the interaction with the detector detector are fully simulated. Figure 5.1 is a representation of the simulated geometry.

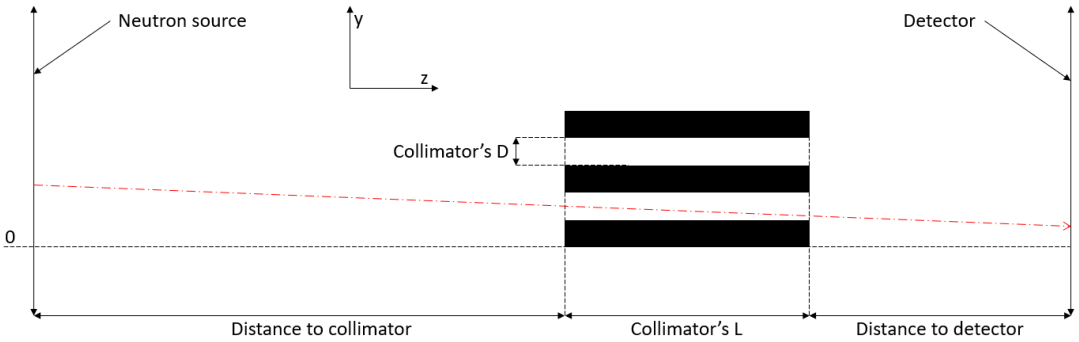

FIGURE 5.1: Geometry of the 2D model also including most of its variables.

[1] https://github.com/OriolSansPlanell/Thesis
[2] Similar to a Soller slit collimator in this case.

In order to study the geometrical alteration of the neutron beam due to the collimator, two assumptions have been used in the model:

1. The scattering of neutrons from air is negligible.
2. The absorbing elements that compose the collimator are treated as ideal neutron absorbers.

The two assumptions are close to reality: thermal neutrons, as those considered in the experiment, have a mean free path of over $10m$ in air, while the distances covered in the model are well below $2m$ overall. Under those circumstances, the scattering due to air can be considered negligible. On the other hand, as demonstrated in [47], the neutron flux on the exiting window of the collimator with respect to a perfect absorber is as close as 98%.
Within the model, every variable is manually tunable, from the size of the neutron source to the amount of channels within the collimator, to the distance between each component.
Under two assumptions, the model is vastly simplified when compared to a more general neutron transport problem. This has a positive impact on the execution time required to obtain reliable data.
In practice, the main function of NeDiMo uses as input the following variables:

1. The L/D factor of the neutron source.
2. The physical dimensions of the neutron source.
3. The collimator's physical dimensions.
4. The distance between the source and the collimator.
5. The distance between the collimator and the detector.

The coordinate system used for NeDiMo is shown in figure 5.2. For each single neutron, the model uses two sets of normalised polar coordinates:

1. Generation coordinates: (r, θ, ϕ)
2. Transport coordinates: $(r, \alpha_{zx}, \alpha_{zy})$

Those coordinate systems are related through the following transformations:

$$\phi = tan^{-1}\left(\frac{tan(\alpha_{zy})}{tan(\alpha_{zx})}\right)$$

$$\theta = tan^{-1}\sqrt{tan^2(\alpha_{zx}) + tan^2(\alpha_{zy})}$$

$$\alpha_{zx} = \begin{cases} tan^{-1}\left(\frac{tan(\theta)}{\sqrt{1+tan^2(\phi)}}\right) & \text{if } \frac{\pi}{2} < \phi < \frac{3\pi}{2} \\ -tan^{-1}\left(\frac{tan(\theta)}{\sqrt{1+tan^2(\phi)}}\right) & \text{otherwise} \end{cases}$$

$$\alpha_{zy} = \begin{cases} tan^{-1}\left(\frac{tan(\theta)tan(\phi)}{\sqrt{1+tan^2(\phi)}}\right) & \text{if } \frac{\pi}{2} < \phi < \frac{3\pi}{2} \\ -tan^{-1}\left(\frac{tan(\theta)tan(\phi)}{\sqrt{1+tan^2(\phi)}}\right) & \text{otherwise} \end{cases}$$

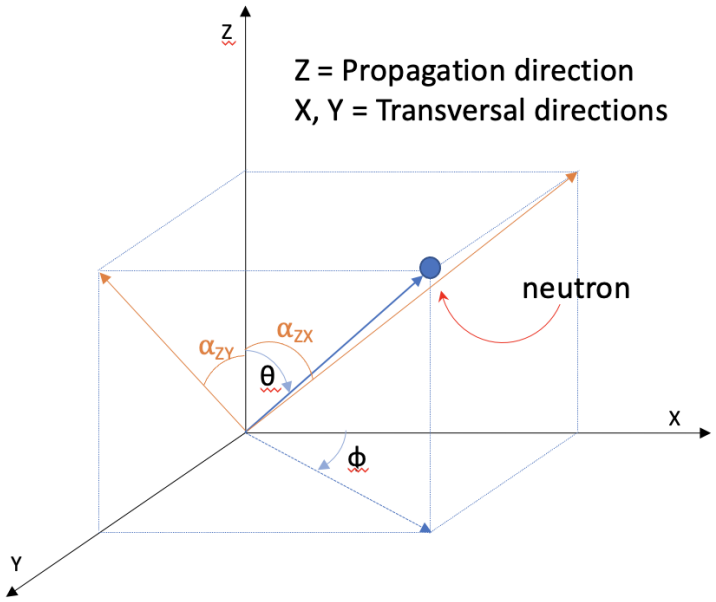

FIGURE 5.2: Coordinate system used for NeDiMo. The collimator's lower-left vertex is placed at the origin (0,0). The two coordinate systems used for transport are (x, y, z, θ, ϕ) and $(x, y, z, \alpha_{zx}, \alpha_{zy})$. Neutrons are generated uniformly with respect to $cos(\theta)$, then transported using the "cartesian" angles $(\alpha_{zx}, \alpha_{zy})$, and eventually registered on the initial coordinate system.

Source The model generates the neutrons on a plane with different spatial geometrical distributions to fit different possible scenarios. The current possible configurations are: uniform (evenly distributed probability on the plane), Gaussian (sampled in 2-D using the Box-Muller algorithm), or squared (using a super-Gaussian sampling function). Any new distribution can be inserted by creating a custom function and setting it as the geometrical generator.
Regarding the angular distribution for the neutrons, the particles are created uniformly with respect to ϕ on the range $[0, 2\pi]$, and uniform with respect to the cosine in θ on the range set by the divergence of the neutron source.

Collimation Once the neutron has been generated, and thus the initial position (x_0, y_0, z_s) and angles (θ, ϕ) are determined, the algorithm traces the geometrical line, and checks whether or not it impacts with the absorbing elements of the collimator. The collimator geometry is described through an impact function, which is tailored to the experiment. The most common in this case is the multi-channel chessboard geometry, described in [47]. If the neutron reaches the material of the collimator, it is eliminated; if it doesn't, then it is detected.

Detection The detector is considered as an ideal detector, with a 100% efficiency. The final position (x_1, y_1, z_d) of the neutron and the initial angles are written in a file, which will eventually be used to perform the analysis.

The physical sample As an experiment in neutron imaging needs a sample to be neutrographed, this model also includes this component. By substraction, the algorithm, once it has registered the neutrons at the detector, it calculates those which would have interacted with an analytically described sample, and removes them from the 2D-histogram. This allows for multiple samples to be studied with exactly the same data set, or under different geometrical conditions. Two samples that can be tested are the cadmium thin foil, for knife-edge analysis, and the Siemens Star, which is a common reference sample to measure the resolution of an imaging system [3].

Movement of the collimator The ultimate use of the ANET collimator requires a dynamic operation while the image is taken. This dynamic pattern can be simulated in two different ways, depending on the source:

1. Quasi-infinite source: From a single simulation, the sample is substracted iteratively applying on each iteration a different offset for the X,Y position of the collimator. After that, the sum of the individual iterations yields the result equivalent to the collimator being used dynamically. this approach can only be done when the source is quasi-infinite (a.k.a.: bigger than the collimator itself, at least). This way the movement calculation doesn't alter the initial source.

2. Discrete source: An array of simulations, each with an X,Y offset on the position of the collimator, while keeping the sample at the same position. This technique is more demanding in terms of computational power, but there is no other way to keep the source unaltered when it is an inhomogeneous one (smaller or compatible in size with the collimator's field of view).

Both these methods lead to a non-normalised measure of the sample which can then be analysed.

The algorithm The pseudocode of the algorithm is detailed in the following:

Algorithm 1: Neutron Divergence Model (NeDiMo) pseudocode

```
Result: Write here the result
initialization;
while i > total iterations do
    Generate neutron (x_0, y_0, z_s, θ, φ) ;
    Calculate impact with collimator;
    if impact = False then
        Register position on detector;
    else
        i + 1;
    end
end
Define object geometry;
for neutron in list do
    Calculate impact with geometry;
    if impact = True then
        Remove neutron from list;
    else
        next
    end
end
Generate 2D histogram;
```

5.1.2 The results

L/D calculation

The true L/D is obtained by geometrically calculating the absolute maximum divergence angle produced by a collimator. This calculation, though, doesn't properly reflect the reality, as it will be shown and demonstrated in this subsection. An alternative to the traditional consideration for the L/D factor calculation will also be presented.
Through a equation 1.6, it is possible to evaluate which is the maximum divergence angle that a neutron can have when passing through the collimator, knowing the L/D factor. Figure 5.3 represents the calculation of the minimum L/D factor on every point contained within the exit window of a single channel of the ANET CNC prototype. A collimator with square channels has to take into account the diagonal of the section rather than the side. This reflects in the nominal L/D factor. Rather than the initially expected 160 for the ANET CNC, the L/D factor is 113. This number, though, doesn't reflect the reality of the measurements.
From the data distribution in figure 5.3, the minimum value for the L/D is 113, but there are also higher values, up to a maximum of 226. To appropriately evaluate which one is the most realistic, the simulation algorithm records the divergence data. Simulating a homogeneous uncollimated source behind the collimator and integrating the output of the collimator over all channels it is possible to measure the L/D factor. The plots in figure 5.4 show a predominance of highly directional neutrons after passing through

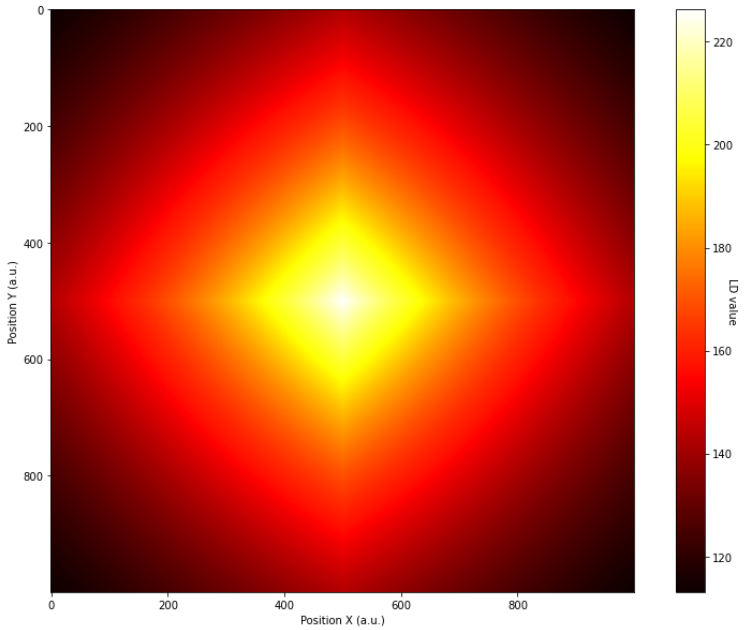

FIGURE 5.3: "Heat map" of the exit window of a single CNC channel showing the maximum possible L/D factor at each point in the plane.

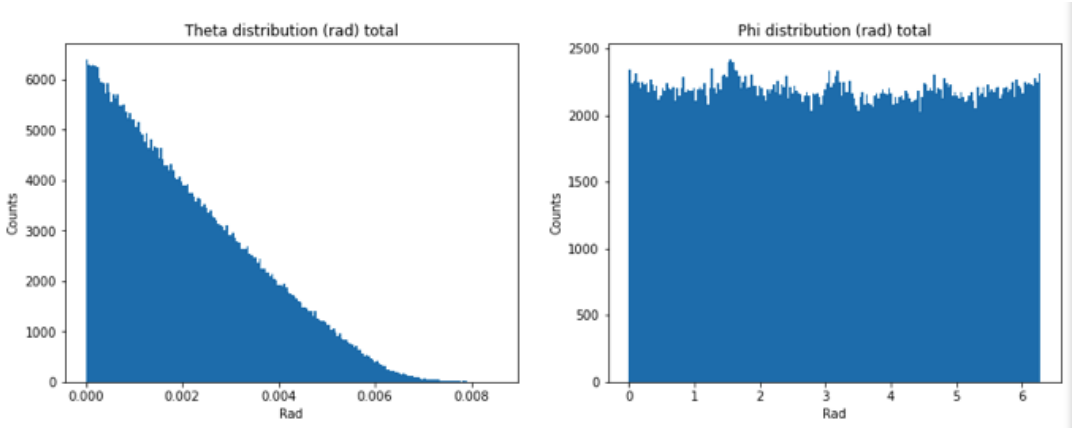

FIGURE 5.4: Distribution of θ (right) and ϕ (left).

the collimator. Despite the worst-case scenario expected by the geometrical L/D 113, the simulation returns a collimation of 163, taking the 99% most collimated part of the θ distribution. The average angular divergence after the collimation is 0.119 degrees, roughly equivalent to an average $L/D = 419$. This simulation proves that, despite the geometrical L/D, the probability, due to the squared section of the channel, of a neutron passing through the right angle to succeed at generating a count at such reduced L/D is very low. The effective measured L/D is then 163. This value is also compatible with the resolution measurements described in chapter 4.

Angular distribution

The algorithm stores, for each neutron at the detector, an array consisting of three position (x, y, z) and two angular (θ, ϕ) coordinates, so providing the

neutron distribution at a certain position of the detector.
In order to avoid unexpected distortions on the image it's important for the angular distribution of neutrons to be uniform. To that end, the simulation shows the angular data regarding the distribution of ϕ in polar form. Figure 5.5 is an example, extracted from the same simulation as the previous Section 5.1.2. The overall distribution is quasi-homogeneous, with a slight increase at the four channel sides. angular distribution is not uniform throughout

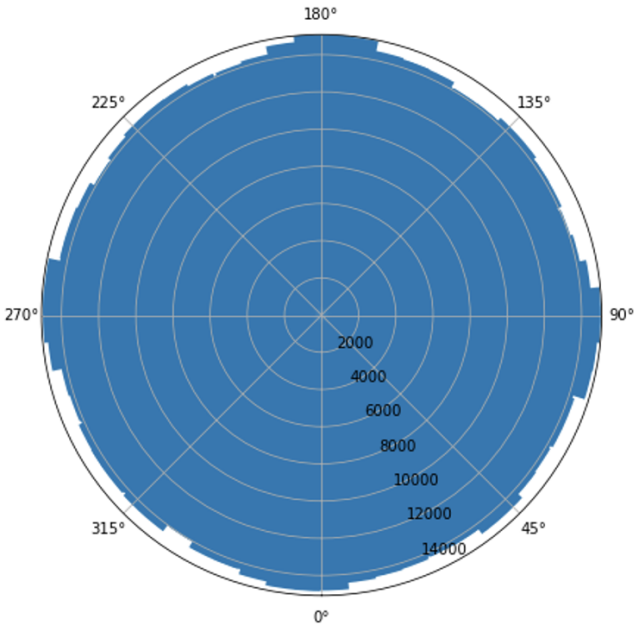

FIGURE 5.5: Distribution in ϕ of all the neutrons arriving at the detector after the collimator.

the collimator. As a matter of fact, it varies greatly from point to point. At the centre, the distribution is quasi-uniform, whilst at the vertexes the distribution holds an hourglass shape. Figure 5.6 highlights four cases of local neutron distribution: one from a vertex (a), one from the centre-top (b), one from the centre of the channel (c) and another one from a centre-left (d).
When the collimator will be moving, the contribution from each point will sum up, resulting in a uniform distribution at any point in space.

Simulating the Siemens star on a dynamic pattern

The most appropriate - and less resource consuming - way to simulate the movement of the collimator is to create a 50 x 50 grid and run a simulation with the collimator placed at each individual position of this grid. Afterwards, the low-statistics runs are summed, delivering a high-statistics result. In order to simulate the Siemens star, the following analytical representation has been used:

$$floor\left(arctan\left(\frac{y-y_c}{x-x_c}\right)\cdot\frac{S_s}{\pi}\right) \tag{5.1}$$

Where x and y are the spatial coordinates in the sample plane, x_c and y_c the coordinates of the Siemens star centre and S_s the number of spikes of the Siemens star. The coordinates (x, y) are evaluated at a certain z between the

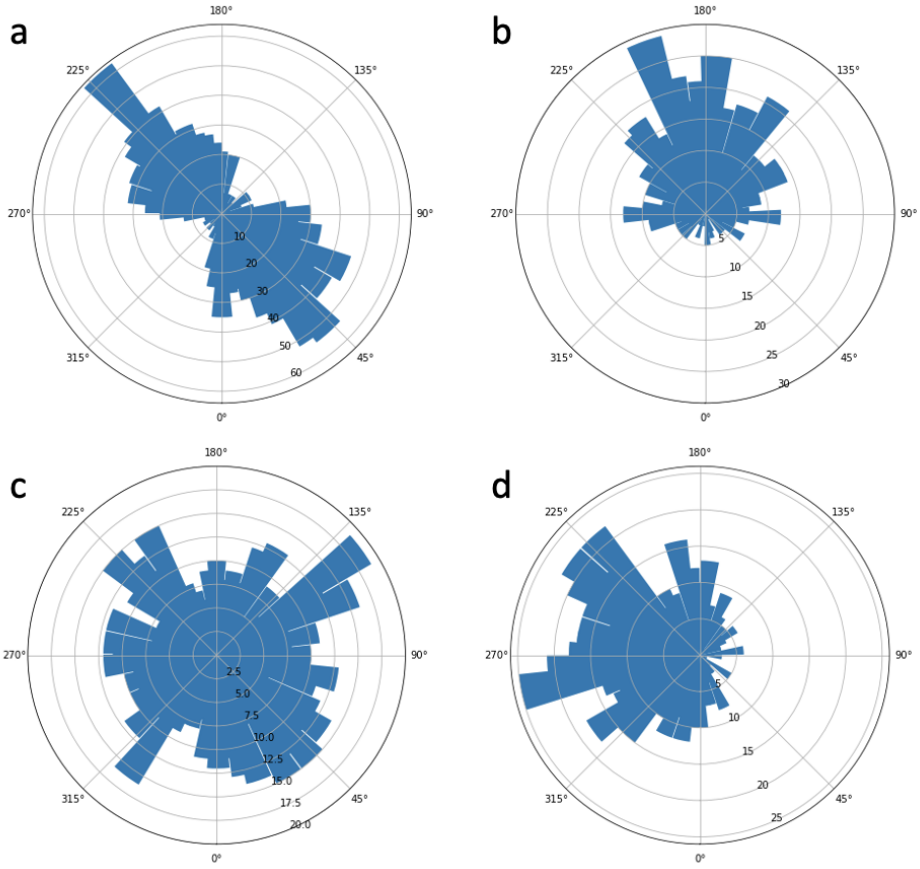

FIGURE 5.6: Polar plots of simulated angular distributions. The difference between the four plots is related with the position of the monitor w.r.t the square collimator channel: (a) top-left vertex, (b) centre-top, (c) centre and (d) centre-left.

collimator and the detector. If the coordinates (x, y) are within the radius of the Siemens star, and the value from equation 5.1 is even, then the neutron is absorbed (eliminated). This exclusion criteria generates the same effect as a 2D Siemens star placed at a certain Z plane within the distance from the collimator to the detector. From that model, the Siemens star can be simulated as positioned in front of the collimator in order to validate the resolution. As shown in figure 5.7, the resolution appreciated from the Siemens star decreases with the distance from the detector, as expected from the theoretical models already shown in chapter 1 and measured in chapter 4.
Through the worked performed on the NeDiMo code it has been possible to further learn regarding the behaviour of neutrons within the collimator, as well as the challenges posed by the geometry of the ANET CNC and the ways to overcome them. NeDiMo has been almost exclusively been programmed using the Jupyter interface and the SWAN framework [49] provided by CERN, as well as CONDOR [50], the cluster service for HPC[3]. The number of simulations performed to obtain the results shown in this chapter is approximately 600. With the number increasing to roughly 5k for the overall study, with up to 1k hours of computing time.

[3]High Performance Computing

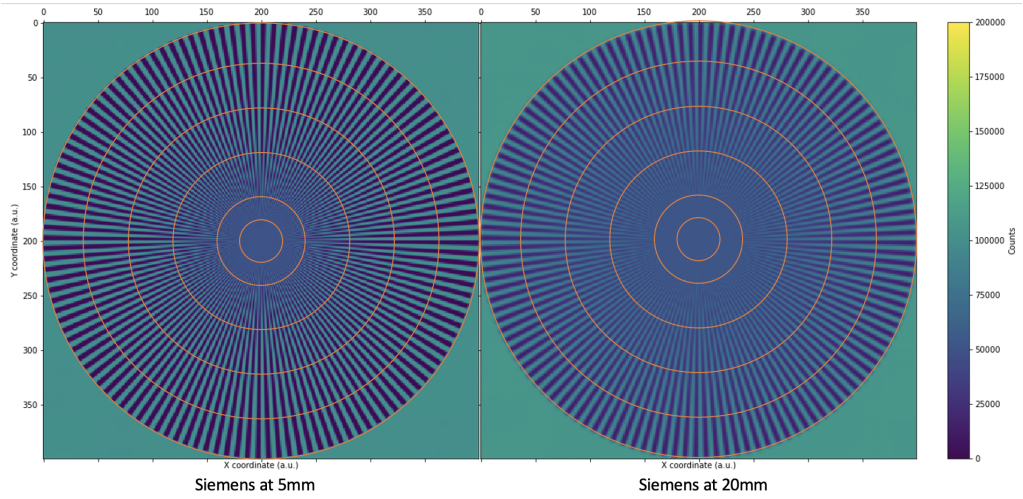

FIGURE 5.7: Two examples of Siemens star simulated under the measuring conditions of the LENA facility. The distance between the Siemens star and the detector is 10 *mm* (left) and 30 *mm* (right).

5.2 The McStas simulation tool

McStas [51–55] is a general-purpose toolbox for Monte Carlo simulation of neutron instruments. It is a highly efficient code which allows for instrument design and scripting using C language, with the results being analysed in Python. The purpose of using McStas for the simulation of the system and the measurements performed at BOA has been to have an understanding of the theoretical performance of the ANET CNC using a standard tool. As a matter of fact, the BOA beamline was already simulated in detail in McStas in an open input file [56], therefore the work required was the inclusion of the ANET CNC in the simulation. Figure 5.8 shows the simulated volumes of the model, as delivered by the McStas software package in trace mode.

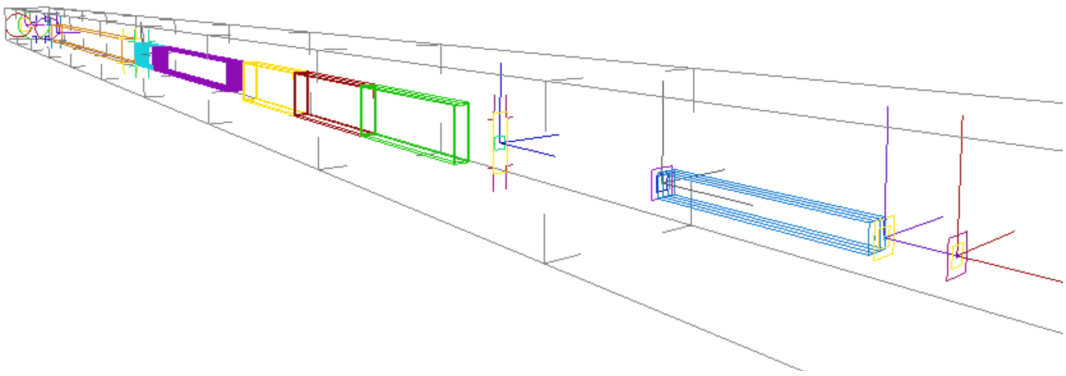

FIGURE 5.8: Rendering of the McStas model of BOA, including the custom ANET CNC section and monitors. The light blue element at the lower right belongs to the ANET CNC; while the objects on the left represent the guides and bender, as well as the source of BOA.

5.2.1 The model

The inclusion of the ANET CNC within McStas has followed a similar approach as the one taken for the NeDiMo code. In order to evaluate whether a neutron will be absorbed or not, the following variables are introduced: fx_0, fy_0, fx_1 and fy_1, defined as[4]:

$$fa_n = floor(\frac{a - width/2}{width}) \tag{5.2}$$

Where a stands for x or y, and n can be 0 or 1, depending if the neutron is measured at the entry or exit window, and $width$ is the width of the single ANET collimator channel. Three conditions are defined:

1. The neutron at the entry and exit windows must be within (x_{min}, x_{max}) and within (y_{min}, y_{max}).
2. $fx_0 = fx_1$ and $fy_0 = fy_1$.
3. fx_0 and fy_0 must be either both even or both odd.

If any of the three conditions isn't met, the neutron will be absorbed, otherwise, it will be transmitted.
This simple model allows for the simulation of any kind of configuration for the ANET collimator, regardless of total length, size or number of channels.

5.2.2 The simulation study

The first study had the purpose of understanding the divergence at the exit window of BOA. The initial neutron beam is transported through a bender on the horizontal plane, and it creates bands of divergence which can be appreciated by separating the divergence components in horizontal and vertical. Figure 5.9 shows the maximum divergence at each point in space at a plane placed at $3mm$ from the exit window. There are 3 effects which are important to consider from this simulation:

1. On the horizontal plane, the bender produces the "divergence bands" due to the effect of different neutron scattering angles on the guide.
2. On the vertical plane, there is a central horizontal band of highly divergent neutrons. This effect is caused by the optical guide bouncing neutrons on the walls and focusing them on the middle section of the beam.
3. Also on the vertical plane, the neutrons with the smallest divergence are found at the centre of the beam, as it would be expected from a common long-tube collimator.

The overall divergence of the initial beam is around 4 degrees. The combination of both vertical and horizontal divergences is shown in figure 5.10.

[4] $floor$ is a standard computational function which takes as input a real number x and returns de greatest integer less than or equal to x.

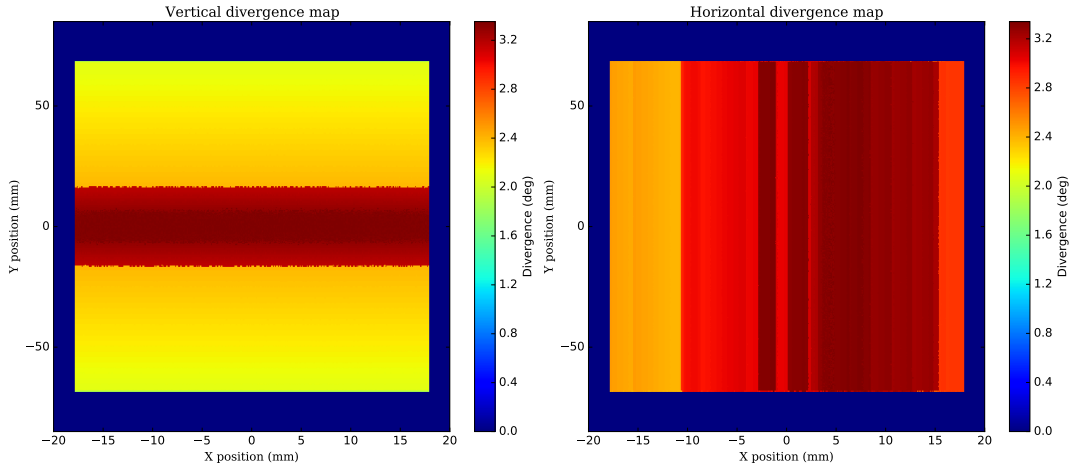

FIGURE 5.9: McStas simulation of the BOA facility. Heat maps of the divergence at the exit window of BOA. Left: Vertical divergence map, Right: Horizontal divergence map.

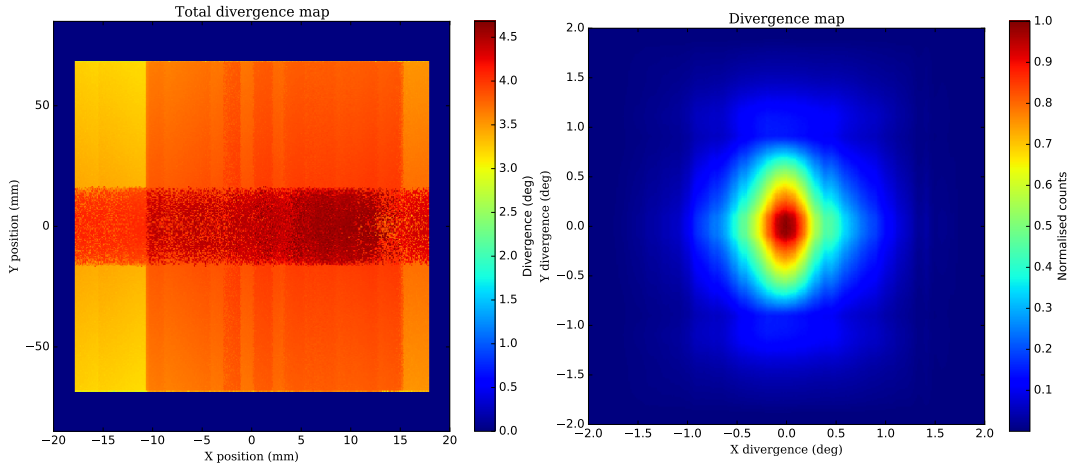

FIGURE 5.10: Left: Heat map of the total divergence at the exit window of BOA. Right: 2D histogram of the axial-wise divergence at the exit window of BOA.

As the real measurement position of the collimator in the beam is at 5.23m from the BOA exit window, the simulation has been used to study the beam divergence distribution at this coordinate. At that distance, there is a strong pinhole effect through which the neutrons become highly collimated. In this case, the total divergence of the neutrons at that distance is close to 0.5 degrees, with 0.44 degrees being caused by the vertical component of the divergence and 0.24 by the horizontal component. The total divergence is calculated as the square root of the sum of squares of the vertical and horizontal divergences. These results are shown in figure 5.11. There is a uniformisation of the divergence of the beam with the increased distance. From the simulated results, the image spatial resolution can not be expected to be uniform regardless of the direction, as there is a strong difference between the horizontal and vertical components of the divergence. From the simulation alone, the equivalent L/D of the BOA beamline at this distance is 130 for the

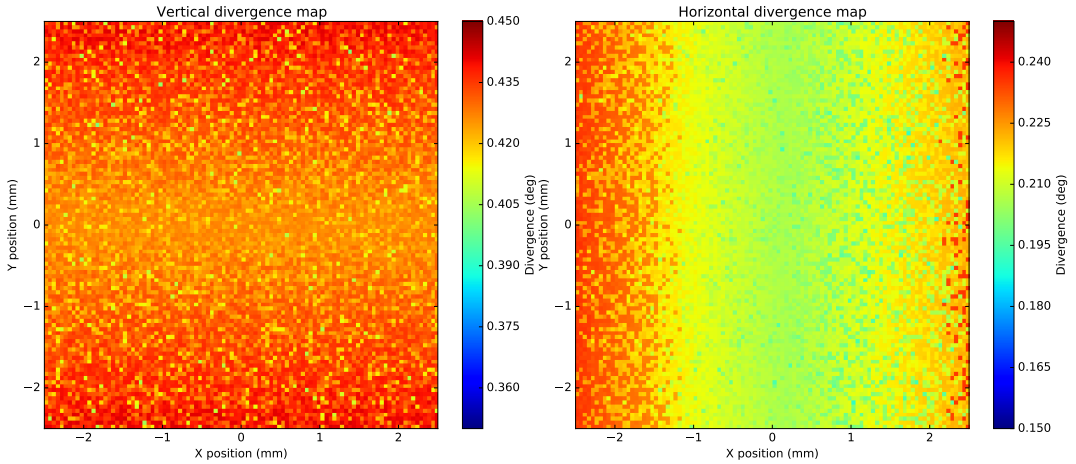

FIGURE 5.11: Heat map of the divergence at 5.23m from the exit window of BOA. Left: Vertical divergence map, Right: Horizontal divergence map.

vertical axis and 242 for the horizontal axis. Given those numbers, the expectation is to measure a small improve in resolution on the vertical axis when including the ANET CNC in the setup, while there should be no improvement whatsoever on the horizontal axis.

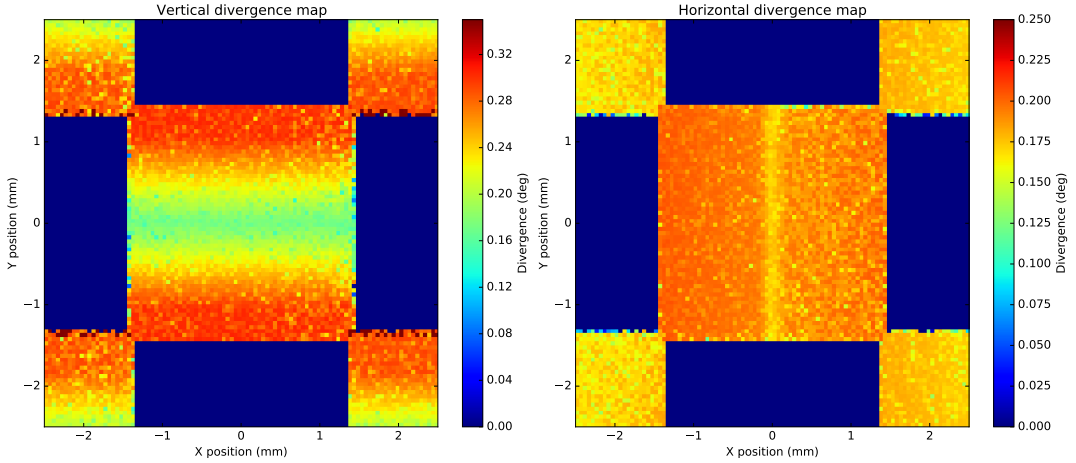

FIGURE 5.12: Heat map of the divergence at 5.23m from the exit window of BOA and right after the ANET CNC. Left: Vertical divergence map, Right: Horizontal divergence map.

Next, the ANET compact neutron collimator is included in the simulation following the model described in section 5.2.1. The following characteristics of the prototype have been assumed: 400mm in length, with a field of view of 50 x 50 mm^2 and a channel section of 2.5mm.
To study in detail the divergence and beam alteration caused by the collimator, the simulation focuses on a single central channel in order to understand the difference between the horizontal and vertical divergences. These results are shown in figure 5.12. From the figure, the main contribution to the total divergence is the vertical component, as the divergence has a maximum of 0.357 degrees, equivalent to an L/D of 161. The reduction close to 0.36 is what

is geometrically expected given the characteristics of the ANET CNC. The divergence distribution is also equivalent to that calculated from the model in figure 5.3, given the contribution of the vertical axis only. This is an indication of the collimator actively limiting the neutrons passing through, as those which are successfully measured on the other side follow the collimator's limit distribution. On the other hand, the divergence distribution on the horizontal axis barely changes, although it is still reduced from 0.236 down to 0.206. This would, numerically, imply an improvement from an effective L/D of 242 without collimator to 278 once the collimator is included. The problem at this level of resolution improvement is that the variation from the resolution curve would be within the instrumental uncertainty, and thus would not be measurable, while the improvement on the vertical resolution being from an L/D of 130 up to 160 would be easier to measure, despite the absolute variation being the same.

5.2.3 Systematic effects of a possible mis-alignment of the ANET CNC

The alignment procedure is critical when installing the set-up of the experiment involving the ANET compact neutron collimator. For this reason, a tilting parameter has been included on the ANET component of the simulation, allowing for the collimator to be rotated along the vertical axis without altering the rest of the beamline.

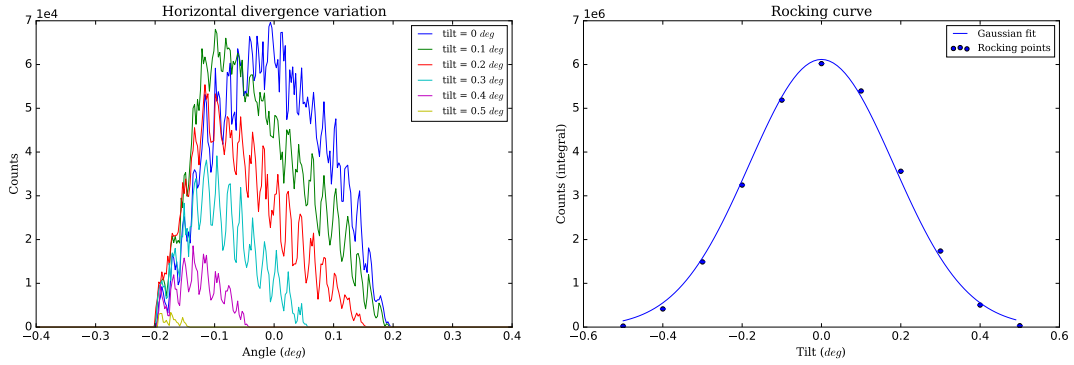

FIGURE 5.13: Plot highlighting the variation in angular distribution when varying the tilt angle of the collimator (left), and rocking curve (right).

Figure 5.13 shows the effect on the angular spectrum when varying the Y angle of alignment of the collimator. The intensity is reduced and the whole distribution tends towards one side - the effect is symmetrical when tilting towards the other side -. The limit angle on each distribution is found by subtracting the CNC acceptance angle to the tilt angle of the structure. Integrating every distribution brings about the rocking curve, which demonstrates the importance of proper alignment of the instrument, as a bare deviation of 0.1 degrees reduces the integral intensity by more than 10% and creates severe asymmetries on the neutron angular spectrum.
With the simulation work performed, the characteristics of the ANET CNC are well defined. The following chapter will be dedicated to an experimental measuring campaign, in which the performance of the ANET CNC will be

studied. The campaign was done at the Paul Scherrer Institute, in Switzerland, and the beamline was BOA.

Chapter 6

Performance Measurement of the ANET CNC

The inital objective of the PSI campaign was the determination of the effective L/D delivered when including the ANET CNC in the BOA beamline. The expected result was that the best collimation should dominate. The BOA beamline has a pin-hole system of 40x80mm^2, which increases the collimation power with increasing distance. The ANET CNC would dominate when placed closer to the exit window, while the L/D value would increase on longer distances due to the better collimation of the pin-hole. Being a complex system, several measurements were required using a standard reference object to extract the value of the resolution and a numerical procedure to combine the results and calculate the beam divergence.

6.1 The L/D factor extraction

The mathematical process to calculate the effective L/D from the measurements is an evolution of the model explained in Chapter 4, detailed in [3].
The measured resolution is the result of a combination of two effects: the detectors resolution limit σ_{det} and the penumbra blurring σ_{pen}. Those two values are combined as follows: $\sigma_{res} = \sqrt{\sigma_{pen}^2 + \sigma_{det}^2}$.
For this development, the following variable is defined: $C = D/L$. The penumbra blurring in this model is defined as $\sigma_{pen} = lC$ This definition is a good approximation when using with a small, close to the detector, tube channel as well as a far pinhole. Considering this relation, the following equation stands:

$$\sigma_{res}(l)^2 = \sigma_{det}^2 + (lC)^2 \tag{6.1}$$

Performing a series of measurements, the following system of linear equations is defined:

$$\begin{aligned} \sigma_{det}^2 + (l_1 C)^2 &= \sigma_1^2 \\ \sigma_{det}^2 + (l_2 C)^2 &= \sigma_2^2 \\ &\vdots \\ \sigma_{det}^2 + (l_n C)^2 &= \sigma_n^2 \end{aligned}$$

Where $i = 1, ...n$ identifies the measurement number. The notation of σ_{res} is simplified in each measurement as $\sigma_{1...n}$. The system of equations can be written in matrix form as:

$$\begin{pmatrix} 1 & l_1 \\ 1 & l_2 \\ \vdots & \vdots \\ 1 & l_n \end{pmatrix} \begin{pmatrix} \sigma_{det}^2 \\ C^2 \end{pmatrix} = \begin{pmatrix} \sigma_1^2 \\ \sigma_2^2 \\ \vdots \\ \sigma_n^2 \end{pmatrix} \tag{6.2}$$

The least squared solution of this system is: $\theta = (H^T H)^{-1} H^T x$. This estimate generates an approximately straight line, proportional to the L/D factor, with an asymptotic minimum towards the value of σ_{det}. To improve the precision of the calculation on the lower distances, a weighting function is applied to force the system to focus on those points, rather than the long-distance ones. The weight matrix takes the form:

$$W = \begin{pmatrix} \frac{1}{l_1} & 0 & \cdots & 0 \\ 0 & \frac{1}{l_2} & \cdots & 0 \\ \vdots & \vdots & \ddots & \vdots \\ 0 & 0 & \cdots & \frac{1}{l_n} \end{pmatrix} \tag{6.3}$$

Modifying the result of the estimate to:

$$\theta = (H^T W H)^{-1} H^T W x \tag{6.4}$$

From this equation, the results of θ are separated as: $\theta_1 = \sigma_{det}^2$ and $\theta_2 = C^2$ which, considering the definition change at the beginning of this calculation, can be expressed as:

$$\theta_2 = C^2 = (L/D)^{-2} \tag{6.5}$$

In order to apply this methodology, several measurements of image resolution are needed at different l distances, in order to improve the precision on the calculation of the fit for the L/D value.

6.2 The set-up description

The experiment has been performed at the Paul Scherrer Institut, at the BOA facility [57]. It is a multi-purpose beamline composed by a $18m$ long tube with a cold neutron flux of $10^8 cm^{-2} s^{-1} mA^{-1}$ at the exit window. As presented in chapter 5, the beamline is composed by a series of neutrons guides and a bender, which creates some alterations on the beam divergence. The beam exit window can also be restricted, through a pinhole, to different sizes, up to 40x150mm^2. For the measurements, the beam was restricted to a rectangular shape of 40 x 80 mm^2.
The setup made use of three towers - labeled as T4, T5 and T6 -. Each one uses a Z-axis moving stage parallel to the beam: the first one (T4) held the Stewart Platform and the collimator, the second one (T5) held a secondary X-axis linear stage with the samples, and the third one (T6) held the detector. The three T stages were configured so that the distance between the exit

window of the collimator and the scintillator of the detector was 190mm. The two standard reference samples were chosen to be a gadolinium knife edge and a Siemens star, both manufactured at the PSI, mounted in the middle stage (T5). The stage moved the samples at 8 different positions, from 10mm up to 80mm from the scintillator at 10mm steps. The T5 X-axis motor served to change from one sample to the other. Table 6.1 describes the position of

Position	T4	T5	T6
1	4480	4920	5360
2	5480	5920	6360
3	6480	6920	7360
4	7480	7920	8360

TABLE 6.1: Distance from the primary pin-hole to each motor (in mm) at each macro-position (1-4) for the measurements at BOA.

each stage, from T4 to T6 at each macro-position with respect to the primary pin-hole.
The camera used to acquire the images was an ANDOR 16-bit cooled CCD with a field of view of 4.00 x 4.00 cm^2 over a resolution of 1024 x 1024, leading to a projected pixel size at the scintillator of 33.65μm. The BOA system was controlled through the software package NIKOS [58], which is a custom distribution of the open source EPICS [59], while the Stewart platform was controlled via LAN using Labview.

6.3 The gadolinium knife edge technique

The spatial resolution measurements have been firstly evaluated with the gadolinium knife-edge technique. A reference sample, developed at the Paul Scherrer Institute [3], composed by a 100μm gadolinium sheet with two polished edges and mounted in an aluminium frame was used. With a fixed field of view, this sample provides a good estimate of the spatial resolution by means of the modulation transfer function ([60] and Chapter 2).
The measurements, as explained in the previous section, have been performed in 4 macro-positions, varying the distance of the whole set-up from the source exit window, and in 8 micro-positions at each turn.
The gadolinium knife edge sample has been placed as flat as possible, without tilt, in order to properly measure the vertical and horizontal spatial resolutions without interference from one to the other. Figure 6.1 shows the variation in image blurring from two measurements performed in position 1 (see table 6.1) with the collimator, and at respective distances from the detector of 70mm (top) and 10mm (bottom).

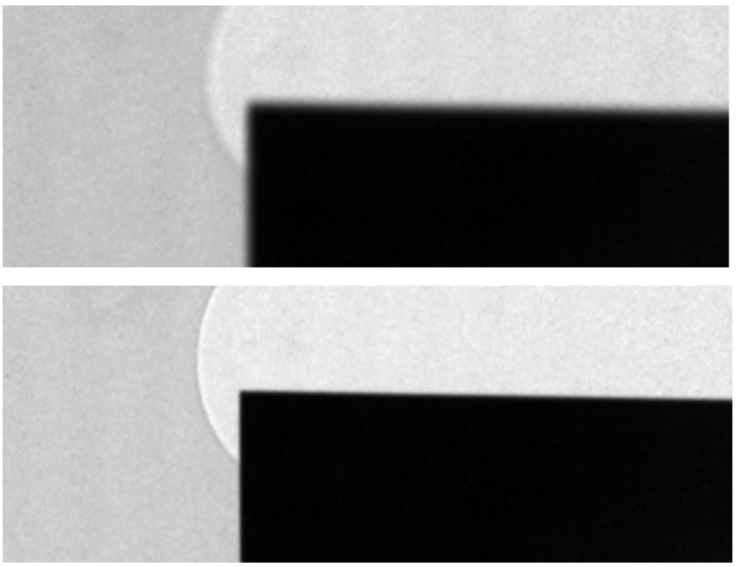

FIGURE 6.1: Two radiographies taken at macro-position 1 with the ANET collimator in, at 70mm (top) and 10mm (bottom) from the detector.

For each distance, two images have been taken, and the Modulation Transfer Function (MTF) has been calculated. Figure 6.2 is a good sample of a

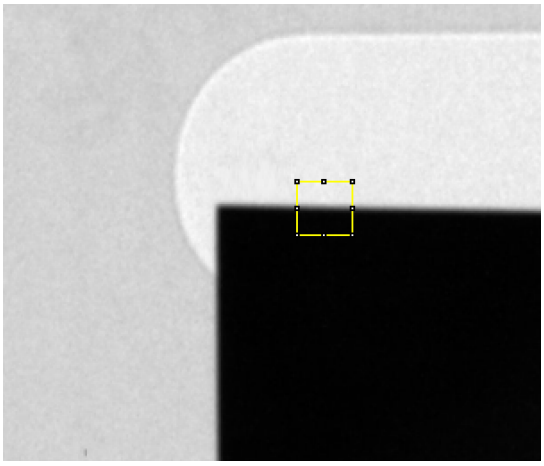

FIGURE 6.2: Image chosen as an example for the MTF demonstration. Image taken at the macro-position 1, with the ANET CNC in the beamline, with the sample at 50mm from the detector.

knife-edge analysis, since it has a very well-defined contrast area by means of a gadolinium sheet which completely eliminates the neutrons coming to the scintillator onto a certain area, creating a high-contrast edge from which to analyse the MTF.
In order to obtain the MTF, first the ESF is normalised through equation 2.28. The first derivative of the normalised ESF[1], calculated with equation 2.29, is the LSF, which is then fitted using a Gaussian curve. The result of the fit is shown in figure 6.3. The Fourier transform of the LSF curve is the OTF, as

[1]As a reminder: OTF: Optical Transfer Function; ESF: Edge Spread Function; LSF: Line Spread Function; MTF: Modulation Transfer Function

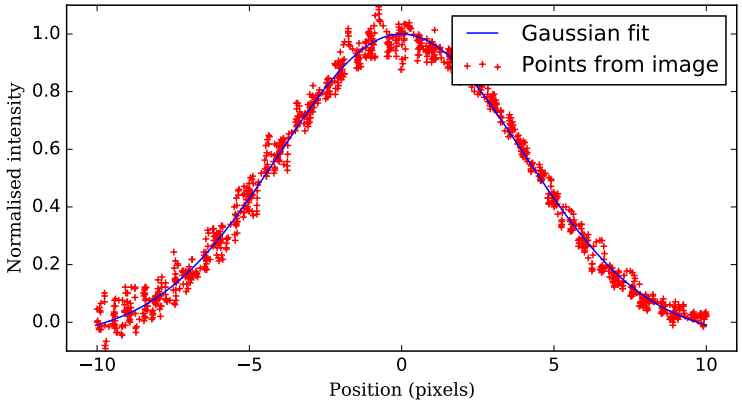

FIGURE 6.3: The LSF curve together with the gaussian fit.

described previously, the magnitude of which is the MTF, that can be fit with a polynomial of grade 6.

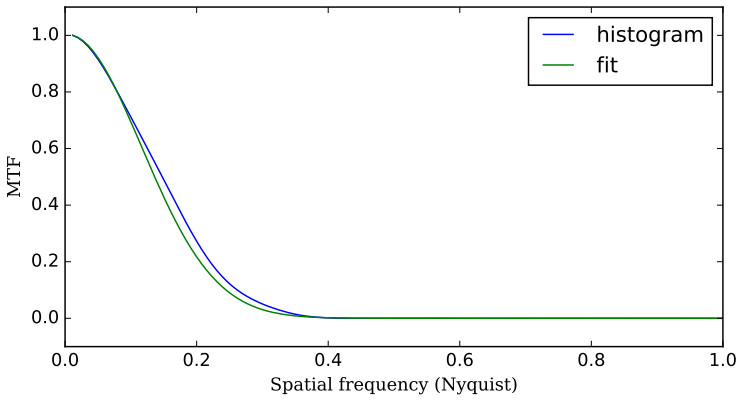

FIGURE 6.4: The MTF curve with the polynomial fit of grade 6.

As described in section 2.2, there is not a universal standard criteria for the threshold value on the MTF. In order to determine the limit resolution, the following procedure will be applied. One first measurement performed with the Siemens star attached to the scintillator delivered a precise measurement for the apparent pixel size[2] of 33.65μm. Through the L/D calculation procedure detailed at the beginning of this chapter, other than the effective divergence of the system, there is also a detail of the contribution of the detector. The procedure to evaluate the appropriate threshold has been the following:

1. Set a MTF threshold value.
2. Calculate the MTF for each of the 224 cases (2 axis, 8 micro-positions, 4 macro-positions and 2 repetitions of each) with that threshold.
3. Derive the 14 values for the L/D and detector contribution.
4. Repeat.

The iterative procedure has been performed for each threshold from 0.05 up to 0.25, leading to the graph in figure 6.5:

[2]Apparent pixel size includes all the different contributions of the detection system.

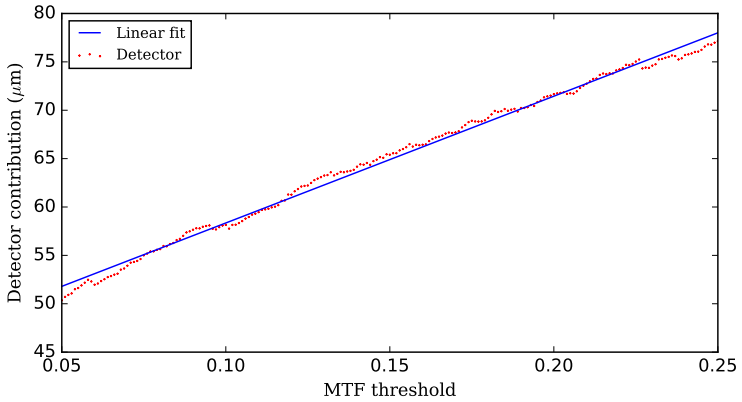

FIGURE 6.5: Detector contribution to the spatial resolution measurement as a function of the MTF threshold.

The actual contribution of the detector to the spatial resolution is twice the pixel size, and thus the correct MTF threshold value will be that which leads to a detector contribution of 67.2 μm. This value is found at a threshold of 0.155.
In figure 6.4, applying the 0.155 threshold on the MTF returns a value of spatial frequency of 0.27. This number translates to a spatial resolution of 124.4 μm, calculated using the same procedure as in 2.24. The result of this calculation for both images at the same position is averaged to obtain the final resolution. The MTF procedure is then repeated on each micro-position and the results included in the calculation of the L/D factor. For each macro-position two graphs (one per axis) as in figure 6.6 is generated.

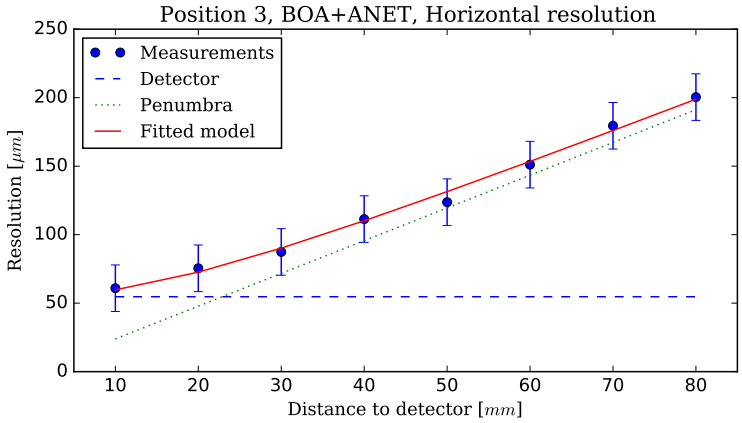

FIGURE 6.6: Sample of the L/D calculation from the measurements with collimator in position 3.

This graphic shows the determination of the L/D factor using the fitting model described in section 6.1. The model also separates the contribution due to the detector (dashed horizontal line) and the blurring (dotted slope), the combination of them results in the fitting of the measures.
Through this method, two L/D values are extracted on each macro-position, one for the vertical and one for the horizontal axis. In figure 6.7 the comparison between the resolution measured at BOA with and without the ANET CNC is shown. The plot shows the fit of the resolution measurements in

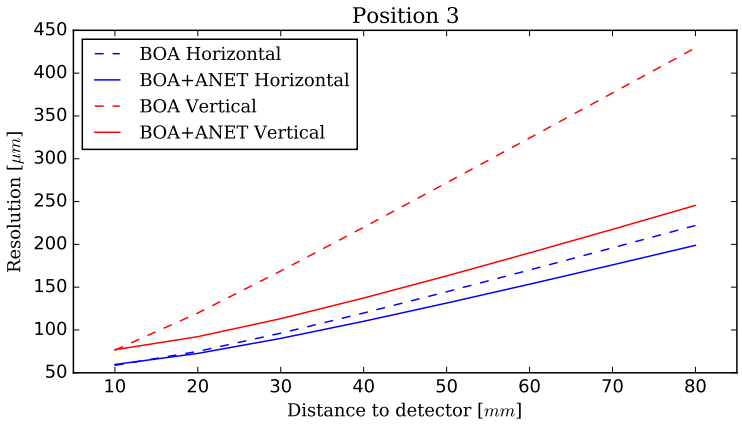

FIGURE 6.7: Resolution fit on macro-position 3, in both the BOA and BOA+ANET configurations, for the horizontal and vertical axis.

macro-position 3. The image shows a small improvement on the resolution on the horizontal axis, and a very big difference on the vertical one. The slope on the fitting curves is directly related to the L/D factor. This value can be converted to angular divergence through the formula:

$$\theta_{div} = arctan\left(\frac{L}{D}\right)^{-1} \tag{6.6}$$

The same analysis shown for macro-position 3 are repeated for all 4 macro-positions, and the results are shown in Figure 6.8. These first results are very important, as a lot of information can be deduced from them. There are two straight observations: the ANET CNC improves the divergence angle in all scenarios and the performance is better than expected by the geometrical structure of the collimator alone.

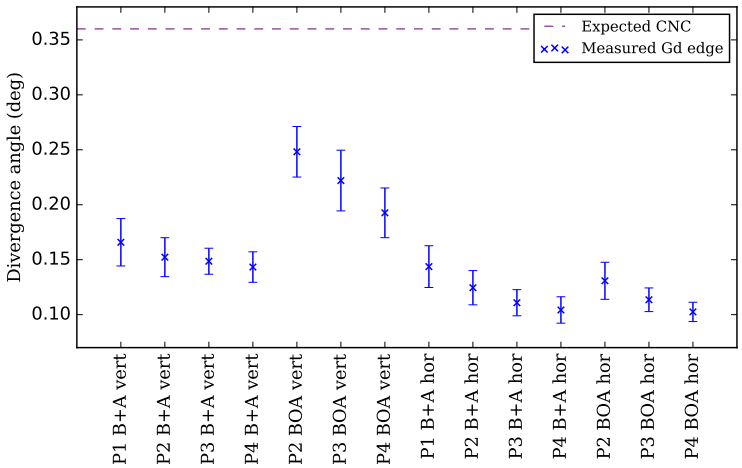

FIGURE 6.8: Calculated divergence angle on every configuration using the gadolinium knife-edge method. B+A stands for "BOA + ANET", while P1-4 correspond to the macro-positions 1 to 4 as detailed in the previous section in table 6.1. The errors have been evaluated using a Monte Carlo procedure and the ABC algorithm.

Following the literature, the beam divergence won't be affected by a collimator whose collimation power is smaller than the beam divergence itself. The measurements shown in figure 6.8 point at different conclusions. Not only the divergence is improved when the ANET CNC is included within the beamline, but it greatly reduces the beam angular divergence beyond its expected capabilities. A hypothesis why this phenomenon happens will be studied in the following chapter. Before extracting any conclusions from those results, more measurements with a second independent technique to determine the angular divergence have been taken and are discussed in the following section.

6.4 The Siemens Star method

All the measurements performed with the gadolinium knife-edge were also done with the PSI Siemens Star. This includes two identical measurements per position to extract the average of the resolution. In figure 6.9 two radiographies are shown at two different distances, showing the increase in blurring caused by the penumbra.

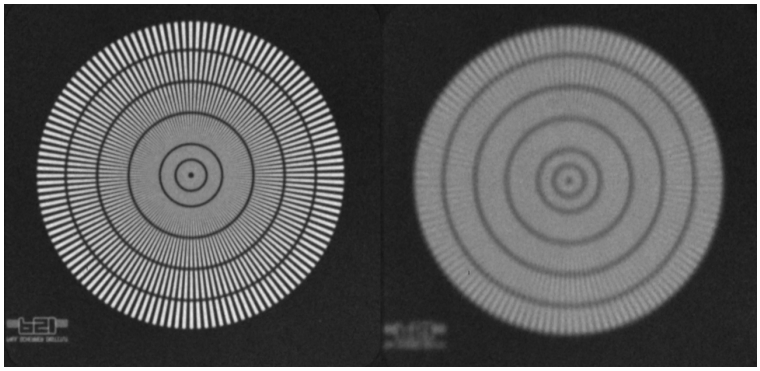

FIGURE 6.9: Two examples of measurements taken with the Siemens star in macro-position 1, at 10mm and 60mm from the detector respectively.

The precision to appreciate the resolution on the Siemens star by optical means is of $\pm 25\mu m$, and it's not always easy to distinguish at which point the threshold is, especially when considering the difference between the vertical and horizontal divergences. In order to improve the evaluation of the spatial resolution, a numerical approach has been taken. By means of the software ImageJ, the single image has been radially resliced from the centre to the most-external circle, starting at a 45° angle. The procedure is represented in figure 6.10. The image contains, on the right, a representation of the Siemens star "unfolded", where the top pixel row is equivalent to the 45° radius used to start the reslice. Dividing the image in 4 equal horizontal sectors allows to separate the 2 components of the divergence. Figure 6.11 shows the 4 images representing the resolution in the 4 different sectors of the Siemens star.
Evaluating the resolution by optical means, the best precision possible on the Siemens star is $\pm 25\mu m$. In order to improve that precision, the following method is adopted: for each single image, the standard deviation of every vertical array of points is taken (from left to right). The standard deviation is

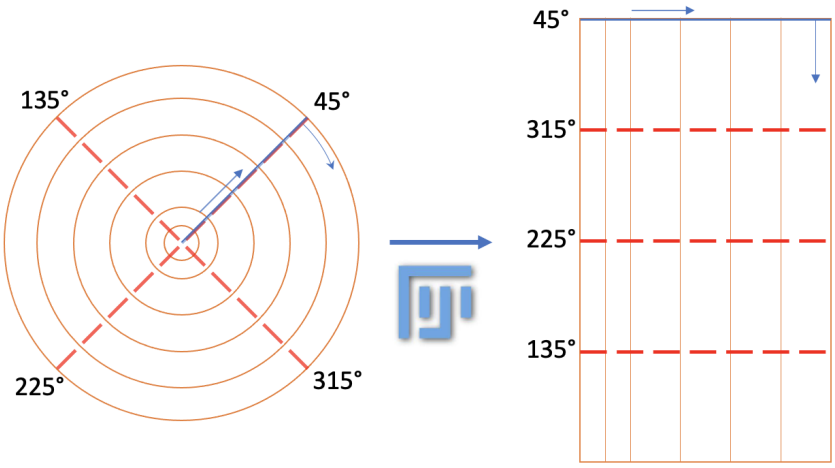

FIGURE 6.10: Representation of the process of "unfolding" the Siemens star using Fiji (ImageJ). The reslicing operation is done clockwise from the 45° line.

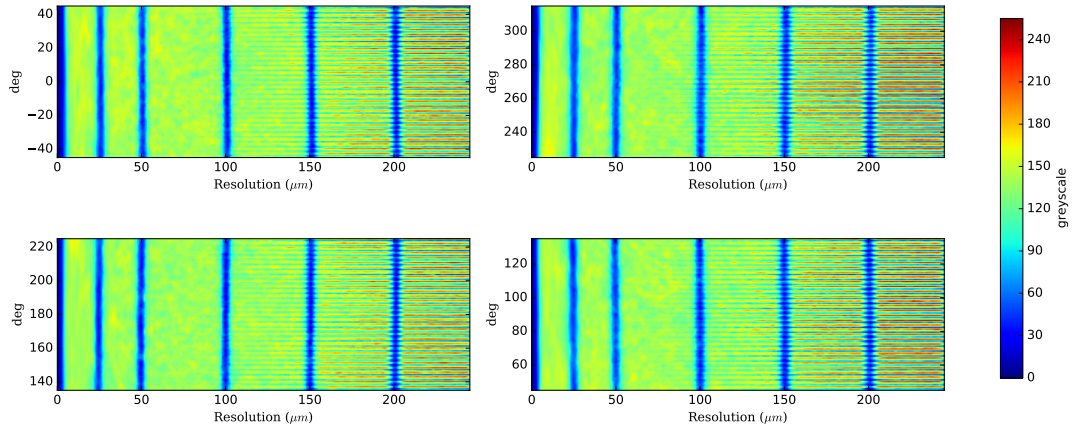

FIGURE 6.11: Visualisation of the unfolded and segmented Siemens star. The greyscale image is displayed using the "jet" LUT in order to highlight the difference between the noise region and the actual spikes of the Siemens star.

a measure of the amount of dispersion of a set of values, and thus the expectation will be constant and small on the first points, in the inner area of the Siemens star (inner rings, left-most area in each figure), where only noise is present. The standard deviation value will increase with the higher contrast (outer rings, right-most area in each figure). This is shown in figure 6.12, where the Standard deviation is plotted against the resolution. In the figure, the initial region is almost constant and it is possible to distinguish the valleys made by the Siemens star ring markers. The decrease in the standard deviation at those points is due to the fact that the points in the area corresponding to the incisions is more uniform than that of the surroundings, thus decreasing the variation. The quoted value for the spatial resolution is found at the intersection between the constant (on average) area and the sloped one.
To determine the value of the resolution, a threshold to distinguish signal from noise has been chosen. What has been noticed from the experimental

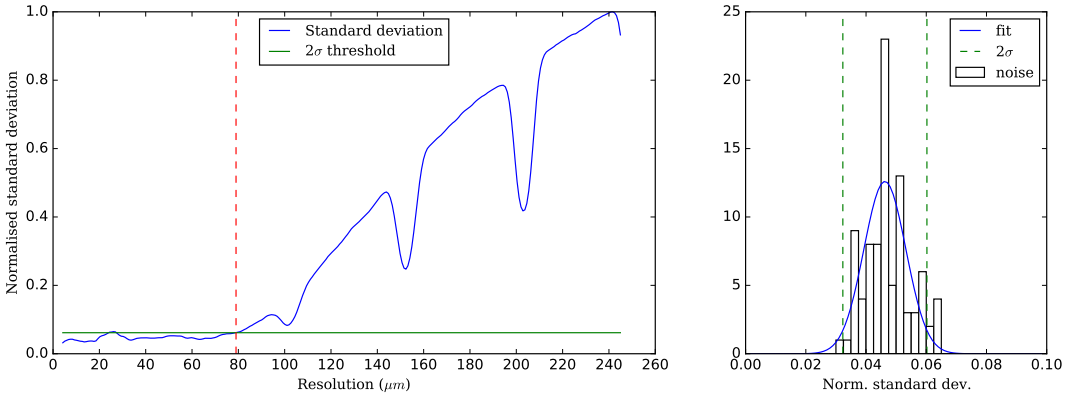

FIGURE 6.12: Left: Sample of the standard deviation of a measure in position 1, at 10mm from the detector. The red dotted line separates the noise region and the signal. Using a 2σ threshold, the value for the resolution is 79μm. Right: Histogram of the noise created by the standard deviation in the noise region. The noise is fitted with a Gaussian curve in order to obtain the 2σ threshold.

data is that, in the region where there is only noise, the pixel counting has a relatively small standard deviation (low contrast), while in the signal region the pixel count distribution has a larger standard deviation (high contrast). In figure 6.12 the green line represents the threshold, tuned to the region where only noise is present, set at 2σ. The red dotted line separates the noise and signal regions. A systematic study to evaluate the sensitivity of the result with respect to the choice of the threshold has been done, varying from 2σ to 5σ, observing a maximum variation on the final L/D of less than 5%. This possible systematic error is taken into consideration for the error calculation. For the horizontal resolution calculation, the average of top and bottom images are used, while for the vertical resolution the left and right are considered.
The procedure to calculate the effective L/D factor is done by repeating the process detailed in section 6.1 and converted to divergence angle through equation 6.6. The results for each macro-position are shown in figure 6.13 with the same notation as in figure 6.8. As seen with the results of the gadolinium knife-edge, the introduction of the ANET collimator on the set-up improves the divergence angle on each case and, in the same line as before, the performance of the CNC is far better than what was expected theoretically, corresponding to a geometrical acceptance of 0.36 degrees.

6.5 Results

In this section the comparison of measurements done by the gadolinium knife-edge and the Siemens star will be shown. As noted before, the ANET CNC improves the quality of the radiographies. This can be appreciated directly.
The collimator not only improves the divergence angle of the beam, but it also improves the resolution of the measurements point-by-point. One example is depicted in figure 6.14. By choosing the appropriate LUT[3] it is pos-

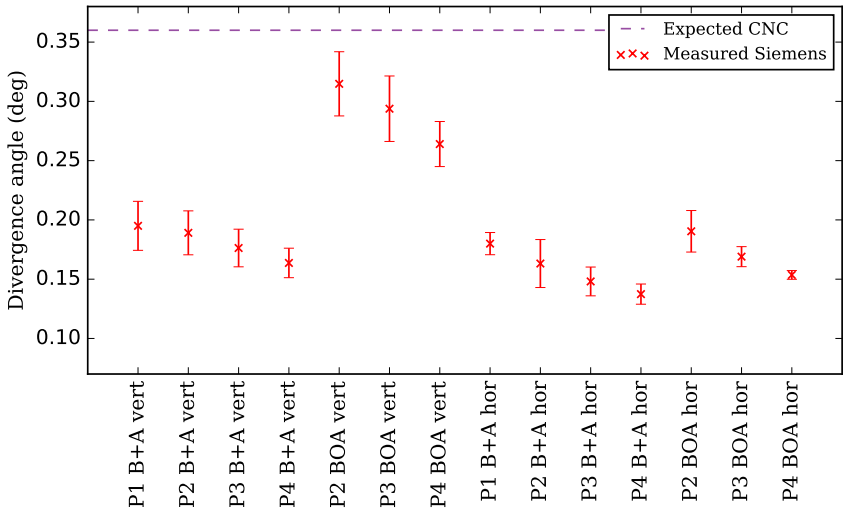

FIGURE 6.13: Calculated divergence angle on every configuration using the Siemens star. The label "B+A" stands for "BOA + ANET", while P1-4 correspond to the macro-positions 1 to 4 as detailed in the previous section in table 6.1. The errors have been evaluated using a Monte Carlo procedure and the ABC algorithm.

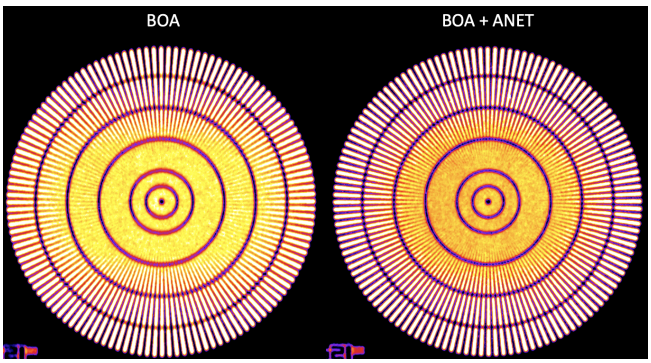

FIGURE 6.14: Comparison between two Siemens star measurements, without and with the ANET CNC, in macro-position 2, at 20*mm* from the detector.

sible to highlight the blurry areas and separate them from the well-defined regions of the Siemens star. The right image in which ANET is included in the set-up shows an evident improvement on the spatial resolution with respect to the image on the left, with BOA alone.
In order to quantitatively compare the gadolinium knife-edge method results with those of the Siemens star measurements, it is worth to show the results in a single plot: Figure 6.15.
The results are not coincidental, but they show the same behaviour and trend. The difference in absolute value between the two methods can be traced directly to the impact on the two threshold criteria used. Both the MTF and the Siemens star noise criteria chosen to obtain those results are sensible to the choice of threshold value. Despite that, it is possible to extract relevant assumptions and data from that graph.
Contrary to the initial assumptions, the measured divergences are not only

[3]Look Up Table, a colour palette.

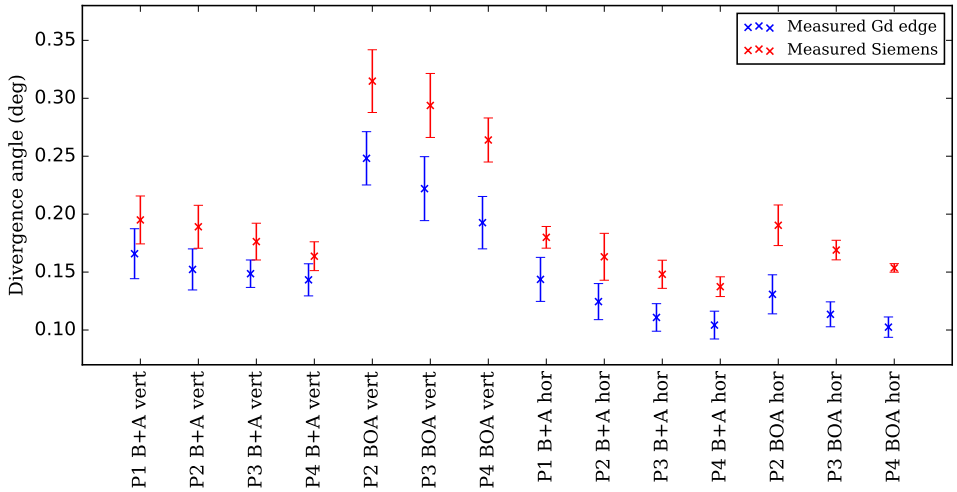

FIGURE 6.15: Graph showing the divergence angle calculated on each macro-position with both the Siemens star and the gadolinium knife-edge.

better than expected, but the ANET CNC improves the divergence even when the beam is geometrically more collimated. A second appreciation is that the absolute improvement is not the same for the vertical and horizontal axis, despite the collimator applying the same potential correction factor by having a square section geometry.
On the next chapter a hypothesis to explain the phenomena causing these results will be explained, as well as an introduction on how to extract the effective divergence angle from the simulations.

Chapter 7

The Acceptance Curve parametrisation and the beam divergence calculation

The measurements performed at the PSI BOA facility have shown an unprecedented improvement on the quality of the beam collimation. This improvement was not predicted by a simple geometrical model. More complicated effects rise when combining two collimation systems.
The original geometrical model states that, in case where two collimators are concatenated in a set-up, the one with the higher L/D will determine the final collimation power of the system. This assumption is not wrong, and in fact it is also confirmed by the simulation. The most divergent neutron after the collimator to reach the detector has, indeed, an angle of 0.36, appertaining to an L/D factor of 160. The reason why the measurements do not reflect the predicted result is that the model only takes into consideration the geometrical properties of the system. The divergence distribution of the neutrons after the first collimator is different from the original source.
A formal description of the complex convolutional effect between both collimators is described in the following sections.

7.1 Mathematical description

Both algorithms explained in chapter 5, McStas and NeDiMo, share the same treatment for the transport of neutrons through absolute absorbing collimators. They give a geometrical treatment to the problem, and it can be described through the following formula, for the 2D case:

$$P_{2D}(\theta) = \int_x \rho(x,\theta)\delta(\theta|x)dx \tag{7.1}$$

This equation describes the probability distribution of a neutron to survive the collimator, $P(\theta)$, calculated through the integral of the initial space and angular distribution, $\rho(x,\theta)$, and a step function which can either take values 0 or 1, depending on whether the neutrons are absorbed or not, which is determined by the angle given a certain position. To calculate the shape of this function, a very simple empirical simulation has been designed: since the probability of passing through the collimator is either 0 or 1, a simple channel was designed, with given characteristics (L and D), and every possible

neutron within an angular range of [-θ,+θ] and an spatial range of [$-\frac{D}{2}$,$+\frac{D}{2}$) was simulated. The output of this model is the distribution $P(\theta)$ which describes the probability of survival through the given collimator. Figure 7.1

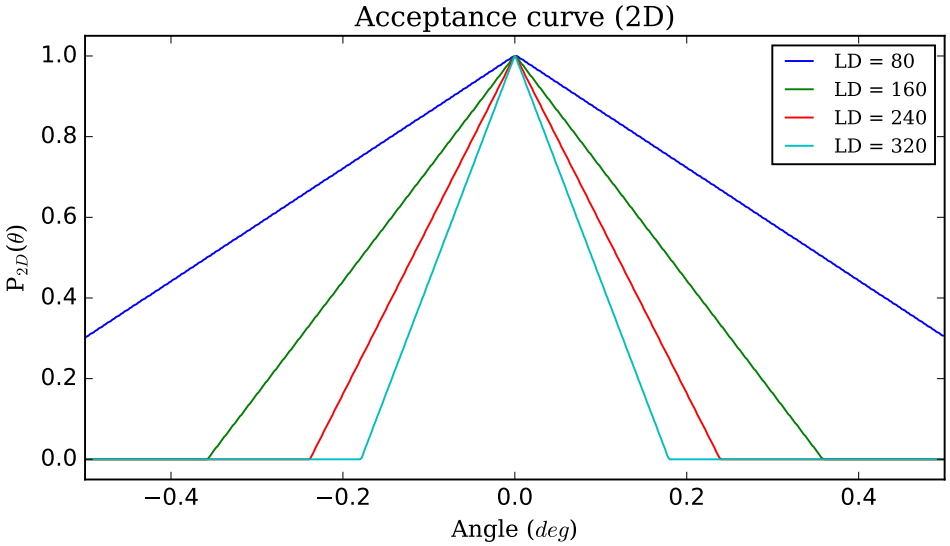

FIGURE 7.1: 2D acceptance curves calculated at different values of L/D.

shows some acceptance curves generated with different L/D values. These curves can be parametrised with a straight line function, which is:

$$P_{2D}(\theta) = \theta\left(arctan(\frac{1}{L/D})\right)^{-1} + 1 \tag{7.2}$$

The value $\left(arctan(\frac{1}{L/D})\right)^{-1}$ essentially describes the limit angle over which the probability of survival is 0[1].
The model can be expanded to 3D, in order to evaluate the total divergence, instead of evaluating only one axis. When treating the collimator in 3D, two more variables are added: there are two spatial coordinates (x, y) and two angular coordinates, the divergence from the propagation axis, θ and the rotation along the propagation axis, ϕ, which is sampled in $[0, 2\pi]$. The formula that describes the mathematical model is:

$$P_{3D}(\theta) = \int_x \int_y \int_\phi \rho(x, y, \theta, \phi)\delta(\theta, \phi|x, y)dxdyd\phi \tag{7.3}$$

The solution of $P_{3D}(\theta)$, contrary to the 2D version, depends heavily on the geometry of the collimator. In the ANET CNC, the 3D distribution follows:

$$P_{3D}\left(\sqrt{\theta_1^2 + \theta_2^2}\right) = P_{2D}(\theta_1) \cdot P_{2D}(\theta_2) \tag{7.4}$$

This relation is due to the square geometry of the collimator individual channels. Figure 7.2 has the result of some calculations of the 3D acceptance curves. Contrary to the 2D case, in the 3D version the θ value has a mini-

[1] As it is a probability, negative values are equal to 0.

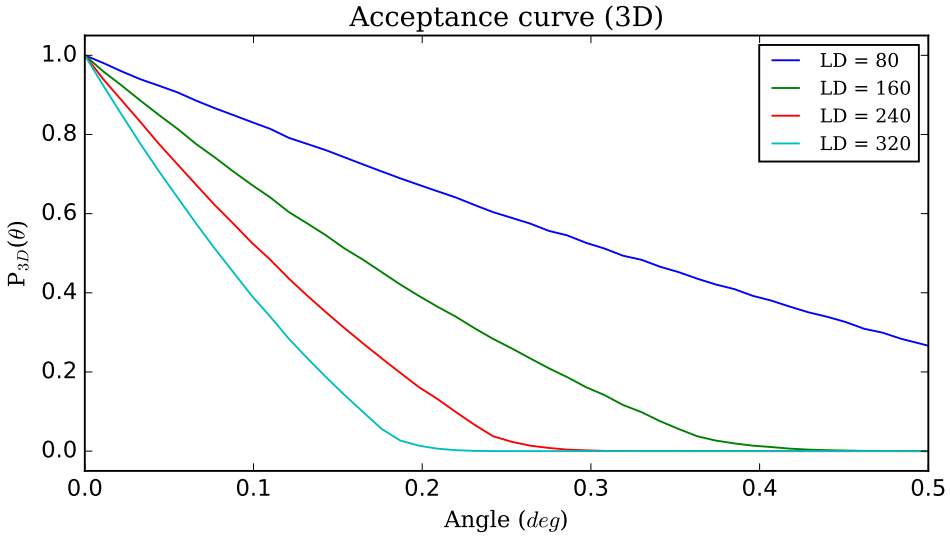

FIGURE 7.2: Different acceptance curves calculated in 3D.

mum value of 0. This is due to the ϕ being sampled from 0 to 2π.
This function acts as a mask over the incident beam, altering the shape regardless of the initial beam divergence. To test this hypothesis, the angular distributions from the BOA facility simulation, described in chapter 5, have been used. The beam divergence distributions before and after the collimator have been simulated. If the mathematical formula is correct, multiplying the angular distribution present at the entrance window of the collimator by the mask should result in the beams angular distribution at the exit window. This is discussed in the following section.

7.2 Testing the Acceptance Curve parametrisation

The set-up has been simulated in 2 positions: with the CNC at 5.23m from the BOA exit window, and at 20cm. The calculation test has been done considering both the 2D and 3D cases.

7.2.1 The 2D cases

Both close (figure 7.3) and far (figure 7.4) configurations have been simulated. The plots in the figures have been normalised to the maximum value of each plot, in order to compare the shapes of the distributions. All cases show a very good agreement between the calculated distributions and the simulated ones. Those plots render evident the difference in the BOA facility between the vertical and horizontal distributions. The bender present along the guide creates distortions on the horizontal axis, as expected. The plots of the vertical divergence shows a wide and uniform distribution before the CNC, which is strongly reduced by the collimator down to the shape of the acceptance curve. On the horizontal axis, instead, the irregular shape of the angular distribution is still very well predicted by the model, as it adapts onto the shape of the acceptance curve. When the ANET CNC is installed far from the exit window of BOA (figure 7.4), the pin-hole collimation of

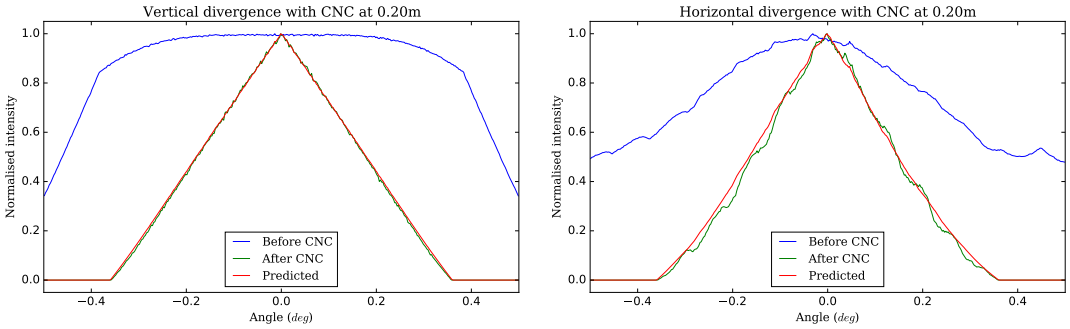

FIGURE 7.3: Vertical and horizontal angular divergence distribution plots before and after the ANET CNC along with the predicted distribution. Simulation done with the CNC at 20 *cm* from the exit window of BOA.

the beam reduces the maximum angular divergence to less than 0.5 degrees. On the vertical axis, the distribution has, at the tails, two secondary peaks, artifacts generated by the beam construction, as explained in the previous simulation chapter 5. Those artifacts get eliminated by the collimator, which also shrinks the distribution. On the horizontal axis, the effect of collimation

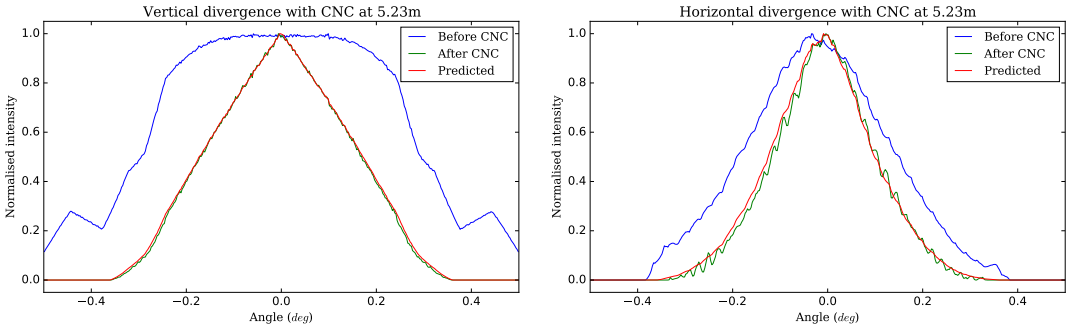

FIGURE 7.4: Vertical and horizontal angular divergence distribution plots before and after the ANET CNC along with the predicted distribution. Simulation done with the CNC at 5.23 *m* from the exit window of BOA.

is less prominent than on the vertical axis, but there is still a reduction of the more divergent neutrons.

7.2.2 The 3D cases

Regarding the 3D calculation, the formula used to extract the analytical shape is reported in equation 7.4, leading to the following results in figure 7.5. The effect of the ANET CNC is very apparent in both cases, but specially when the collimator is close to the exit window of BOA. All the neutrons beyond the 0.50 limit angle are absorbed, while the whole distribution shifts towards smaller divergence angles. On the far set-up configuration, the angular distribution without the collimator is more irregular, and it becomes smoother when the ANET CNC is present in the set-up. In both close and far configurations, the model accurately predicts the impact of the ANET CNC on the angular divergence of the beam.

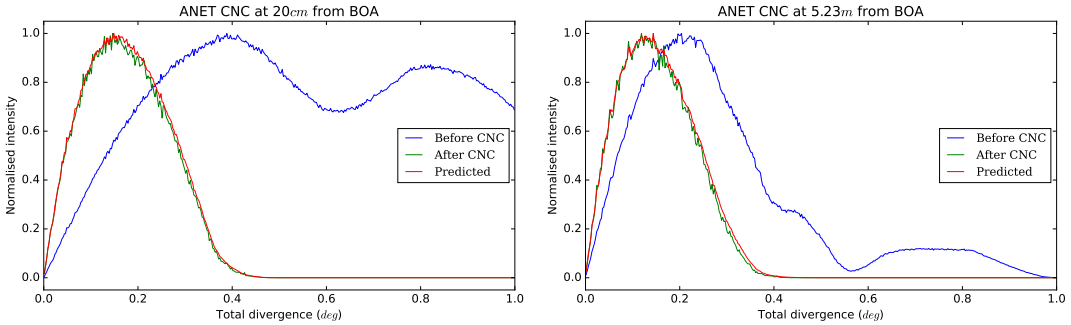

FIGURE 7.5: Results of the simulations of the 3D neutron angular distribution before and after the ANET CNC, along with the analytical calculation of the resulting angular distribution.

7.3 Physical implications

A first important consequence of the curve of the mathematical acceptance model is the fact that the collimator has an active effect in altering the quality of the image, regardless of the angular divergence of the initial beam. A second consequence is that the collimator doesn't alter the absolute divergence if the beam is more collimated, as the endpoint of the distribution after the collimator doesn't change. The improvement in the image quality is due to the reduction of the number of neutrons present at high divergence angle, not because the collimator fully eliminates them.
This hypothesis is not limited to the ANET CNC, as at no point within the calculations the full ANET geometry has been imposed. The model has been done for a single collimation channel, and the calculations for the 2D model are perfectly applicable to a circular collimator or a pinhole, for example. Using this hypothesis, the combination of more than one pinhole, or the ANET collimator itself, can be used as a beam divergence corrector. Equations 7.3 and 7.4 imply that the effect of the collimator is null on the perfectly straight neutrons, while the greater the angle, the better the absorption, up to 1 when that angle is beyond the geometrical acceptance of the collimator.

7.4 Calculating the divergence angle from the simulation

By means of the McStas code presented in chapter 5, the whole set-up has been simulated on each macro-position, with the aim of calculating an approximate value for the angular divergence. In order to restrict the angular divergence only the neutrons that effectively participate on the measurement of the spatial resolution, a squared section of $1cm^2$ has been selected, placed on the centre of the detector. This region of interest is approximately the area used to measure both the MTF in case of the gadolinium knife-edge, and the area corresponding to a sector in the Siemens star. The graph array in figure[2] 7.13 depicts all the angular distributions, both vertical and horizontal, in all positions with and without the ANET CNC.
This figure contains, for each measured position, both the horizontal and vertical components of the angular distribution of neutrons. One common

[2]This figure has been placed at the last page of this chapter due to formatting reasons.

characteristic in every scenario is a typical triangular shape of the distribution. This is direct consequence of the effect of the acceptance curve. It is relevant to notice that, related to the application of this acceptance curve, the endpoint of a distribution doesn't change when adding the ANET CNC if that endpoint is below the acceptance angle. This acceptance angle is slightly below the aforementioned 0.36 degrees, as the reduced window diminishes the angular range of the neutrons reaching the detector from the collimator.
Although the endpoint of the distribution doesn't change, the shape does. Obtaining the value for the maximum measurable divergence -which determines the spatial resolution of the image- is fairly easy on the cases in which the distribution has a sudden end, by picking the angle at roughly the middle height. This same criterion, though, is not so trivial on the cases with a strong slope. To try to uniformise the determination of the L/D in all cases, both vertical and horizontal, the following approach has been taken: through an optimisation procedure with a minimisation of χ^2 and considering a threshold value ranging from 0 to 1, comparing the simulated value in each case with the results measured both with the gadolinium knife-edge and the Siemens star. The point in which the χ^2 is minimum should, ideally, be common for both systems. The result of the calculation is found on figure 7.6.

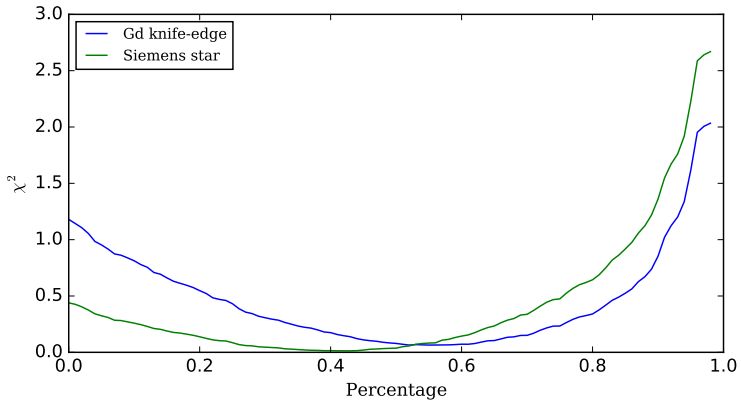

FIGURE 7.6: Result of the calculation of the χ^2 with all the measures from the gadolinium knife-edge and the Siemens star.

The respective minima for the χ^2 in both measurements sets are found at percentages of 0.55 and 0.43 for the gadolinium knife-edge and the Siemens star respectively. The final L/D numbers are obtained by applying the coincidence percentage, 0.53, as threshold in every case. The uncertainty is calculated as a projection of a $\pm 10\%$ variation of the vertical value to the horizontal axis.
The results in figure 7.7 show a similar trend for the data measured with the two techniques and calculated through the simulations. The results are in agreement.
All three measuring strategies show the same trend, despite differences on the absolute value for the divergence. With the acceptance curve, the phenomena of uniformisation of the vertical and horizontal divergences when introducing the ANET CNC in the system is explained, as the collimator has an effect which is dependent of the angle, through the whole angular spectrum of the incident beam, not only on the most divergent component as

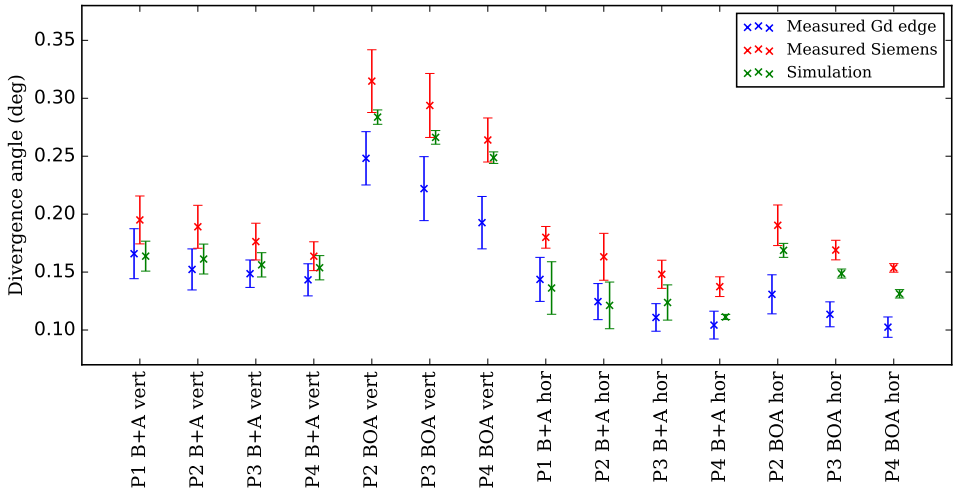

FIGURE 7.7: Graphical summary of all the measurements with the gadolinium knife-edge, the Siemens star and the calculated values.

previously assumed.

7.5 Comparing the ANET CNC to a pin-hole collimator

A performance study has been conducted comparing the ANET prototype with an equivalent pin-hole system under simulated experimental conditions. The goal of the study is to determine how well does the ANET CNC fare against a traditional pin-hole system in terms of quality of the neutron beam for neutron imaging, i.e. how spatially uniform the divergence distribution is, how collimated the beam at the sample is, and how big the neutron flux is. The first two elements determine the radiography quality, while the third sets the exposure time required. The characteristics of both systems are detailed in table 7.1.

ANET CNC	Pin-hole
L/D = 160	L/D = 160
N. channels = 200	Diameter = 10 mm
Channel size = 2.5x2.5 mm^2	Det. distance = 1600 mm
Length = 400 mm	Detector FOV = 50x50 mm^2
Field of view = 50x50 mm^2	
Detector FOV = 50x50 mm^2	

TABLE 7.1: Characteristics of the simulated ANET CNC and pin-hole systems.

From a geometrical perspective, the ANET CNC performs a more severe selection over the incoming neutron flux with respect to the pin-hole system. This can be appreciated from the comparison between the acceptance curves in figure 7.8.
From the acceptance curves, is evident that the selection applied by the ANET CNC is of higher quality with respect to the pin-hole system. This is due to the "tube" geometry of the channels of the CNC, not present in case of a single pin-hole, where its open geometry allows for more divergent neutrons

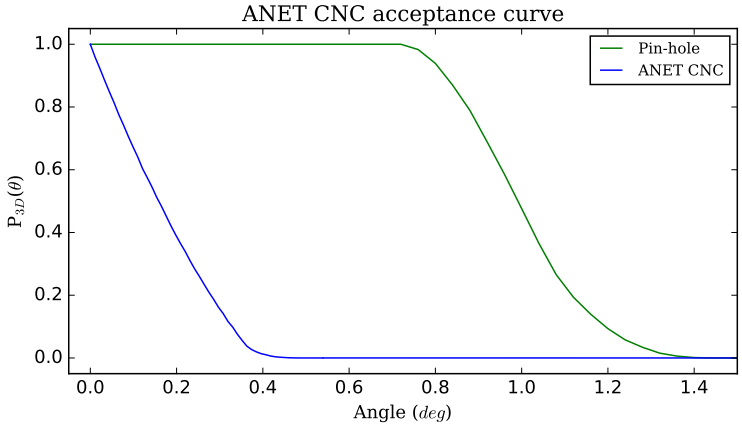

FIGURE 7.8: Comparison between the 3D acceptance curves of the ANET CNC and an equivalent pin-hole system.

to reach the detector. This is not present in case of the ANET CNC, where only those neutrons with a strict angular aperture are capable of surviving the collimator.
Both systems have been simulated using McStas and assuming simple flat source. The comparison of the 2D angular distribution of neutrons as measured at the detector is shown in figure 7.9.

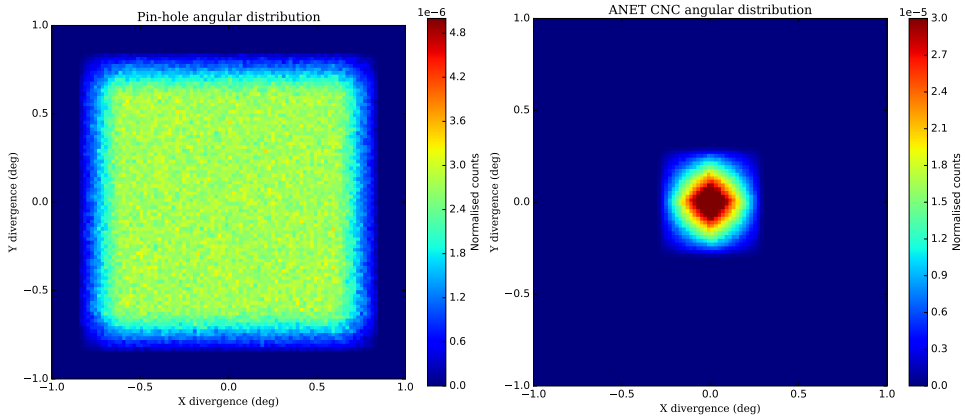

FIGURE 7.9: Comparison between the 2D angular distributions of the pin-hole and the ANET CNC on the detector. The neutron survival probability is plotted against the divergence angle.

The two graphs represent the angular distribution of neutrons in both systems, and show a higher concentration of highly collimated neutrons in the ANET configuration. The neutrons measured at the detector with the pin-hole system are angularly very spread with a quasi-uniform distribution between ± 0.8 degrees. On the other hand, the ANET system shows higher degree of collimation, within ± 0.36 degrees in both x and y. To understand the impact of the divergence distribution on the final image quality, it is necessary to study the maximum divergence spatial distribution on the detector. The comparison between both systems is shown in figure 7.10. The colour map highlights different areas of maximum divergence value, which in turn correspond to areas of different resolution values.
The plots highlight the same effect already noted on the acceptance curve:

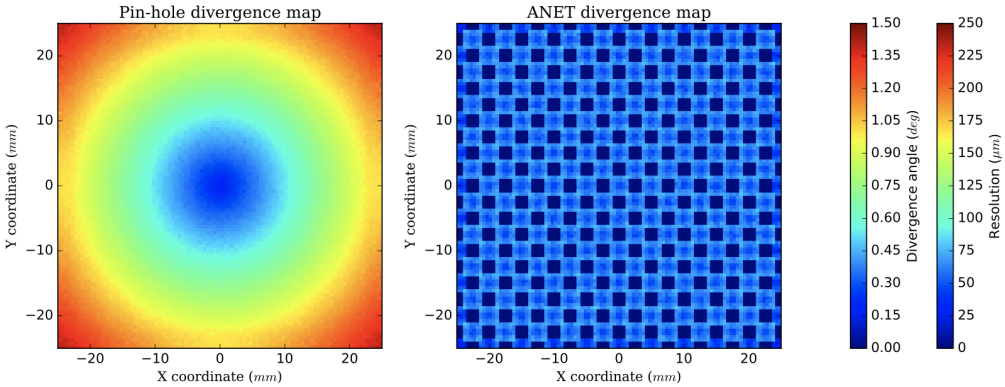

FIGURE 7.10: Comparison between the 2D maximum divergence distributions of the pin-hole and the ANET CNC on the detector. The two colour map scales show the divergence angle and the equivalent geometrical resolution measured when a sample is placed at 30 *mm* from the detector (calculated using equation 1.7).

the pin-hole system does a poorer selection of angular divergences, which in turn translates into a central region with an elevated collimation, that decreases with the distance from the centre. This in turn implies that the image resolution measured in the centre is better to that on the external area. On the other hand, the ANET CNC delivers a very stable collimation throughout the whole field of view. As proven in previous chapters, the chessboard structure visible in this static image disappears when the dynamic acquisition in applied. This is the main advantage of the scalable ANET design, thanks to which the quality of the image does not depend on the field of view.
The higher quality of the ANET CNC system can also be appreciated by comparing the 3D angular distribution of the neutron beam at the detector. This is shown in figure 7.11.

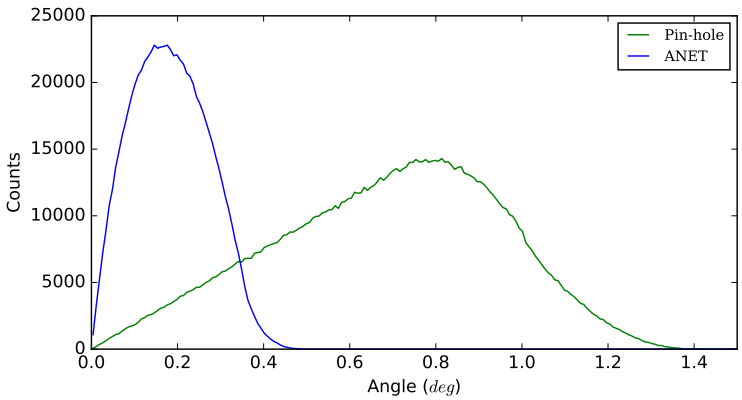

FIGURE 7.11: Histograms comparing the number of neutrons on each angle, calculated on two simulations with the same number of particles.

From the two histograms in figure 7.11 there are two considerations which are important: The first relevant conclusion is the fact that mostly all of the neutrons exiting from the ANET system are greatly collimated (at an average of 0.26 *deg* and a maximum angular divergence of 0.51 *deg*), while the average value in case of the pin-hole distribution is found at an angle of 0.69

degrees. Nevertheless, the area under the two curves is not the same, as the pin-hole has a greater acceptance than the ANET CNC. This implies that, in a direct comparison between a 10 mm pin-hole and the tested prototype of the ANET CNC, the total flux measured at the detector is greater in the pin-hole case. The difference in flux can be compensated (see figure 7.12) by taking advantage of the scalability of the ANET design: by increasing the field of view from a 5 x 5 cm^2 up to a 10 x 10 cm^2, the effective flux is multiplied, while the quality and the uniformity of the beam remain the same.

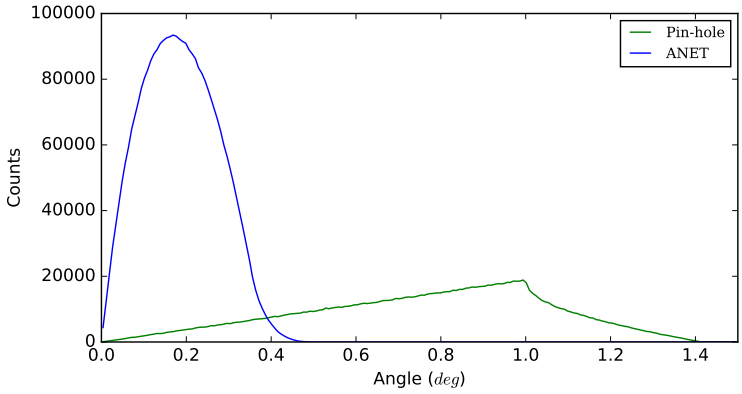

FIGURE 7.12: Histograms comparing the number of neutrons measured on a 10 x 10 cm^2 ANET CNC and a pin-hole system, with a L/D factor of 160 and a detector of 10 x 10 cm^2.

Figure 7.12 shows the massive difference in flux that the ANET CNC can deliver when scaling the field of view, without compromising the neutron divergence at the detector nor the quality of the images.
With this work the ANET CNC has proven to be an excellent instrument for neutron imaging. The scalability of the field of view and L/D factor deliver a very reliable collimation system with a high degree of adaptability to different conditions. The ANET CNC is capable of delivering higher fluxes than common set-ups, as well as more uniform beams in terms of angular divergence.

The next chapter will be a first application of the ANET CNC system to a tomography. Two samples have been studied: a small Afghan lapis lazuli and a Dutch iron fibula. This application was a step beyond what was expected at the beginning of this thesis work.

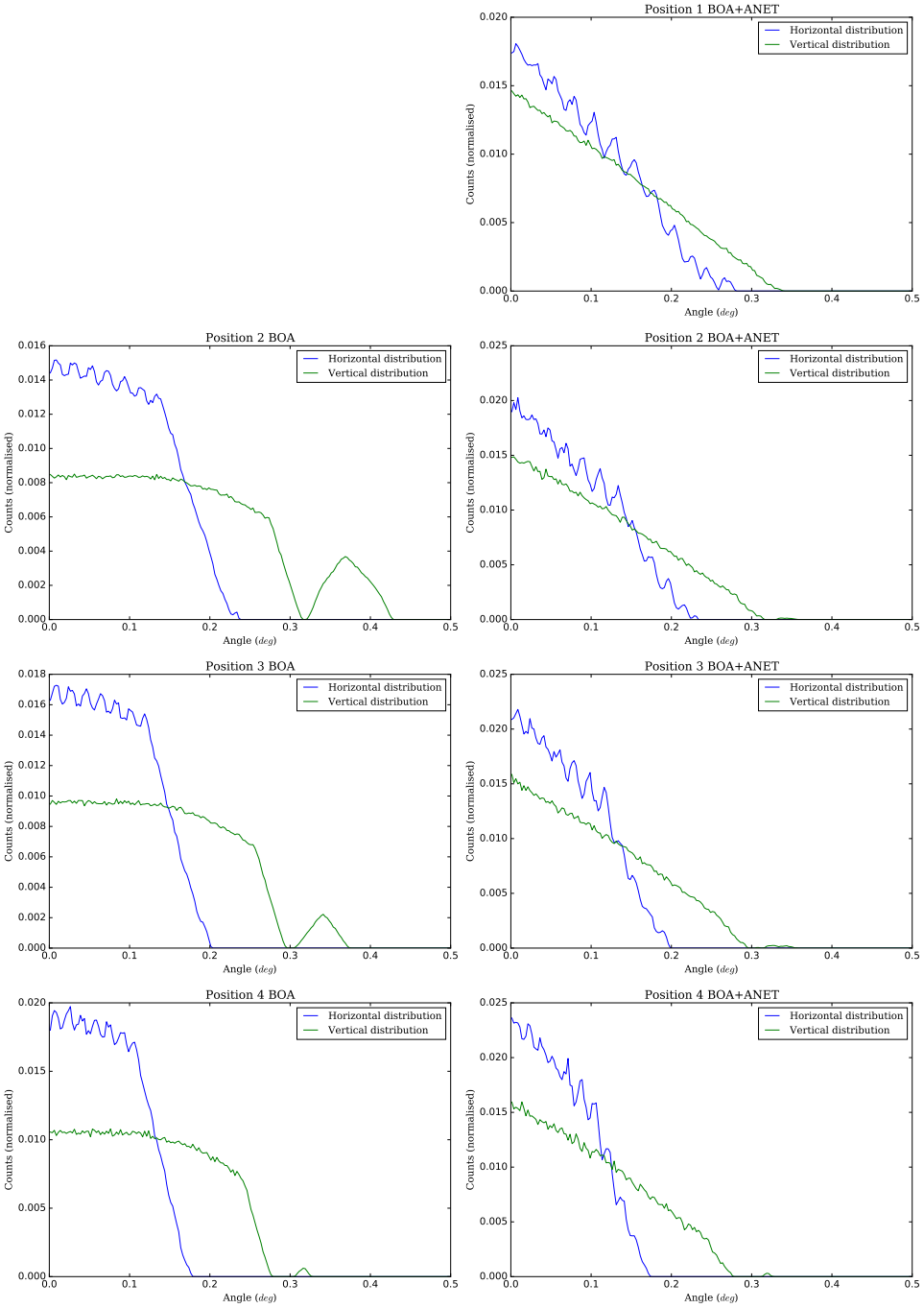

FIGURE 7.13: Simulations of the angular neutron distribution in all macro-positions with and without the ANET CNC.

Chapter 8

Application to tomography

In the previous chapters, it has been proven that the ANET collimator is capable of delivering highly collimated neutron fluxes within a limited space to produce neutron radiographies without disturbances and with the expected resolutions.
During the experimental campaign at the Paul Scherrer Institute, at the BOA beamline, the opportunity arose to study two small objects: an iron fibula from northen Europe, circa X century, and an Afghan lapis lazuli. Those objects have been chosen on purpose as they have very different scattering and absorption properties. This chapter, as a possible application of the ANET CNC, describes the attempt at a tomographic reconstruction of those samples.

8.1 The experiment description

The set-up used for the tomography is the one described in the previous chapter 6, with the addition of a rotary stage between the ANET CNC and the detector, on top of which the two small pieces were placed.

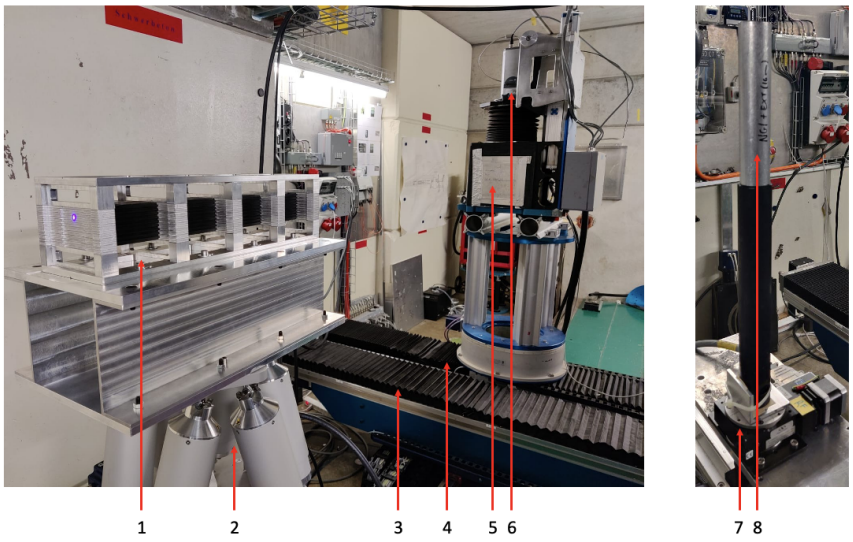

FIGURE 8.1: The measurement set-up (left) with a detail on the rotary stage (right). (1) The ANET CNC, (2) The Stewart platform, (3) The T5 stage, (4) The T6 stage, (5) The ZnS-Lif(Ag) scintillator, (6) The Andor cooled camera, (7) The rotary stage, (8) Samples for the neutron tomography inside the aluminium tube.

The measurements performed consist on 375 radiographies at independent angles, with an exposure time of 140 seconds each. The collimator system is operated under a continuous dynamic pattern acquisition with the Stewart platform as explained in section 4.1.2. The number of radiographies has been tuned to be greater than 360 and odd, in order to maximise the information extracted from each projection aiming at a discrete quality tomography. The exposure time was chosen to be high enough to have a good signal-to-noise ratio and to maintain a stable and repeatable dynamic pattern throughout the whole measurement.

8.2 Tomography reconstruction

In order to perform a tomography reconstruction from the radiographies taken, two software suites have been used: ImageJ [61] for the arrangement and preparation of the images and Octopus Reconstruction [62] for the normalisation of the image array, the creation of the sinograms and the reconstruction itself.
All the images have first been filtered using ImageJ and, to avoid undesired artefacts, de-noised by applying a removal of bright outliers. There has been no need to apply a beam hardness correction. During the pre-processing, though, a particular patterned phenomenon has manifested, as shown in figure 8.2. This plot is generated when taking a squared region, 40 pixels x 40 pixels, identical on each projection and averaging the pixel values within. This array of values is then plotted as a function of the projection number. A periodical distortion is observed. This can be caused by two independent

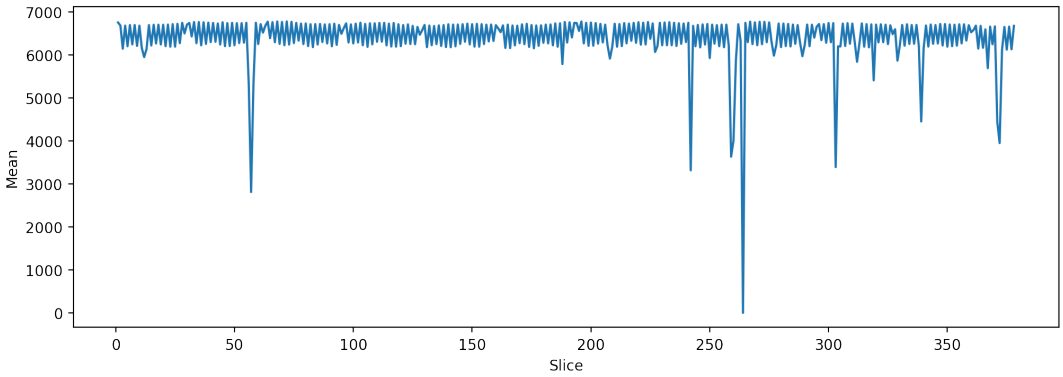

FIGURE 8.2: Average Z-profile on a small squared area devoid of sample, extracted from the tomography dataset.

sources: a regular alteration of the beam's intensity, which actually happened roughly every 3 minutes during the acquisition, and a small mismatch between the infinite pattern movement of the Stewart platform and the acquisition, in which, at regular intervals, the period of movement didn't match the exposure time of the camera. There are also several projections which clearly have a drop in intensity due to malfunctions in the beam. To sort this problem out, the solution has been to remove the low-statistics projections, as they would disturb the result once normalised to a common open beam, and write down the eliminated angles on a file for the reconstruction.

Some of the raw images that pass the first intensity filter still have distortions present. Despite, those elements are eliminated once the normalisation is applied (following the process in equation 1.9). Figure 8.3 shows the difference

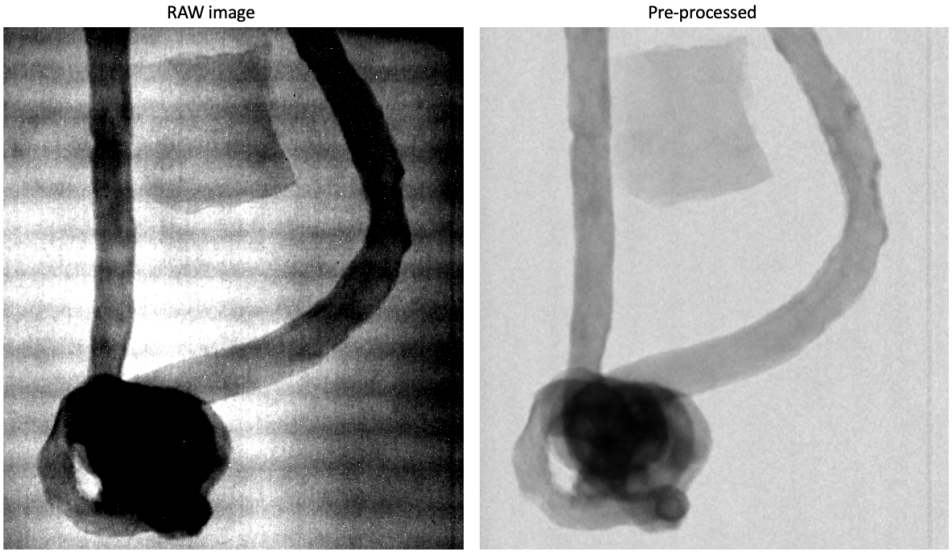

FIGURE 8.3: Comparison between the raw image and the pre-processed result after the normalisation and de-noise.

between the raw image and the pre-processed result. One important detail regarding the images is that the alterations due to the collimator have an impact only in the intensity of the image, not on the resolution. Proof of that is that in the regions where the disturbances were present, once normalised, the resolution remains the same as the rest of the image.
The tomography reconstruction has been done with the Octopus Reconstruction software, following the procedure explained in section 1.5.
Both objects studied are very different in terms of scattering and absorption power, but they were sampled together. Because of that, two different dynamic ranges within the 16-bit have been chosen, one for each, in order to maximise the quality information from each tomography.

8.3 Results

In the following, the results will be shown individually for the two objects.

8.3.1 The iron fibula

The iron fibula presented extensive corrosion along the surface and deep wearing due to time and poor conditions. Figure 8.4 shows three different

FIGURE 8.4: False colour 3D models of the reconstructed fibula. 1- "pristine metal" volume fraction unaffected by the corrosion, 2- Transparent isosurface which represents the effective mineralised layer.

False colour 3D models which highlight the different neutron attenuation produced by the different elements present in each compound. Hydrogen

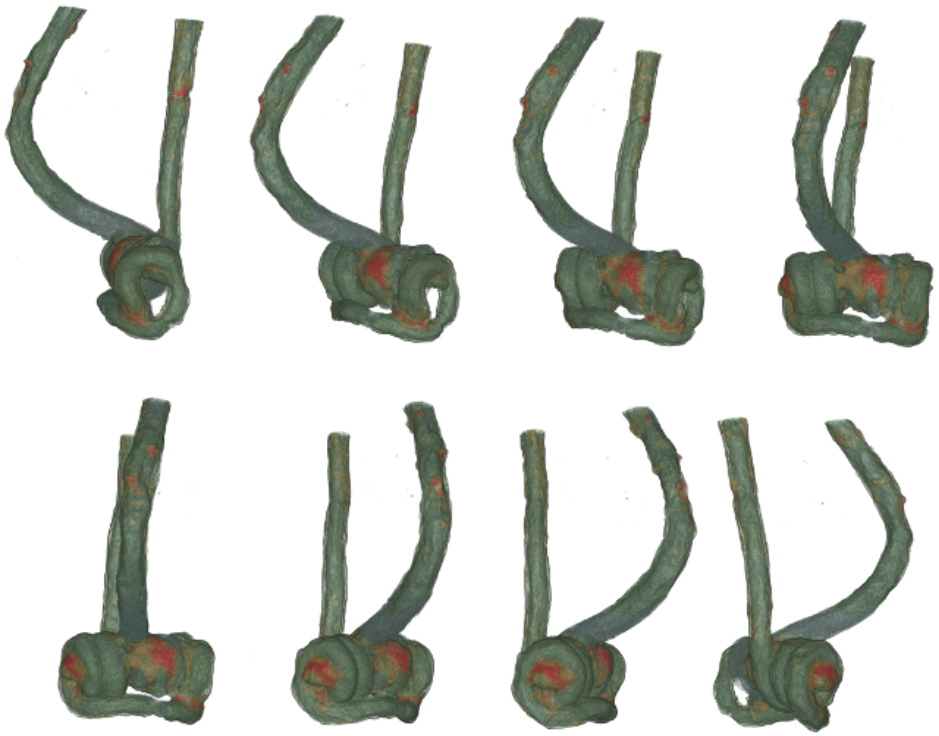

FIGURE 8.5: Rotation of the False colour 3D map representation of the iron fibula with a highlight on the largely attenuating corrosion.

is commonly associated with light elements (oxygen or sulfur) present in

the mineralisation products of the metal. In iron, one of the main corrosion phases is goethite ($Fe^{+3}O(OH)$). Due to the strong neutron scattering interaction of hydrogen it is possible to map the corrosion phases on the whole volume. Higher attenuation can be related to a greater presence of hydrogen-rich mineral phases, which entails an advanced corrosion stage. Figure 8.5 shows some different points of view from the same 3D False colour model in which the distribution of the corrosion can be appreciated. On this sample, the quality of the tomography delivered by the BOA+ANET CNC combination has been good enough to extract useful information regarding the geometry and state of conservation.

8.3.2 The lapis lazuli

Lapis lazuli is a metamorphic rock highly priced in antiquity due to its characteristic intense blue colour. It is mainly composed of lazurite, a blue feldspathoid silicate mineral[1] with the formula:
$(Na, Ca)_{7.5-8}(Si, Al)_{12}(O, S)_{24}(SO_4, Cl)_{1.3-2}$[2]. Other materials which compose the lapis lazuli are: calcite ($CaCO_3$), pyrite (FeS_2) or diopside ($CaMg(SiO_3)_2$). The lapis lazuli is a very complex rock, with over 30 different phases being reported in literature [63–65], some containing also sodalite, as well as minor traces of other minerals, such as augite, enstatite or mica. The content of the sample studied was essentially lazurite, calcite and pyrite.
In the lapis lazuli it is fairly easy to distinguish the pyrite from the other two components due to the iron present in the mineral, which makes it more attenuating with respect to the other two phases. The lazurite and calcite

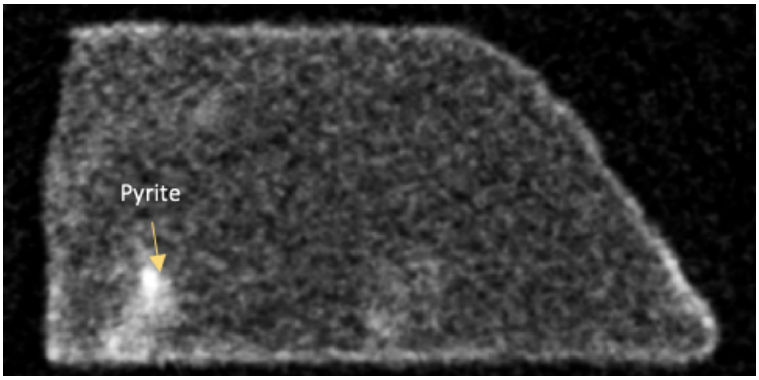

FIGURE 8.6: Slice of the reconstructed tomography from the lapis lazuli. The pyrite can be individualised with ease, as the contrast is very different from the other two phases. The calcite and lazurite are very similar in attenuation, and thus remain harder to distinguish.

have their most elevated attenuation coefficient with the calcium and oxygen, which are common in both, and their relative transmission (for 1 *cm* of material) for thermal neutrons is respectively 94.5% and 97.6%[3], which is barely distinguishable compared to the 70% of the pyrite, easily identified in figure

[1] Group of tectosilicate minerals similar to feldspars but with different structure and much lower silica content

[2] There are different formulae for lazurite, but the neutron attenuation barely changes between the different alternatives.

[3] Data extracted from the NIST site.

8.6. The lazurite and calcite are very dispersed, but regions with a higher concentration of those minerals, on average[4], can be individualised with a high quality tomography. Figure 8.6 presents a slice from the reconstructed tomography, in which the pyrite is easy to separate. It's nonetheless complicated to deliver reliable appreciations regarding the distribution of lazurite and calcite with this tomography quality. Figure 8.7 shows different cuts on

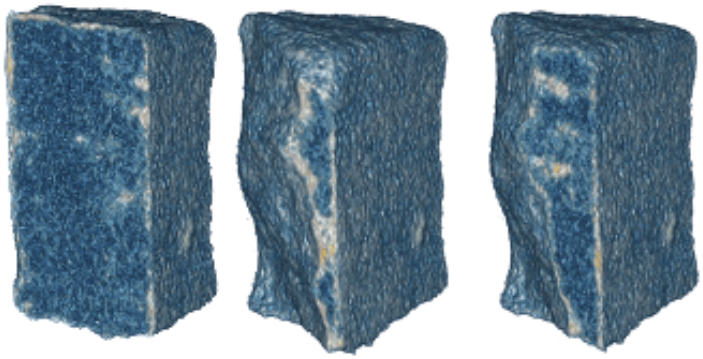

FIGURE 8.7: False colour 3D model of the lapis lazuli, with three different cuts to highlight, with the appropriate colour map, the different material distributions within the mineral.

the False colour 3D model of the tomography of the lapis lazuli. The results are good enough to extract reliable information from the samples, such as the internal distribution of pyrite within the lapis lazuli, and up to a certain point to identify different veins and sheets with a higher concentration of calcite and lazurite.
Both the results obtained with the iron fibula and the lapis lazuli are encouraging regarding the performance of the ANET CNC with tomography. They deliver a proof of concept of the validity and utility of the collimator for this application. Further measurements in the future with optimised parameters, increased statistics and at dedicated measuring campaigns give hope at reaching even better results.

[4]Single minerals can be smaller than a micrometer, thus impossible to distinguish with this technique. Only an average over a greater region is identified.

Chapter 9

Conclusions

In this thesis work the design, construction and test of a novel compact multi-channel neutron collimator has been illustrated. Its performances have been evaluated and a first application on a tomographic reconstruction has been described.

The ANET CNC has a scalable structure, both in collimation power and in field of view. It needs to be coupled to a moving stage in order to smooth out its chess-board geometry form the final image. This is fully demonstrated and tested. The dynamic acquisition mode can be tuned in size, pattern and speed to adapt to different facilities.

The performances of the ANET CNC have been evaluated in different facilities with standard reference samples. For this purpose, both reactor and accelerator-based sources not optimised for neutron imaging were chosen. There has been an obvious improvement in spatial resolution in every instance in which the ANET CNC has been introduced in the beamline. The collimator has been tested under fluxes from 10^6 up to 10^9 $cm^{-2}s^{-1}$ and no bottleneck has been observed.

An extensive simulation work using high-end tools has been conducted in order to further study the device properties. The agreement between the experimental and simulated data is remarkable.

Most of the experimental work has been conducted at the LENA facility in Pavia (Italy) and at the BOA facility at the PSI (Switzerland). In the last case, the beamline was characterised by the presence of a traditional pin-hole system. The inclusion of the ANET CNC was in combination of the former set-up. A theoretical work has been conducted to explain the unexpected improvement in spatial resolution measured when combining the two collimating systems. The effect has been mathematically described and verified through the simulations. The theoretically calculated values for the beam divergence are in agreement with those measured in the experimental campaigns.

The ANET CNC has been compared, through simulation, with a similar traditional pin-hole system in terms of quality of the beam for neutron imaging. It has been proven to deliver better suited neutron beams with a high degree of uniformity throughout the whole field of view, as well as a scalable flux.

The capabilities of the ANET CNC to perform tomographies have been verified using two very different samples, an iron fibula and a lapis lazuli. The results are a proof of concept of the validity and utility of the instrument for this application.

The work shown in this thesis demonstrates the applicability of the ANET CNC technology to a broader array of facilities, such as small and medium-sized reactors and accelerator-based facilities for a wide range of applications. It also demonstrates its potential to improve current facilities reliant on traditional collimating systems.

Appendix A

The Artificial Bee Colony

During this thesis an algorithm used recurrently and in different applications has been the Artificial Bee Colony, originally developed by Prof. Dervis Karaboga back in 2005 [66].
The algorithm is one of the most proficient metaheuristic[1] ones based on swarm intelligence to date when dealing with optimisation problems with many local inflexion points and complicated phase spaces. The design of the algorithm is based on the foraging behaviour of the honey bees, coordinating a number of searching elements that communicate and reinforce themselves, while avoiding to be stuck at local minima or maxima by expiring the food sources and searching for new ones. This family of metaheuristic algorithms has been gaining popularity in recent years, as shown in figure A.1.

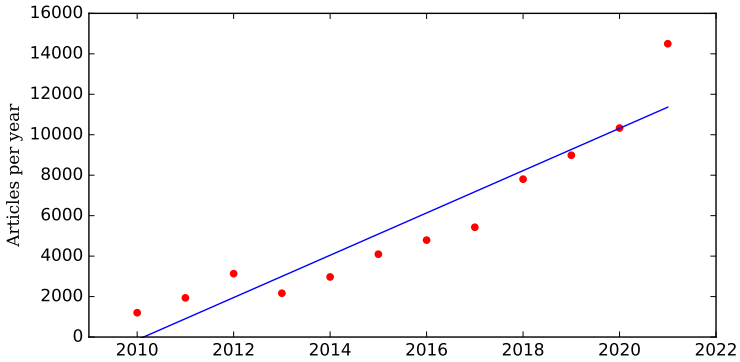

FIGURE A.1: Number of articles published related to the *Artificial Bee Colony* algorithm and *Swarm Intelligence* each year.

A.1 Origin

Swarm intelligence algorithms were first defined in 1993 by Gerardo Beni and Jing Wang, in a proceeding of the NATO Advanced Workshop on Robots and Biological Systems, held in Italy [68]. They published the concept of an algorithm which simulated the behaviour of a natural population, coherent with some certain rules and constraints, and the interaction of the individuals within those populations would lead to an "intelligent" global behaviour,

[1] In computer science and mathematical optimization, a metaheuristic is a higher-level procedure or heuristic designed to find, generate, or select a heuristic (partial search algorithm) that may provide a sufficiently good solution to an optimization problem, especially with incomplete or imperfect information or limited computation capacity [67].

unknown to the singular elements. Ants, birds, microbes, fish or bees are some of examples of natural behaviours that have been hypothesised since. With the essential concept of swarm intelligence in mind, the improvement brought by Prof. Karaboga was that of an algorithm capable of efficiently scout a massive phase space with a reduced number of iterations, that would not get stuck on local maxima or minima for long.

A.2 The original algorithm

The algorithm itself is based on the coordinated behaviour of a set of bees, which are represented by individual objects of 3 types: employees, onlookers and scouts. Each one has a defined role which is fulfilled within every iteration. First, the employed bees search for food around the food source they have in memory, while sharing the information regarding the food source (point in the phase space) to the colony. Within the colony then, the onlooker bees will lend a hand to the employees by helping their food source. Each onlooker will select an employed bee to help, and the decision of which will come based on the quality of the food source. The better the source, the more onlooker bees will come around to help, improving the computational search on the local area of the phase space, while lower quality areas will be less studied. After a certain number of iterations on a low quality food source, the employed bee will abandon it, becoming a scout, and will search for a new point of the phase space for a new food source. Typically, the number of onlooker bees is equal to that of the employed bees.n
Let $X_i = \{x_{i,1}, x_{i,2}, \ldots, x_{i,n}\}$ represent the i^{th} solution in the swarm, where n is the dimension size.
Each employed bee X_i generates a new candidate solution V_i in the neighbourhood of its present position as equation below:

$$v_{i,k} = x_{i,k} + \Phi_{i,k} \times (x_{i,k} - x_{j,k}) \tag{A.1}$$

where X_j is a randomly selected candidate solution (i), k is a random dimension index selected from the set $\{1, 2, \ldots, n\}$, and $\Phi_{i,k}$ is a random number within $[-1, 1]$. Once the new candidate solution V_i is generated, a greedy selection is used. If the fitness value of V_i is better than that of its parent X_i, then update X_i with V_i; otherwise keep X_i unchanged. After all employed bees complete the search process; they share the information of their food sources with the onlooker bees through waggle dances. An onlooker bee evaluates the nectar information taken from all employed bees and chooses a food source with a probability related to its nectar amount. This probabilistic selection is really a roulette wheel selection mechanism which is described as equation below:

$$P_i = \frac{\text{fit}_i}{\sum_j \text{fit}_j} \tag{A.2}$$

where fit_i is the fitness value of the i^{th} solution in the swarm. As seen, the better the solution i, the higher the probability of the i^{th} food source selected. If a position cannot be improved over a predefined limit number of cycles, then the food source is abandoned. Assume that the abandoned source is X_i,

and then the scout bee discovers a new food source to be replaced with i^{th} as equation below:

$$x_{i,k} = lb_k + \Phi_{i,k} \times (ub_k - lb_k) \tag{A.3}$$

where $\Phi_{i,k} = \text{rand}(0,1)$ is a random number within$[0,1]$ based on a normal distribution, and lb_k, ub_k are lower and upper boundaries of the k^{th} dimension, respectively.

A.3 State of the art improvements

Since the creation of the algorithm back in 2005, some great deal of variations have been presented that improve the searching capabilities of the individual bees, as well as constitute a major leap in the optimisation performance of the algorithm [69–72].
One of the most relevant improvements to date is merit of the work by Xiao et al. in 2019 [73]. Their proposal puts together some of the most successful ABC variations in the field: the Elite strategy and Dimension Learning.

1. *Elite Strategy*
   The Elite Strategy variation is an approach to improve the exploitation capabilities of the bees. Saving the N best solutions the employees have found and using them to improve the search of the onlookers increases the effectiveness of the search as well as save computational resources. It is an extension of the Global Best algorithm, in which at every step any bee takes it has to take into account the position of the best coordinates found.

2. *Dimension Learning*
   In the typical ABC, a random dimension j is selected to evaluate the solution search equation. In a single dimension, there's a high chance that the values are similar, and thus a small variation will occur. This limits the capability of the bee to jump position. For such, the Dimension Learning proposes the use of the difference between two different dimensions as step size, leading to a better probability of avoiding local points.

The two equations that compose the algorithm are the following:

$$v_{ij} = \frac{1}{2}(E_{lh} + Gbest_j) + \psi_{ij}(x_{ih} - E_{lj}) + \phi_{ij}(x_{ih} - Gbest_j) \tag{A.4}$$

$$v_{ij} = \frac{1}{2}(E_{mj} + Gbest_h) + \psi_{ij}(x_{ij} - E_{lh}) + \phi_{ij}(x_{ij} - Gbest_h) \tag{A.5}$$

Where v_{ij} is the step on iteration i, dimension j, E_{lh} is the dimension h of the l^{th} element of the Elite set, $Gbest_j$ is the j coordinate of the Global best solution, and ϕ and ψ are two random constants, ranging from -0.5 to 0.5 and 0 to 1 respectively which values change at every iteration and dimension. x_{ij} is the position of the bee at the i^{th} iteration on dimension j.
The first equation A.4 is the one used to compute the step of the employed bees, while equation A.5 is the one performed iterative by each onlooker σ

times per step, where σ is the number of elite solutions stored in memory.
The main algorithm remains practically the same, with the only inclusion of a 4th step, the updating of the global solution after the scout bee phase, and the update of the elite set after every employee or onlooker bee upgrades their best found solutions.

A.4 Benchmarking

To prove the effectiveness of the ABC-ESDL versus the original ABC some brief tests were performed, setting both algorithms to solve the same problem under the same computing conditions (equal number of bees and iterations).
The functions employed to compare the performance of both algorithms are the Rastrigin function (Eq. A.6) and the Eggholder function (Fig. A.3).
The Rastrigin function is usually used for optimisation problems and benchmarking as it is particulary difficult to solve. It is a non-convex function with a large number of local minima. First proposed by Leonard A. Rastrigin in 1974 [74], the funcion is shown in Figure A.2 and has the following equation:

$$f(X) = 10D + \sum_{i=1}^{D}[x_i^2 - 10cos(2\pi x_i)] \tag{A.6}$$

Where $X = (x_1, x_2, ...x_D)$, being D the number of dimensions. It has a global minimum at X = (0,0,...,0) with a value f(X) = 0. The search space comprised is -5.12 < x_i < 5.12.
In Figure A.2 it is displayed the representation of the Rastrigin function in 3D, as well as the performance of both the original and the modified ABC algorithms under the same initial configuration, 50 bees with a 100 iterations.

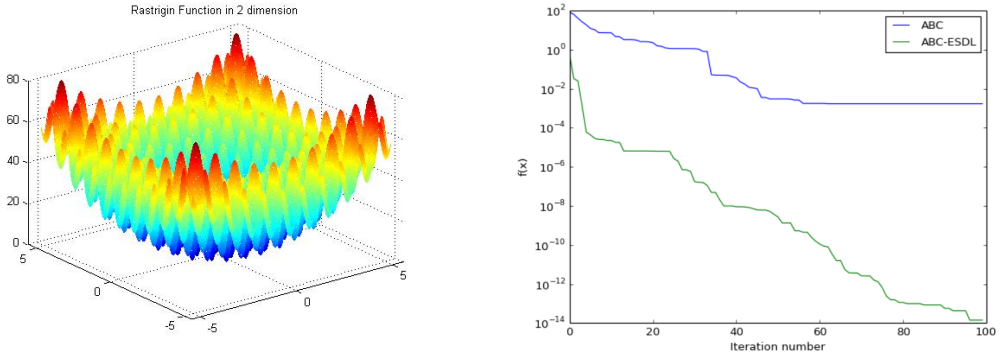

FIGURE A.2: Comparative plot of the performance between the classical ABC algorithm and the modified version, ABC-ESDL, applied to the Rastrigin function.

As seen on the graph on the right, the modified algorithm outperforms the original ABC by several orders of magnitude.
The second example used for benchmarking is the Eggholder function, with a

particularly complicated shape and a vast amount of local minima and maxima. The equation is the following:

$$f(x,y) = -(y+47)sin\sqrt{|\frac{x}{2}+(y+47)|} - xsin\sqrt{|x+(y+47)|} \tag{A.7}$$

Equation A.7 has a global minimum at $(x,y) = (512, 404.2319)$, with a value:

$$f(512, 404.2319) = -959.6407 \tag{A.8}$$

The searching range for the function is -512 < x,y < 512.

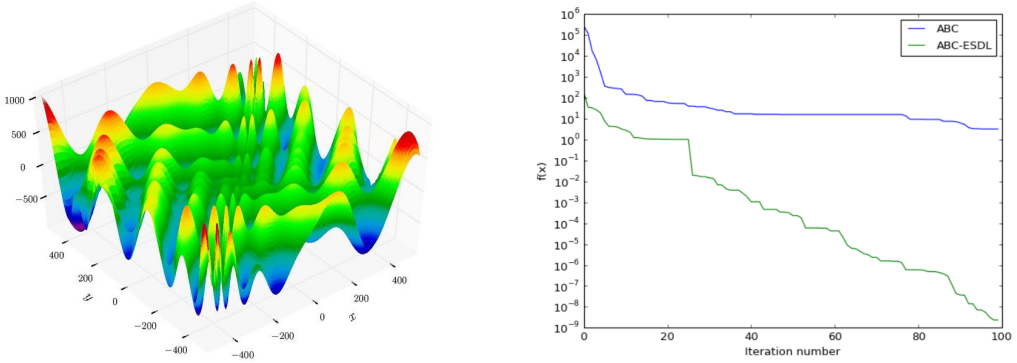

FIGURE A.3: Comparative plot of the performance between the classical ABC algorithm and the modified version, ABC-ESDL, applied to the Eggholder function.

After executing both algorithms under the same computational properties (50 bees, 100 iterations) the results are displayed in Figure A.3. As it happened with the Rastrigin function, the evolved ABC-ESDL outperformed the classical ABC by a wide margin.
Those results further justify the choice of the ABC-ESDL to solve the different problems where the phase space is massive and computationally demanding, forcing the use of more advanced methods in order to obtain reasonable results within discrete amounts of time.

Bibliography

[1] Burkhard Schillinger. "Why use neutrons?" In: *Restaurierung und Archäologie* 8 (2015), pp. 1–7.

[2] Oxford English Dictionary. "Oxford english dictionary". In: *Simpson, JA & Weiner, ESC* (1989).

[3] AP Kaestner et al. "Samples to determine the resolution of neutron radiography and tomography". In: *Physics Procedia* 88 (2017), pp. 258–265.

[4] Ronald N Bracewell. "Numerical transforms". In: *Science* 248.4956 (1990), pp. 697–704.

[5] Johann Radon. "On the determination of functions from their integral values along certain manifolds". In: *IEEE transactions on medical imaging* 5.4 (1986), pp. 170–176.

[6] Ali Mohamad-Djafari. *Inverse problems in vision and 3D tomography*. John Wiley & Sons, 2013.

[7] DJ Thomas and AV Alevra. "Bonner sphere spectrometers—a critical review". In: *Nuclear Instruments and Methods in Physics Research Section A: Accelerators, Spectrometers, Detectors and Associated Equipment* 476.1-2 (2002), pp. 12–20.

[8] Gabor T Herman. *Fundamentals of computerized tomography: image reconstruction from projections*. Springer Science & Business Media, 2009.

[9] M Van Heel et al. "The structure and function of invertebrate respiratory proteins". In: *EMBO workshop*. 1982, pp. 69–73.

[10] Marin Van Heel and Michael Schatz. "Fourier shell correlation threshold criteria". In: *Journal of structural biology* 151.3 (2005), pp. 250–262.

[11] Marin van Heel and Michael Schatz. "Reassessing the revolution's resolutions". In: *BioRxiv* (2017), p. 224402.

[12] Roland Beckmann et al. "Alignment of conduits for the nascent polypeptide chain in the ribosome-Sec61 complex". In: *Science* 278.5346 (1997), pp. 2123–2126.

[13] B Böttcher, SA Wynne, and RA Crowther. "Determination of the fold of the core protein of hepatitis B virus by electron cryomicroscopy". In: *Nature* 386.6620 (1997), pp. 88–91.

[14] PB Rosenthal, RA Crowther, and R Henderson. "An objective criterion for resolution assessment in single-particle electron microscopy (appendix)". In: *J Mol Biol* 333 (2003), pp. 743–745.

[15] WO Saxton and W_ Baumeister. "The correlation averaging of a regularly arranged bacterial cell envelope protein". In: *Journal of microscopy* 127.2 (1982), pp. 127–138.

[16] Elena V Orlova et al. "Structure of keyhole limpet hemocyanin type 1 (KLH1) at 15 Å resolution by electron cryomicroscopy and angular reconstitution". In: *Journal of molecular biology* 271.3 (1997), pp. 417–437.

[17] Claude Elwood Shannon. "A mathematical theory of communication". In: *The Bell system technical journal* 27.3 (1948), pp. 379–423.

[18] Alicia Fernandez-Oliveras, Antonio Manuel Pozo Molina, and Manuel Rubiño López. "Comparison of spectacle-lens optical quality by modulation transfer function measurements based on random-dot patterns". In: *Optical Engineering* 49.8 (2010), p. 083603.

[19] Saul N Friedman et al. "A simple approach to measure computed tomography (CT) modulation transfer function (MTF) and noise-power spectrum (NPS) using the American College of Radiology (ACR) accreditation phantom". In: *Medical physics* 40.5 (2013), p. 051907.

[20] Kenichiro Masaoka. "Practical edge-based modulation transfer function measurement". In: *Optics express* 27.2 (2019), pp. 1345–1352.

[21] Kristina T Wigati et al. "On the relevance of modulation transfer function measurements in digital mammography quality control". In: *Journal of Medical Imaging* 8.2 (2021), p. 023505.

[22] Françoise Viallefont-Robinet et al. "Comparison of MTF measurements using edge method: towards reference data set". In: *Optics express* 26.26 (2018), pp. 33625–33648.

[23] James Chadwick. "Possible existence of a neutron". In: *Nature* 129.3252 (1932), pp. 312–312.

[24] JR Dunning et al. "Interaction of neutrons with matter". In: *Physical Review* 48.3 (1935), p. 265.

[25] Luis W Alvarez. "The production of collimated beams of monochromatic neutrons in the temperature range 300-10 K". In: *Physical Review* 54.8 (1938), p. 609.

[26] George A Fink. "The production and absorption of thermal energy neutrons". In: *Physical Review* 50.8 (1936), p. 738.

[27] RL Maughan et al. "A simple multi-rod collimator for producing irregular fields". In: *International Journal of Radiation Oncology• Biology• Physics* 13 (1987), p. 120.

[28] Richard L Maughan et al. "A multirod collimator for neutron therapy". In: *International Journal of Radiation Oncology• Biology• Physics* 34.2 (1996), pp. 411–420.

[29] Kazuyuki Ogawa and Nebuyoshi Wakabayashi. "Thermal neutron radiography with a small reactor". In: *Applied Physics* 33.5 (1964), pp. 334–341.

[30] Anthony C Nunes and Giuseppe Zaccai. "Some focusing techniques and their application to low-angle neutron scattering." In: *Brookhaven symposia in biology*. 27. 1976, pp. VII49–VII56.

[31] Edward S Kenney and Alan M Jacobs. "Radiation Imaging—An Interesting Utilization of Nuclear Engineering Methodology". In: *Nuclear Technology* 27.1 (1975), pp. 67–77.

[32] V Orphan, D Kedem, and F Johansen. "Mobile neutron radiography system for aircraft inspection". In: *Neutron Radiography*. Springer, 1987, pp. 447–454.

[33] WE Dance et al. "DIANE: Advanced system for mobile neutron radiology". In: *Nuclear Instruments and Methods in Physics Research Section B: Beam Interactions with Materials and Atoms* 40 (1989), pp. 1316–1321.

[34] D Lundberg. *Neutron beam collimators*. US Patent 3,781,564. 1973.

[35] Masahito Matsubayashi et al. "Design and characteristics of the JRR-3M thermal neutron radiography facility and its imaging systems". In: *Nuclear technology* 132.2 (2000), pp. 309–324.

[36] F Mezei. "Novel polarized neutron devices: supermirror and spin component amplifier". In: *Communications on Physics (London)* 1.3 (1976), pp. 81–85.

[37] F. Mezei and P. A. Dagleish. *Corrigendum and first experimental evidence on neutron supermirrors*. 1977.

[38] C Schanzer, M Schneider, and P Böni. "Neutron optics: Towards applications for hot neutrons". In: *J. Phys: Conf. Ser.(submitted)*. 2016.

[39] C Petrillo et al. "A honeycomb collimator for the neutron Brillouin scattering spectrometer BRISP". In: *Nuclear Instruments and Methods in Physics Research Section A: Accelerators, Spectrometers, Detectors and Associated Equipment* 489.1-3 (2002), pp. 304–312.

[40] Matthew B Stone et al. "Characterization of plastic and boron carbide additive manufactured neutron collimators". In: *Review of Scientific Instruments* 88.12 (2017), p. 123102.

[41] Anton S Tremsin and W Bruce Feller. "The theory of compact and efficient circular-pore MCP neutron collimators". In: *Nuclear Instruments and Methods in Physics Research Section A: Accelerators, Spectrometers, Detectors and Associated Equipment* 556.2 (2006), pp. 556–564.

[42] AS Tremsin et al. "High resolution neutron radiography with very compact and efficient neutron collimators". In: *Journal of Instrumentation* 6.01 (2011), p. C01041.

[43] *Paul Scherrer Institut*. https://www.psi.ch/en. Accessed: 2021-07-29.

[44] *PCT Patent n. PCT/IB2021/053856 Collimator*.

[45] T Goorley et al. "Initial MCNP6 release overview". In: *Nuclear technology* 180.3 (2012), pp. 298–315.

[46] MB Chadwick et al. "ENDF/B-VII. 1 nuclear data for science and technology: cross sections, covariances, fission product yields and decay data". In: *Nuclear data sheets* 112.12 (2011), pp. 2887–2996.

[47] R. Bedogni et al. "Design of a compact neutron collimator". In: *Journal of Instrumentation* 16.08 (2021), P08055.

[48] Oriol Sans-Planell et al. "First results with the ANET Compact Thermal Neutron Collimator". In: *Journal of Instrumentation* 16.11 (2021), P11025.

[49] E Tejedor et al. "SWAN: a Service for Web-Based Data Analysis in the Cloud". In: *Proceedings of the 22nd International Conference on Computing in High Energy and Nuclear Physics (CHEP 2016)*. 2016.

[50] Massimo Lamanna. "The LHC computing grid project at CERN". In: *Nuclear Instruments and Methods in Physics Research Section A: Accelerators, Spectrometers, Detectors and Associated Equipment* 534.1-2 (2004), pp. 1–6.

[51] Kim Lefmann and Kristian Nielsen. "McStas, a general software package for neutron ray-tracing simulations". In: *Neutron news* 10.3 (1999), pp. 20–23.

[52] Peter Willendrup, Emmanuel Farhi, and Kim Lefmann. "McStas 1.7-a new version of the flexible Monte Carlo neutron scattering package". In: *Physica B: Condensed Matter* 350.1-3 (2004), E735–E737.

[53] P Willendrup et al. “McStas: Past, present and future”. In: *Journal of Neutron Research* 17.1 (2014), pp. 35–43.

[54] Peter Kjær Willendrup and Kim Lefmann. “McStas (i): Introduction, use, and basic principles for ray-tracing simulations”. In: *Journal of Neutron Research* 22.1 (2020), pp. 1–16.

[55] Peter Kjær Willendrup and Kim Lefmann. “McStas (ii): An overview of components, their use, and advice for user contributions”. In: *Journal of Neutron Research* Preprint (2020), pp. 1–21.

[56] E Lehmann et al. “Edge enhancement investigations by means of experiments and simulations”. In: *Physics Procedia* 88 (2017), pp. 282–289.

[57] M Morgano et al. “Neutron imaging options at the BOA beamline at Paul Scherrer Institut”. In: *Nuclear Instruments and Methods in Physics Research Section A: Accelerators, Spectrometers, Detectors and Associated Equipment* 754 (2014), pp. 46–56.

[58] Georg Brandl et al. “NICOS–The Instrument Control solution at the MLZ”. In: *10th International Workshop on Personal Computers and Particle Accelerator Controls*. IMPULSE-2014-00016. FZJ. 2014.

[59] David Brodrick et al. “EPICS Architecture for Neutron Instrument Control at the European Spallation Source”. In: *16th Int. Conf. on Accelerator and Large Experimental Control Systems (ICALEPCS'17), Barcelona, Spain, 8-13 October 2017*. JACOW, Geneva, Switzerland. 2018, pp. 1043–1047.

[60] Glenn D Boreman. *Modulation transfer function in optical and electro-optical systems*. Vol. 4. SPIE press Bellingham, WA, 2001.

[61] Michael D Abràmoff, Paulo J Magalhães, and Sunanda J Ram. “Image processing with ImageJ”. In: *Biophotonics international* 11.7 (2004), pp. 36–42.

[62] Manuel Dierick, Bert Masschaele, and Luc Van Hoorebeke. “Octopus, a fast and user-friendly tomographic reconstruction package developed in LabView®”. In: *Measurement Science and Technology* 15.7 (2004), p. 1366.

[63] Alessandro Lo Giudice et al. “Multitechnique characterization of lapis lazuli for provenance study”. In: *Analytical and bioanalytical chemistry* 395.7 (2009), pp. 2211–2217.

[64] Gloria Vaggelli et al. “Improvements to the analytical protocol of lapis lazuli provenance: First study on Myanmar rock samples”. In: *The European Physical Journal Plus* 134.3 (2019), p. 104.

[65] M Favaro et al. “Characterization of lapis lazuli and corresponding purified pigments for a provenance study of ultramarine pigments used in works of art”. In: *Analytical and bioanalytical chemistry* 402.6 (2012), pp. 2195–2208.

[66] Dervis Karaboga. *An idea based on honey bee swarm for numerical optimization*. Tech. rep. Technical report-tr06, Erciyes university, engineering faculty, computer . . ., 2005.

[67] R Balamurugan, AM Natarajan, and K Premalatha. “Stellar-mass black hole optimization for biclustering microarray gene expression data”. In: *Applied Artificial Intelligence* 29.4 (2015), pp. 353–381.

[68] Gerardo Beni and Jing Wang. “Swarm intelligence in cellular robotic systems”. In: *Robots and biological systems: towards a new bionics?* Springer, 1993, pp. 703–712.

[69] Dervis Karaboga and Bahriye Akay. "A comparative study of artificial bee colony algorithm". In: *Applied mathematics and computation* 214.1 (2009), pp. 108–132.

[70] Dervis Karaboga et al. "A comprehensive survey: artificial bee colony (ABC) algorithm and applications". In: *Artificial Intelligence Review* 42.1 (2014), pp. 21–57.

[71] Bahriye Akay and Dervis Karaboga. "A modified artificial bee colony algorithm for real-parameter optimization". In: *Information sciences* 192 (2012), pp. 120–142.

[72] Pei-Wei TSai et al. "Enhanced artificial bee colony optimization". In: *International Journal of Innovative Computing, Information and Control* 5.12 (2009), pp. 5081–5092.

[73] Songyi Xiao et al. "An Improved Artificial Bee Colony Algorithm Based on Elite Strategy and Dimension Learning". In: *Mathematics* 7.3 (2019), p. 289.

[74] Leonard Andreevič Rastrigin. "Systems of extremal control". In: *Nauka* (1974).